

Fast simulation of Volterra processes using random Fourier features with application to the log-stationary fractional Brownian motion

Othmane Zarhali¹ and Nicolas Langrené^{*2}

¹Ceremade, CNRS-UMR 7534, Université Paris-Dauphine PSL, Place du Maréchal de Lattre de Tassigny, 75016 Paris, France

²Guangdong Provincial/Zhuhai Key Laboratory of Interdisciplinary Research and Application for Data Science, Beijing Normal-Hong Kong Baptist University, Zhuhai, China

March 4, 2026

Abstract

A fast simulation framework for stochastic Volterra processes based on Random Fourier Features (RFF) approximation of the kernel is developed. After recalling the main properties of Volterra processes and reviewing existing numerical simulation methods, an accelerated scheme is introduced that relies on a spectral representation of the kernel. A particular attention is devoted to sampling from the kernel spectral density using Hamiltonian Monte Carlo, whose efficiency and stability bring more convenience than alternative sampling procedures. Quantitative guarantees for the proposed method are established, including moment estimates and strong error bounds. The approach is further compared with the kernel approximation by sum of exponentials (Random Laplace Features) commonly used in the literature, emphasizing the broader generality of the present framework. As a primary application, Volterra processes associated with the Stationary fractional Brownian Motion (S-fBM) kernel are investigated. A spectral density representation is derived in closed form using hypergeometric functions, a condition for positive definiteness is established, and explicit truncation as well as Monte Carlo error bounds are provided for the RFF approximation in this setting. Numerical experiments in dimensions one and two illustrate the accuracy of the kernel approximation, the reliable recovery of model parameters, and the competitiveness of the accelerated simulation scheme in terms of computational efficiency and both weak and strong error performance.

Keywords: Volterra processes, random Fourier features, Log S-fBM model, Fourier transform, hypergeometric functions, spectral density, spectral sampling.

1 Introduction

Stochastic Volterra equations (SVEs) have emerged as a central framework for modeling non-Markovian dynamics with memory effects. In contrast to classical Itô stochastic differential equations, the future evolution of an SVE depends on the entire past trajectory through a deterministic kernel, typically of convolution type. This non-local structure allows one to capture rough behavior, long-range dependence and hereditary phenomena arising in physics, biology and more recently in mathematical finance.

A general stochastic Volterra equation of convolution type can be written as

$$X_t = X_0 + \int_0^t K(t-s)b(X_s) ds + \int_0^t K(t-s)\sigma(X_s) dW_s, \quad (1)$$

*Corresponding author, nicolaslangrene@bnbu.edu.cn

where K is a deterministic kernel and W is a Brownian motion. When the kernel exhibits a fractional singularity of the form $K(t) = t^{H-\frac{1}{2}}$ with $H \in (0, 1)$, the solution typically fails to be a semimartingale for $H < \frac{1}{2}$, placing the model outside the scope of classical Itô calculus. A prominent example is the rough Heston model introduced in [El Euch and Rosenbaum \(2019\)](#), which combines a fractional Volterra-type variance process with affine transform techniques. The model preserves tractability through a fractional Riccati equation while reproducing key stylized facts of implied volatility surfaces, thus establishing a deep connection between stochastic Volterra equations and modern mathematical finance.

A systematic weak solution theory for stochastic Volterra equations of convolution type has been developed in [Abi Jaber et al. \(2021\)](#). Their work establishes general existence, stability and approximation results and provides a robust framework for analyzing non-Markovian dynamics under minimal structural assumptions on the kernel. In particular, they introduce techniques based on resolvent measures and affine transform methods that have become fundamental in the area.

A major breakthrough in connecting SVEs with tractable probabilistic structures was achieved in the theory of affine Volterra processes ([Abi Jaber et al., 2019](#)). This work extends the classical affine process framework to the Volterra setting, establishing exponential-affine transform formulas and Riccati-Volterra equations that characterize the Fourier-Laplace transform of the solution. These results provide the theoretical backbone for rough volatility models such as the rough Heston model.

From a numerical and approximation perspective, [Bayer and Breneis \(2023\)](#) proposed and analyzed multi-factor Markovian approximations of stochastic Volterra equations with fractional kernels. They prove strong convergence rates and show how singular Volterra dynamics can be approximated by finite-dimensional Markovian systems, thus bridging the gap between non-Markovian theory and computational practice. More recently, significant analytical progress has been made on pathwise uniqueness and strong solvability for singular kernels. [Prömel et al. \(2025\)](#) establish pathwise uniqueness for a broad class of singular stochastic Volterra equations, extending classical Yamada-Watanabe arguments to the non-Markovian setting. Their results clarify the interplay between kernel singularity and coefficient regularity in determining strong well-posedness.

Besides this singular power kernel, it can be of interest to study SVEs for other general classes of kernels. The focus of this paper is the class of *positive definite* kernels. By definition, a shift-invariant, isotropic kernel $K : [0, \infty[\rightarrow \mathbb{R}$ is said to be *positive definite* in \mathbb{R}^d if for any $N \geq 1$, $(\mathbf{x}_1, \dots, \mathbf{x}_N) \in \mathbb{R}^{d \times N}$ and $(z_1, \dots, z_N) \in \mathbb{R}^N$,

$$\sum_{i=1}^N \sum_{j=1}^N z_i z_j K(\|\mathbf{x}_i - \mathbf{x}_j\|) \geq 0. \quad (2)$$

Let Φ_d be the set of kernels that are positive definite in \mathbb{R}^d , and let Φ_∞ be the set of kernels that are in Φ_d for all $d \geq 1$. The construction and characterization of positive definite kernels have been extensively studied in the literature, since they coincide with covariance functions ([Yaglom, 1987a,b](#)). According to Bochner's theorem ([Sasvári, 2013](#), Theorem 1.7.3), $K \in \Phi_d$ if and only if it is the inverse Fourier transform of a finite nonnegative measure on $[0, \infty[$. In particular, $K \in \Phi_d$ admits the probabilistic representation

$$\forall \mathbf{u} \in \mathbb{R}^d, \quad K(\|\mathbf{u}\|) = K(0)\mathbb{E}[\cos(\boldsymbol{\eta} \cdot \mathbf{u})] \quad (3)$$

where the density of the random projection vector $\boldsymbol{\eta}$ is the inverse Fourier transform of $K(\|\cdot\|)/K(0)$. Such a kernel (3) can be well approximated by a sum of cosine terms; this is the *random Fourier features* methodology, ([Rahimi and Recht, 2007](#)) also known as *spectral sampling*. It provides the following explicit kernel approximation

$$K(\|\mathbf{x}_i - \mathbf{x}_j\|) \approx \varphi(\mathbf{x}_i)^\top \varphi(\mathbf{x}_j), \quad \text{where, for any } \mathbf{x} \in \mathbb{R}^d, \quad (4)$$

$$\varphi(\mathbf{x}) := \frac{\sqrt{K(0)}}{\sqrt{M}} \left[\cos(\boldsymbol{\eta}_1^\top \mathbf{x}) \quad \dots \quad \cos(\boldsymbol{\eta}_M^\top \mathbf{x}) \quad \sin(\boldsymbol{\eta}_1^\top \mathbf{x}) \quad \dots \quad \sin(\boldsymbol{\eta}_M^\top \mathbf{x}) \right]^\top \in \mathbb{R}^{2M} \quad (5)$$

The main objective of our paper is to leverage the kernel approximation (4) in the context of stochastic Volterra equations (1), in order to accelerate the numerical simulation of the solution of such SVEs.

This proposed methodology can be applied whenever the kernel function K is positive definite. A specific example of interest is the so-called stationary fractional Brownian motion (S-fBM) kernel, defined by

$$K(\tau) = \frac{\nu^2}{2} \left(1 - \left(\frac{|\tau|}{T} \right)^{2H} \right) \mathbb{1}_{\{|\tau| \leq T\}}, \quad \tau \in \mathbb{R} \quad (6)$$

The S-fBM covariance kernel appears in the context of the Log S-fBM model introduced in [Wu et al. \(2022\)](#) to bridge the rough volatility regime for non vanishing Hurst exponent H and the multifractal regime for vanishing Hurst exponent, characterized by the multifractal random walk model (see [Muzy and Bacry 2002](#); [Bacry and Muzy 2003](#); [Muzy et al. 2000](#)). The Log S-fBM model has been used as a building block for the Nested Stationary fractional factor model (NSfFM, [Zarhali et al. 2025](#)) which accounts for the empirical findings in [Wu et al. \(2022\)](#) that the Hurst exponent of single stocks are of order $H \simeq 0.01$ while the one of indices such as the S&P500 are of order $H \simeq 0.1$. A multivariate extension of Log S-fBM was developed recently in [Zarhali et al. \(2026\)](#) by considering a multidimensional analogue of the Hurst exponent (the co-Hurst matrix) and of the so-called intermittency parameter (the co-intermittency matrix) to define a multidimensional stationary fractional Brownian motion (mS-fBM). The model is able to interpolate between multidimensional rough volatility and multifractal regimes. As a further contribution to this literature, our paper is going to define, analyze and simulate numerically a Volterra process with S-fBM kernel (6).

Specifically, our paper makes the following contributions:

- We introduce a fast simulation scheme for Volterra processes based on random Fourier features. We propose to perform the spectral sampling using the Hamiltonian Monte Carlo method. Moment estimates and strong error bounds of the proposed numerical scheme are established.
- We compare our kernel decomposition by random Fourier features to the traditional multifactor approximation of Volterra kernels by a sum of exponential functions. In particular, we prove mathematically that our proposed decomposition can be successfully applied to a much larger class of kernel functions, including kernels with compact support such as the S-fBM kernel.
- We apply the proposed numerical scheme to Volterra processes defined by an S-fBM convolution kernel. In doing so, we establish a new formula for the spectral distribution of isotropic S-fBM kernels in terms of hypergeometric functions, along with an explicit condition to ensure its positive definiteness. Moreover, we establish an explicit error bound of the RFF simulation scheme tailored to the case of the S-fBM kernel.
- We illustrate numerically the competitiveness of fast Volterra simulation by RFF in terms of both computational runtime and error (weak and strong).

The paper is organized as follows. Section 2 recalls the main properties of Volterra processes and the existing methods to simulate them. Section 3 introduces the fast Volterra simulation scheme built upon the random Fourier features approximation of kernel functions, and Section 4 compares it to multifactor approximation of kernel functions by sums of exponentials. Section 5 defines the log-stationary fractional Brownian motion model, and Section 6 establishes spectral properties of the S-fBM kernel. Section 7 provides detailed numerical results about the RFF Volterra scheme. Finally, Section 8 concludes the paper.

2 Volterra processes

2.1 Overview

Let $(\Omega, \mathcal{F}, (\mathcal{F}_t)_{t \geq 0}, \mathbb{P})$ be a filtered probability space and $(W_t)_{t \geq 0}$ be a standard (\mathcal{F}_t) -Brownian motion. Stochastic Volterra processes form a broad class of non-Markovian models defined through integral representations of the form:

$$X_t = X_0 + \int_0^t K(t, s) \sigma(X_s) dW_s^1 \quad (7)$$

where $\sigma: \mathbb{R} \rightarrow \mathbb{R}$ is a globally Lipschitz continuous function and $K: \mathbb{R}_+^2 \rightarrow \mathbb{R}_+$ is a nonnegative, integrable kernel function. These processes naturally capture memory effects and long-range dependence and arise in turbulence, finance and statistical physics.

A prominent example is the fractional Brownian motion (fBM) with Hurst exponent $H \in (0, 1)$, which admits the following Volterra representation, also known as the Mandelbrot-Van-Ness representation:

$$B_t^H = \int_0^t K_H(t, s) dW_s, \quad (8)$$

where K_H is a singular kernel behaving like $(t-s)^{H-\frac{1}{2}}$, see [Mandelbrot and Van Ness \(1968\)](#); [Decreusefond and Üstünel \(1998\)](#). This representation has motivated the study of rough paths and stochastic calculus for Volterra-type processes ([Coutin and Qian, 2007](#)).

In mathematical finance, stochastic Volterra processes gained significant attention with the advent of rough volatility models, which generalize classical Markovian stochastic volatility models using Volterra-driven processes. For example, the rough Bergomi model ([Bayer et al., 2016](#)) defines the log-volatility process ξ as

$$\log(\xi_t) = \log(\xi_0) + \eta \int_0^t (t-s)^{H-\frac{1}{2}} dW_s, \quad (9)$$

with $H < \frac{1}{2}$, capturing the empirically observed roughness of volatility ([Bayer et al., 2016](#); [Gatheral et al., 2018](#)). More generally, affine and non-affine stochastic Volterra equations (SVEs) of the form

$$X_t = X_0 + \int_0^t K(t, s)b(X_s) ds + \int_0^t K(t, s)\sigma(X_s) dW_s \quad (10)$$

where $b: \mathbb{R} \rightarrow \mathbb{R}$ have been studied extensively. Existence, uniqueness and regularity results are provided in [Abi Jaber et al. \(2019\)](#), where applications to rough volatility and term-structure modeling are developed.

The motivation for studying stochastic Volterra processes arises from their ability to capture memory, roughness and long-range dependence (see [Mandelbrot and Van Ness 1968](#); [Coutin and Qian 2007](#)), which are ubiquitous features in natural and financial systems. Traditional Markovian stochastic models, such as the classical Black-Scholes or Heston models, fail to reproduce empirical stylized facts such as volatility clustering, roughness of realized volatility and persistence of correlations (see [Cont 2001](#); [Gatheral et al. 2018](#)). Stochastic Volterra processes, through their kernel-based integral representation, naturally incorporate these phenomena by allowing the current state to depend on the entire history of the driving noise ([Biagini et al., 2008](#); [Coutin and Qian, 2007](#)). In particular, the representation of fractional Brownian motion as a Volterra integral highlights how singular kernels can generate rough paths with Hurst exponent $H < 1/2$, providing a mathematically rigorous foundation for rough volatility models ([Mandelbrot and Van Ness, 1968](#); [Bayer et al., 2016](#)). Moreover, the flexibility of Volterra processes in multidimensional and non-linear settings enables modeling of cross-asset dependence, multifractality and other features observed in financial markets. This combination of theoretical richness and empirical relevance has driven extensive research into stochastic Volterra processes in recent years.

2.2 Simulation of Volterra processes: standard approaches

From a numerical perspective, Volterra kernels pose challenges for simulation. Classical schemes based on discretization incur high computational costs, motivating fast methods such as hybrid schemes ([Bennedsen et al., 2017](#)), Markovian approximations ([Abi Jaber and El Euch, 2019](#); [Zhu et al., 2021](#); [Bayer and Breneis, 2023](#)) and spectral or Fourier-based approaches ([Harms and Stefanovits, 2019](#)). These methods aim to preserve the covariance structure while achieving tractability.

2.2.1 The Gaussian Volterra case: Standard covariance matrix factorization

Consider first the simpler case of Gaussian Volterra processes (Mishura et al., 2020; Di Nunno et al., 2022), defined by:

$$X_t = X_0 + \int_0^t K(t, s)b(s) ds + \int_0^t K(t, s)\sigma(s) dW_s \quad (11)$$

where $\sigma: \mathbb{R}_+ \rightarrow \mathbb{R}$. We are interested in the case where $K: \mathcal{D} \rightarrow \mathbb{R}$ is a measurable kernel function and $\mathcal{D} \subset \mathbb{R}_+^2$ as for instance in Biagini et al. (2008). Since b and σ do not depend on X_s here, unlike the more general SVE (10), the resulting process X has a Gaussian distribution. Being Gaussian, X is fully characterized by its mean and covariance:

$$\begin{cases} \mathbb{E}[X_t] = \mathbb{E}[X_0] + \int_0^t K(t, u)b(u) du \\ \mathbb{Cov}(X_t, X_s) = \int_0^{t \wedge s} K(t, u)K(s, u)\sigma(u)^2 du. \end{cases} \quad (12)$$

Gaussian Volterra processes have become central in quantitative finance, particularly in rough volatility modeling because they lead to tractable analytical computations of covariance and correlation structures as exploited in Bayer et al. (2016); Gatheral et al. (2018). Their Gaussianity ensures that linear functionals, such as option pricing kernels, remain analytically or numerically manageable, while the kernel choice provides flexibility to calibrate to market data or introduce desired memory properties.

Many methodologies exist to simulate Gaussian processes (Liu et al., 2019), provided the mean and covariance (12) can be computed analytically. The most standard simulation approach relies on discretizing the time interval, constructing the associated covariance matrix, factorizing it using the Cholesky decomposition, and multiplying it by a vector of i.i.d. Gaussian simulations. This method is both straightforward and exact, making it attractive for small to moderate grid sizes and for benchmarking purposes. However, the Cholesky-based simulation suffers from significant computational and practical disadvantages. First, its computational complexity scales cubically in the number of time steps, $\mathcal{O}(N^3)$, while memory requirements scale as $\mathcal{O}(N^2)$, rendering it infeasible for fine discretizations or long time horizons commonly required in applications such as Monte Carlo pricing or calibration. Second, the method lacks flexibility in adaptive or non-uniform grids, since any change in the time discretization requires recomputation of the full covariance matrix and its factorization. Third, numerical stability issues may arise when the covariance matrix becomes ill-conditioned, as is often the case for kernels with strong singularities near the diagonal, such as those appearing in fractional or rough Volterra models. These limitations have motivated the development of alternative simulation techniques, including hybrid schemes, convolution-based methods and Markovian approximations, which trade exactness for substantial gains in efficiency while maintaining controlled accuracy.

2.2.2 Euler discretization scheme

Another common numerical approach for simulating stochastic Volterra differential equations of the form of Eq. (7) is based on an Euler-type discretization of the stochastic integral, where the process is evaluated on a time grid and the integral is approximated by a weighted sum of Brownian increments. In this scheme, the kernel $K(t, s)$ is discretized explicitly and the diffusion coefficient $\sigma(X_s)$ is frozen at previous grid points, leading to a natural extension of the Euler–Maruyama method to non-Markovian settings. This can be formulated as follows:

The main advantage of this approach lies in its simplicity and broad applicability, as it accommodates general kernels and nonlinear diffusion coefficients without requiring Gaussianity or explicit covariance structures. Nevertheless, the Euler scheme for Volterra equations exhibits several important disadvantages. First, the method typically suffers from low strong convergence rates, which are further deteriorated by the presence of kernel singularities near the diagonal, as encountered in fractional or rough volatility models. In such cases, convergence rates may be significantly slower than the classical 1/2 rate of standard SDEs. Second, the scheme is computationally expensive, as each time step requires summation over all past increments, leading to $\mathcal{O}(N^2)$ complexity for a single path simulation, which becomes prohibitive for large-scale Monte Carlo

Algorithm 1 Euler scheme of Volterra process of Eq. (7)

Input: Time grid $t_0 = 0 < t_1 < t_2 < \dots < t_N = T$;

Input: N i.i.d. standard Gaussian random variables G_1, G_2, \dots, G_N

Output: One simulated path $(\tilde{X}_{t_n})_{n=0}^N$

$\tilde{X}_{t_0} \leftarrow x_0$

for $t_n = t_0, t_1, \dots, t_{N-1}$ **do**

$\tilde{X}_{t_0, t_n} \leftarrow x_0$

for $t_i = t_0, t_1, \dots, t_{n-1}$ **do**

$\tilde{X}_{t_{i+1}, t_n} \leftarrow \tilde{X}_{t_i, t_n} + K(t_n - t_i) \sigma(t_i, \tilde{X}_{t_i}) \sqrt{t_{i+1} - t_i} G_{i+1}$

$\tilde{X}_{t_n} \leftarrow \tilde{X}_{t_n, t_n}$

applications. Third, error propagation is more severe than in Markovian systems, since inaccuracies introduced at early time steps persist and influence the entire future trajectory through the memory structure of the Volterra kernel. Moreover, stability issues may arise when σ is highly nonlinear or only locally Lipschitz, potentially leading to bias or divergence unless very fine time discretizations are employed. These limitations have spurred the development of improved schemes, such as higher-order discretizations, truncated memory methods and hybrid or multilevel approaches, which aim to balance computational efficiency with accuracy while preserving the essential non-Markovian features of the Volterra dynamics.

3 Fast simulation of Volterra processes using Random Fourier Features

In the context of SVEs, RFFs allow the kernel-driven memory term to be expressed as a finite sum of stochastic integrals with random weights, providing a tractable and accurate Monte Carlo approximation. Here, we incorporate the RFF in the discretization scheme of stochastic Volterra equations. After exposing the classical Euler scheme in Section 2.2.2 and evoking its limitation particularly when it comes to generate long sample paths, the focus is made in the acceleration scheme with RFF as well as the associated estimates. For that sake, we start by presenting the Random Fourier Features representation of the kernel formulated as a proper Monte Carlo estimate sampled from the associated spectral density then we present the sampling procedure used in the upcoming theoretical error bounds for an arbitrary kernel as well as numerical experiments.

3.1 Random Fourier Features representation

Random Fourier features (RFF), introduced in [Rahimi and Recht \(2007\)](#), provide a scalable approach to approximate shift-invariant kernels by representing them as expectations over randomized feature maps. By sampling a finite number of random frequencies, the kernel can be approximated efficiently, reducing the computational complexity of kernel methods from quadratic to linear in the number of data points. Subsequent works have extended this idea, including the Fastfood algorithm for faster computation ([Le et al., 2013](#)) and rigorous error bounds for Monte Carlo approximations ([Sutherland and Schneider, 2015](#)). RFF have been applied for Gaussian processes ([Lázaro-Gredilla et al., 2010](#)) and signal processing ([Vedaldi and Zisserman, 2012](#)), enabling low-rank approximations and efficient simulation of high-dimensional stochastic systems.

In RFF simulations, the spectral density (for which we have derived the main properties in Section 6.1 for the S-fBM kernel) plays a central role by determining how the random frequencies used to approximate a shift-invariant kernel are sampled. By Bochner’s theorem, any continuous, positive-definite, shift-invariant kernel can be expressed as the Fourier transform of a nonnegative measure, whose density is the kernel’s spectral density. Sampling frequencies from this spectral density ensures that the expected inner product of the resulting random features matches the target kernel function. Consequently, the shape of the spectral density directly controls which frequency components are emphasized in the approximation, influencing smoothness, length-scale behavior and approximation accuracy of the simulated kernel. A correct choice and

sampling of the spectral density are therefore essential for the Random Fourier Features map to provide an unbiased and consistent kernel approximation.

Quantitatively speaking, consider any positive definite kernel K extended to the entire real line symmetrically: for all $u \geq 0$, we set $K(-u) = K(u)$. This ensures that K remains well-defined and symmetric. Under these assumptions, it is known that the kernel admits the following RFF representation (see [Rahimi and Recht 2007](#)):

$$K(u) = K(0) \mathbb{E}[\cos(\eta u)], \quad (13)$$

where the density of the random variable η is the spectral density of K . The expectation \mathbb{E} in this equation can be approximated by Monte Carlo simulations. Let $\eta_1, \eta_2, \dots, \eta_M$ be M independent and identically distributed simulations of η , independent of W . From equation (13), a Monte Carlo approximation of the kernel K is given by:

$$\hat{K}_M(u) = \frac{K(0)}{M} \sum_{m=1}^M \cos(\eta_m u) \quad (14)$$

The aim of the upcoming section is to detail the sampling algorithm from the spectral density, exposing theoretical sampling guarantees of the quantity of Eq. (14).

3.2 Sampling from the spectral density

As long as the spectral density of the underlying kernel is available in closed form up to an unknown multiplicative constant, sampling can be performed using either acceptance–rejection (AR) methods or Markov chain Monte Carlo (MCMC) techniques. Although AR sampling is exact and non-iterative, its efficiency relies critically on the construction of a proposal density that uniformly dominates the target density and on the choice of a tight upper-bounding constant. In moderate to high dimensions, these requirements can result in vanishing acceptance probabilities, making the AR approach impractical. MCMC methods, by contrast, are explicitly designed to operate with unnormalized target densities. Within this class, Hamiltonian Monte Carlo (HMC) offers significant advantages over random-walk Metropolis–Hastings (MH). While MH proposals are typically local and suffer from diffusive random-walk behavior—resulting in slow mixing and high autocorrelation particularly in high dimension, HMC exploits gradient information of the log-target density to construct coherent, long-range proposals via approximate Hamiltonian dynamics. This mechanism preserves high acceptance rates while enabling efficient exploration along level sets of the target distribution. As a result, HMC achieves substantially higher effective sample sizes per unit computational cost than both AR and standard MH methods, making it particularly well suited for scalable Monte Carlo when only the unnormalized target density is available.

3.2.1 Hamiltonian Monte Carlo

The HMC was originally introduced in [Duane et al. \(1987\)](#) as a sampling method inspired by Hamiltonian dynamics for lattice field theory. The key idea is to augment the target distribution with auxiliary momentum variables and to simulate a deterministic Hamiltonian flow that preserves the invariant measure, thereby producing distant proposals with high acceptance probability. The practical implementation relies on a numerical integrator, typically the leapfrog scheme, which ensures approximate energy conservation and detailed balance. This foundational work laid the theoretical and algorithmic basis for modern variants of HMC widely used in Bayesian inference.

We start by recalling the HMC algorithm. First, we fix some notations. Let $\pi(x)$ be the target spectral probability density supported in \mathbb{R}^d . We define the potential energy as:

$$U(x) = -\log \pi(x) \quad (15)$$

and introduce auxiliary momentum $p \in \mathbb{R}^d$ with kinetic energy

$$K(p) = \frac{1}{2} p^\top M^{-1} p \quad (16)$$

where M is a symmetric positive-definite mass matrix (often $M = I$). The Hamiltonian is

$$H(x, p) = U(x) + K(p) \quad (17)$$

Its dynamics follow Hamilton's equations

$$\begin{cases} \frac{dx}{dt} = \nabla_p H(x, p) \\ \frac{dp}{dt} = -\nabla_x H(x, p) \end{cases} \quad (18)$$

By definition, one has that:

$$\begin{cases} \nabla_p H(x, p) = M^{-1} p \\ \nabla_x H(x, p) = \nabla U(x) \end{cases},$$

which means that the Hamiltonian dynamics can be reformulated as:

$$\begin{cases} \frac{dx}{dt} = M^{-1} p \\ \frac{dp}{dt} = -\nabla U(x) \end{cases} \quad (19)$$

In practice, the Hamiltonian dynamics is discretized using the leapfrog integrator with step size $\varepsilon > 0$ and L steps formulated as:

$$\begin{cases} p(t + \frac{\varepsilon}{2}) = p(t) - \frac{\varepsilon}{2} \nabla U(x(t)), \\ x(t + \varepsilon) = x(t) + \varepsilon M^{-1} p(t + \frac{\varepsilon}{2}) \\ p(t + \varepsilon) = p(t + \frac{\varepsilon}{2}) - \frac{\varepsilon}{2} \nabla U(x(t + \varepsilon)) \end{cases} \quad (20)$$

This is framed in Algorithm 2.

Algorithm 2 Hamiltonian Monte Carlo (HMC)

Input: Initial position $x^{(0)}$;

Input: Step size ε , number of leapfrog steps L ;

Input: Mass matrix M , number of iterations N

Output: Samples $\{x^{(n)}\}_{n=1}^N$

for $n = 0, 1, \dots, N - 1$ **do**

Sample momentum $p^* \sim \mathcal{N}(0, M)$

$x \leftarrow x^{(n)}$ $p \leftarrow p^*$

/* Leapfrog integration of Hamiltonian dynamics */

$p \leftarrow p - \frac{\varepsilon}{2} \nabla U(x)$

for $\ell = 1, 2, \dots, L$ **do**

| $x \leftarrow x + \varepsilon M^{-1} p$ **if** $\ell < L$ **then**

| | $p \leftarrow p - \varepsilon \nabla U(x)$

$p \leftarrow p - \frac{\varepsilon}{2} \nabla U(x)$ $p \leftarrow -p$ /* Momentum flip for reversibility */

$\alpha \leftarrow \min(1, \exp(-H(x, p) + H(x^{(n)}, p^*)))$

With probability α , set $x^{(n+1)} \leftarrow x$;

otherwise set $x^{(n+1)} \leftarrow x^{(n)}$

Appendix B analyzes the HMC dynamics by viewing it as a continuous-time Markov process and studying its long-term behavior. First, it derives the infinitesimal generator of the process. The generator naturally

splits into two components: a deterministic part corresponding to the Hamiltonian flow, which moves the state smoothly along trajectories that conserve energy and a stochastic jump part corresponding to momentum updates governed by an acceptance rule. Next, the appendix shows that the Hamiltonian itself can be used to construct a Lyapunov function, meaning that the process has a natural tendency to return toward regions of moderate energy. This establishes a drift condition for the generator, which implies stability of the dynamics. Finally, these stability properties are used to prove geometric ergodicity of the Markov process, leading to exponential decay of correlations between samples.

3.2.2 Discretization scheme with RFF approximation

Herein, we are interested in the discretization scheme of Eq. (7) using Random Fourier Features. For any positive definite, symmetric kernel, Eq. (13) holds. For many kernels of practical interest, the distribution of the random projection η can be computed explicitly, allowing for straightforward simulation, which is the case of the S-FBM kernel as developed in Section 3.1.

Substituting (13) into (7), we can express X as

$$X_t = X_0 + K(0) \int_0^t \mathbb{E}_\eta[\cos(\eta(t-s))] \sigma(s, X_s) dW_s, \quad (21)$$

where $\mathbb{E}_\eta[\cdot] = \mathbb{E}[\cdot | W]$ denotes the expectation with respect to the distribution of η , conditionally on the Brownian motion W . Applying the standard cosine decomposition formula $\cos(a-b) = \cos(a)\cos(b) + \sin(a)\sin(b)$ allows the integrand to be separated as

$$X_t = X_0 + \mathbb{E}_\eta \left[K(0) \cos(\eta t) \int_0^t \cos(\eta s) \sigma(s, X_s) dW_s + K(0) \sin(\eta t) \int_0^t \sin(\eta s) \sigma(s, X_s) dW_s \right]. \quad (22)$$

Using Eq. (14), the SVE (7) can be approximated by the process X^M with the following dynamic:

$$X_t^M = X_0 + \int_0^t \frac{K(0)}{M} \sum_{m=1}^M \cos(\eta_m(t-s)) \sigma(s, X_s^M) dW_s, \quad t \geq 0. \quad (23)$$

Applying the cosine decomposition formula again, this representation can be rewritten in a more computationally convenient form:

$$\begin{aligned} X_t^M &= X_0 + \int_0^t \frac{K(0)}{M} \sum_{m=1}^M (\cos(\eta_m t) \cos(\eta_m s) + \sin(\eta_m t) \sin(\eta_m s)) \sigma(s, X_s^M) dW_s \\ &= X_0 + \frac{K(0)}{M} \sum_{m=1}^M \left[\cos(\eta_m t) \int_0^t \cos(\eta_m s) \sigma(s, X_s^M) dW_s + \sin(\eta_m t) \int_0^t \sin(\eta_m s) \sigma(s, X_s^M) dW_s \right]. \end{aligned} \quad (24)$$

The process X^M can be simulated efficiently, as described in Algorithm 3.

The formulation (24) allows for a tractable and efficient Monte Carlo approximation of the SVE, where the high-dimensional memory effect induced by K is captured via a finite sum of random Fourier features. Furthermore, it is competitive against the two previous methods (covariance factorization and Euler scheme) with a computational complexity of $\mathcal{O}(N \times M)$, where M is the number of spectral points, typically set to a few dozen points in practice (Lázaro-Gredilla et al., 2010; Rudi and Rosasco, 2017; Delbridge et al., 2020). In the next sections, we investigate the theoretical guarantees and error bounds of the RFF-based numerical scheme.

3.2.3 Quantitative estimates

This part is devoted to quantitative estimates for the time-discretized Volterra scheme with its RFF approximation for an arbitrary kernel. We first introduce an Euler-type discretization associated with a generic

Algorithm 3 RFF scheme for the SVE of (24)

Input: Time grid $t_0 = 0 < t_1 < \dots < t_N = T$

Input: N i.i.d. standard Gaussian random variables G_1, \dots, G_N

Input: M i.i.d. random variables η_1, \dots, η_M

Output: One simulated path $(\tilde{X}_{t_n}^M)_{n=0}^N$

Initialize $\tilde{X}_{t_0}^M \leftarrow 0$, $\tilde{C}_{t_0}^m \leftarrow 0$ and $\tilde{S}_{t_0}^m \leftarrow 0$ for $m = 1, \dots, M$

for $n = 0, 1, \dots, N-1$ **do**

for $m = 1, 2, \dots, M$ **do**

$$\tilde{C}_{t_{n+1}}^m \leftarrow \tilde{C}_{t_n}^m + \cos(\eta_m t_n) \sigma(t_n, \tilde{X}_{t_n}^M) \sqrt{t_{n+1} - t_n} G_{n+1}$$

$$\tilde{S}_{t_{n+1}}^m \leftarrow \tilde{S}_{t_n}^m + \sin(\eta_m t_n) \sigma(t_n, \tilde{X}_{t_n}^M) \sqrt{t_{n+1} - t_n} G_{n+1}$$

$$\tilde{X}_{t_{n+1}}^M \leftarrow X_0 + \frac{K(0)}{M} \sum_{m=1}^M \left(\cos(\eta_m t_{n+1}) \tilde{C}_{t_{n+1}}^m + \sin(\eta_m t_{n+1}) \tilde{S}_{t_{n+1}}^m \right)$$

kernel K on an arbitrary time grid and then define its random-features counterpart obtained by replacing the kernel with a finite-dimensional spectral approximation. Under standard growth, Lipschitz continuity and temporal regularity assumptions on the volatility coefficient, we derive moment bounds, Hölder-type regularity estimates and sharp \mathcal{L}^p error bounds that quantify both the time-discretization error and the additional approximation error induced by the random features expansion. For that sake, let us consider for each $N \geq 1$ a discrete grid

$$\pi_N = \{0 = t_0^N < t_1^N < \dots < t_N^N = T_f\}$$

and denote

$$\delta_N := \max_{0 \leq k \leq N-1} (t_{k+1}^N - t_k^N), \quad \zeta_N(s) := t_k^N, \quad \text{for } s \in [t_k^N, t_{k+1}^N[, \quad k \geq 0.$$

We consider the underlying scheme process X_N defined as:

$$X_N(t) = X_0 + \int_0^t K(t - \zeta_N(s)) \sigma(\zeta_N(s), X_N(\zeta_N(s))) dW_s. \quad (25)$$

In practice, we only simulate the values of X_N pointwisely on the discrete-time grid

$$\pi_N = \{t_k, \quad k = 0, 1, \dots, N\}.$$

This can be achieved by generating the Brownian motion increments

$$\Delta W_{k+1} := W_{t_{k+1}} - W_{t_k}, \quad k = 0, \dots, N-1.$$

Let $\Delta t_{k+1} := t_{k+1} - t_k$ and initialize $X_N(t_0) := X_0$. Then, the recursive scheme is given by

$$X_N(t_{k+1}) = X_0 + \sum_{i=0}^k K(t_{k+1} - t_i) \sigma(t_i, X_N(t_i)) \Delta W_{i+1}.$$

We introduce the scheme with random Fourier features scheme denoted X_N^M and defined as:

$$X_N^M(t) = X_0^M + \int_0^t \hat{K}_M(t - \zeta_N(s)) \sigma(\zeta_N(s), X_N^M(\zeta_N(s))) dW_s. \quad (26)$$

In the sequel, we consider the following assumptions on σ :

$$\mathcal{H}_1 : \quad \forall (s, x) \in \mathbb{R}_+^2, \quad |\sigma(s, x)| \leq C_1(1 + |x|) \quad (27)$$

$$\mathcal{H}_2 : \quad \forall (t, s) \in \mathbb{R}_+^2, \quad |\sigma(t, x) - \sigma(s, x)| \leq C_2 |x - y|, \quad (28)$$

$$\mathcal{H}_3 : \quad \forall (t, s) \in \mathbb{R}_+^2, \quad |\sigma(t, x) - \sigma(s, x)| \leq C_3 |t - s|^{\alpha \wedge 1} (1 + |x|), \quad \alpha > 0 \quad (29)$$

which correspond respectively to the linear growth and the linear growth in space and Hölder in time conditions.

We establish moment estimates as well as the Hölder regularity of the schemes (25) and (26) in the following theorem, proved in Appendix C.2.

Theorem 1. *If σ satisfies Assumption \mathcal{H}_1 and K satisfies the integrability conditions of Assumptions I and II in [Decreusefond \(2002\)](#), the following claims hold:*

1. *For any compact $\mathcal{K} \subset \mathbb{R}_+$, there exist positive constants $C_1(\mathcal{K})$ and $C_2(\mathcal{K})$ such that:*

$$\forall p > 0, \forall M \in \mathbb{N}, \quad \begin{cases} \sup_{t \in \mathcal{K}} \mathbb{E}[|X_N(t)|^p] \leq C_1(\mathcal{K}) \left(\mathbb{E}[|X_0|^p] + |K(0)|^p \right), \\ \sup_{t \in \mathcal{K}} \mathbb{E}[|X_N^M(t)|^p] \leq C_2(\mathcal{K}) \left(\mathbb{E}[|X_0^M|^p] + |K(0)|^p \right). \end{cases} \quad (30)$$

2. *There exist positive constants C_p such that:*

$$\forall (t, s) \in \mathcal{K}^2, \quad \forall p > 0, \forall M \in \mathbb{N}, \quad \mathbb{E}[|X_N^M(t) - X_N^M(s)|^p] \leq C_p \left(|t - s|^{p/2} + 1 \right) \quad (31)$$

The following results quantify, for an arbitrary kernel of the form of Section 3.1, the propagation of errors using the scheme of Eq. (26). Theorem 2, proved in Appendix C.3, provides a \mathcal{L}^p bound on the discrepancy between the Euler scheme X_N and its random feature approximation X_N^M .

Theorem 2. *If σ satisfies \mathcal{H}_1 and \mathcal{H}_2 and K the integrability conditions of Assumptions I and II in [Decreusefond \(2002\)](#), then for any arbitrary compact $\mathcal{K} \subset \mathbb{R}_+$, there exists a positive constant $C_{\mathcal{K}}^p > 0$ such that:*

$$\forall M \in \mathbb{N}, \forall t \in \mathcal{K}, \quad \sup_{s \in [0, t]} \mathbb{E}[|X_N(s) - X_N^M(s)|^p] \leq \begin{cases} \frac{C_{\mathcal{K}}^p}{M^{p-1}} e^{C_{\mathcal{K}}^p t}, & \text{if } 1 \leq p < 2 \\ C_{\mathcal{K}}^p \left(\frac{2}{M^{p-1}} + \left(\frac{4^p}{M} \right)^{\frac{1}{2}} \right) e^{C_{\mathcal{K}}^p t}, & \text{if } p \geq 2 \end{cases} \quad (32)$$

The above strong error bound guarantees uniform-in-time control (on compact subsets of \mathbb{R}_+) of the RFF scheme with respect to its Euler counterpart. The bound is explicit in the discretization parameter M and highlights two different convergence regimes depending on whether $p < 2$ or $p \geq 2$. In particular, for $1 \leq p < 2$, the error behaves essentially like $M^{-(p-1)}$, while for $p \geq 2$ an additional term of order $M^{-1/2}$ appears. The exponential factor $e^{C_{\mathcal{K}}^p t}$ arises from a Grönwall-type argument and captures the accumulation of local discretization errors over time.

One can propagate one step further to explicit the error bound between the true SVE solution and the RFF scheme.

Proposition 1. *If σ satisfies \mathcal{H}_1 , \mathcal{H}_2 and \mathcal{H}_3 and K the integrability conditions of Assumptions I and II in [Decreusefond \(2002\)](#), then for any $p > 0$ and $\varepsilon \in \left] \frac{1}{p}, \alpha \wedge 1 \right[$ there exist positive constants K_p^1 and K_p^2 such that:*

$$\sup_{s \in [0, t]} \mathbb{E}[|X_s - X_N^M(s)|^p] \leq \begin{cases} K_p^1 \left(\left(1 + \mathbb{E}[|X_0|^p] \right) \delta_N^{p(\alpha \wedge 1) - \varepsilon} + \frac{e^{C_{\mathcal{K}}^p t}}{M^{p-1}} \right), & \text{if } 1 \leq p < 2 \\ K_p^2 \left(\left(1 + \mathbb{E}[|X_0|^p] \right) \delta_N^{p(\alpha \wedge 1) - \varepsilon} + \left(\frac{2}{M^{p-1}} + \left(\frac{4^p}{M} \right)^{\frac{1}{2}} \right) e^{C_{\mathcal{K}}^p t} \right), & \text{if } p \geq 2 \end{cases}$$

Indeed, the bound decomposes naturally into two contributions: the first term, of order $\delta_N^{p(\alpha \wedge 1) - \varepsilon}$, corresponds to the approximation error induced by the time discretization, while the second term reflects the time-discretization error associated with M , as already identified in Theorem 2. The estimate holds uniformly in time as in the previous result and two regimes appear depending on whether $1 \leq p < 2$ or $p \geq 2$, with

an additional $M^{-1/2}$ contribution for higher moments. This proposition therefore quantifies the combined impact of the RFF sampling and the Euler time discretization, yielding explicit convergence rates for both procedures.

In Section 6.3, we will leverage the Markovian structure of the HMC sampling to derive explicit Monte Carlo bounds of the RFF kernel approximation and incorporate it in the strong error bounds of Theorem 2 and Proposition 1 in the case of the S-fBM kernel to derive sharper and explicit bounds.

4 Benchmarking with the multifactor approximation

4.1 Completely monotonic kernels

Definition 1. Let $K : [0, +\infty[\rightarrow \mathbb{R}$ be a continuous, bounded, shift-invariant, infinitely differentiable kernel function. It is said to be *completely monotonic* if

$$(-1)^n K^{(n)}(x) \geq 0 \quad (33)$$

for all $n \in \mathbb{N}$ and $x > 0$.

According to the Hausdorff-Bernstein-Widder theorem (Sasvári, 2013, Theorem 3.9.6), K is completely monotonic if and only if it is the inverse Laplace transform of a finite nonnegative measure on $[0, \infty)$. In particular, a completely monotonic K admits the probabilistic representation

$$K(u) = K(0) \mathbb{E} [e^{-\eta u}] , \quad \forall u \geq 0 \quad (34)$$

where the density of the random variable η is the inverse Laplace transform of $K(\cdot)/K(0)$. Such a kernel (34) can be well approximated by a sum of exponential terms; this is the *random Laplace features* methodology.

4.2 The multifactor method

The multifactor method for simulating stochastic Volterra processes in the sense of [Abi Jaber and El Euch \(2019\)](#) is based on approximating a non-Markovian Volterra dynamics by an explicit finite-dimensional Markovian system that is numerically tractable and converges to the original process as the number of factors increases. A stochastic Volterra equation with kernel K on a filtered probability space $(\Omega, \mathcal{F}, \mathbb{F}, \mathbb{P})$ is typically written as

$$X_t = u_0(t) + \int_0^t K(t-s) b(X_s) ds + \int_0^t K(t-s) \sigma(X_s) dW_s,$$

where b and σ are drift and diffusion coefficients and W is an \mathbb{F} -Brownian motion. For rough volatility models (e.g. rough Heston), one considers a singular one dimensional kernel also known as power law kernels of the form:

$$K(t) = \frac{t^{\alpha-1}}{\Gamma(\alpha)}, \quad \alpha \in \left] 0, \frac{1}{2} \right[,$$

which induce non-Markovian and non-semimartingale behavior that is difficult to simulate directly. The multifactor method approximates the kernel K by a finite sum of exponentials seen as a completely monotone approximation justified by Hausdorff-Bernstein-Widder theorem (Sasvári, 2013, Theorem 3.9.6) which is nothing else but the empirical counterpart of Eq. (34). The approximation takes the form:

$$K_n(t) = \sum_{i=1}^n c_i e^{-x_i t}, \quad \text{with weights } c_i > 0 \text{ and rates } x_i > 0,$$

chosen so that $K_n \rightarrow K$ in L^2 . Under such an approximation, one defines factor processes $(Y_t^{n,i})_{i=1, \dots, n}$ satisfying

$$dY_t^{n,i} = -x_i Y_t^{n,i} dt + b(X_t^n) dt + \sigma(X_t^n) dW_t, \quad Y_0^{n,i} = 0,$$

and the multifactor approximation of X as

$$X_t^n = u_0^n(t) + \sum_{i=1}^n c_i Y_t^{n,i},$$

which in integrated form yields

$$X_t^n = u_0^n(t) + \int_0^t K_n(t-s) b(X_s^n) ds + \int_0^t K_n(t-s) \sigma(X_s^n) dW_s.$$

Each factor $Y^{n,i}$ is Markovian with mean-reversion rate x_i , so that $(X^n, Y^{n,1}, \dots, Y^{n,n})$ is a finite-dimensional Markov process amenable to standard simulation techniques such as the classical Euler scheme (see Section 2.2.2). Under mild assumptions on b, σ and the convergence $K_n \rightarrow K$, one proves that X^n converges to X in probability or in \mathcal{L}^p uniformly on compacts as $n \rightarrow \infty$, providing an efficient simulation framework for rough volatility and more general non negative Volterra processes (Abi Jaber and El Euch, 2019; Abi Jaber et al., 2024). Extensions to general completely monotone kernels and further approximation results for stochastic Volterra equations are developed also in Alfonsi and Kebaier (2024).

4.3 Positive definiteness VS complete monotonicity

The key connection between these two properties is given by Schoenberg’s theorem for kernels in Φ_∞ (Sasvári, 2013, Theorem 3.8.5): a kernel K belongs to Φ_∞ if and only if $K(\sqrt{\cdot})$ is completely monotonic. In other words, $K(\|\cdot\|)$ is positive definite in \mathbb{R}^d for all $d \geq 1$, if and only if $K(\sqrt{\cdot})$ is the inverse Laplace transform of a finite nonnegative measure on $[0, \infty)$ (Sasvári, 2013, Theorem 3.9.8).

In addition, (Langrené et al., 2025) proved that if $K \in \Phi_\infty$, then $K(\|\cdot\|^\alpha)$ is also positive definite in all \mathbb{R}^d for all $\alpha \in (0, 1]$. Similarly, if K is completely monotonic, then $K(\cdot^\alpha)$ is also completely monotonic for all $\alpha \in (0, 1]$. Combining this with Schoenberg’s theorem yields the following equivalence: *$K(\|\cdot\|^\alpha)$ is positive definite in all \mathbb{R}^d for all $\alpha \in (0, 1]$ if and only if $K(\cdot^{\frac{\alpha}{2}})$ is completely monotonic on $[0, \infty)$ for all $\alpha \in (0, 1]$.*

This result clearly shows that working with positive definite kernels is more general than working with completely monotonic kernels: if a kernel K is completely monotonic, then it is also positive definite, but the converse is not necessarily true. Intuitively, “half of the powers are lost” when going from positive definite kernels $K(\|\cdot\|^\alpha)$ to completely monotonic kernels $K(\cdot^{\frac{\alpha}{2}})$. For example, the univariate kernels $K(u) = e^{-u^\alpha}$ (exponential power), $K(u) = (1 + u^\alpha)^{-\beta}$, $\beta > 0$ (generalized Cauchy), or $K(u) = u^{\frac{\alpha\beta}{2}} \mathcal{K}_\beta(\sqrt{2\beta}u^{\frac{\alpha}{2}})$, $\beta > 0$ (generalized Matérn, where \mathcal{K}_β is the modified Bessel function), are not completely monotonic when $\alpha \in (1, 2]$, yet are still positive definite for such values of α . As a result, such kernels can be well approximated by a sum of cosine functions (random Fourier features), but cannot be well approximated by a sum of exponential functions (random Laplace features).

Finally, if one considers kernel functions in $\Phi_d \setminus \Phi_\infty$, such functions, with either compact support or taking negative values, can still be well approximated by spectral sampling (Emery and Lantuéjoul, 2006) but not by a sum of exponential functions, which would necessarily be positive with unbounded support.

In particular, the isotropic S-fBM kernel $K(\mathbf{u}) = (1 - \|\mathbf{u}\|^\alpha) \mathbb{1}_{\{\|\mathbf{u}\| \leq 1\}}$ belongs to Φ_d only for $d = 1$ (when $\alpha \in]0, 1[$) and $d = 2$ (when $\alpha \in]0, \frac{1}{2}[$). As such, like any kernel with compact support, the S-fBM kernel is not completely monotonic and therefore cannot be well approximated by a sum of exponentials. Nevertheless, it can still be well approximated by a sum of cosine functions whenever the condition for positive definiteness is satisfied ($0 \leq \alpha \leq \frac{3-d}{2}$, see Theorem 4).

5 The log stationary fractional Brownian motion model

Here, we recall the definition of the Log S-fBM model. For that sake, we start by briefly recalling its main building block, namely the stationary fractional Brownian motion (S-fBM) model introduced in Wu et al. (2022), highlighting its main construction and properties.

The S-fBM process is built using the so-called time-scale domain

$$C_{l,T}(t^*) := \{(t, h) : h > l, |t - t^*| < \frac{1}{2} \min(h, T)\}, \quad (35)$$

and defined as:

$$\omega_{H,T}(t) = \mu_H + \int_{C_T(t)} dG_H, \quad (36)$$

where $C_T(t) := C_{0,T}(t)$ and dG_H is a centered non-homogeneous Gaussian white noise with variance measure

$$\mathbb{E}(dG_H(t, h)^2) = \lambda^2 \frac{h^{2H-2}}{T^{2H}} dt dh. \quad (37)$$

The constant μ_H is chosen such that $\mathbb{E}(e^{\omega_{H,T}(t)}) = 1$, yielding

$$\mu_H = -\frac{\nu^2}{4}. \quad (38)$$

The resulting process $(\omega_{H,T}(t))_t$ is a stationary Gaussian process with autocovariance

$$C_\omega(\tau) = \begin{cases} \frac{\nu^2}{2} \left(1 - \left(\frac{|\tau|}{T}\right)^{2H}\right), & |\tau| < T, \\ 0, & \text{otherwise,} \end{cases} \quad (39)$$

so that $\text{Var}(\omega_{H,T}(t)) = \nu^2/2$. Here, T plays the role of a correlation limit. The so-called intermittency parameter λ is related to ν and H as follows:

$$\nu^2 = \frac{\lambda^2}{H(1-2H)}, \quad H \in \left]0, \frac{1}{2}\right[. \quad (40)$$

Following [Bacry et al. \(2001a\)](#), [Wu et al. \(2022\)](#) define the associated multifractal random measure

$$M_{H,T}(dt) = \exp(\omega_{H,T}(t)) dt. \quad (41)$$

A key feature of the framework is its continuity at $H = 0$. As $H \rightarrow 0$, the measure $M_{H,T}$ converges weakly to the multifractal random measure of a Multifractal Random Walk (MRW) denoted $\tilde{M}_T(\cdot)$ as introduced in [Bacry et al. \(2001b,a\)](#); [Muzy et al. \(2000\)](#); [Muzy and Bacry \(2002\)](#). In fact, [Wu et al. \(2022\)](#) showed that

$$M_{H,T}(dt) \xrightarrow[H \rightarrow 0]{w} \tilde{M}_T(dt), \quad (42)$$

so that the S-fBM framework naturally unifies fractional ($H > 0$) and log-correlated ($H = 0$) regimes.

Finally, the Log S-fBM model is defined by subordinating a Brownian motion to the multifractal measure:

$$dX_t = \exp(\omega_{H,T}(t)) dB_t = \frac{M_{H,T}(dt)}{dt} dB_t, \quad (43)$$

where $(B_t)_t$ is a standard Brownian motion. This construction provides a flexible stochastic volatility model encompassing both rough and multifractal behaviors observed in empirical data.

In the upcoming sections, we derive the main ingredients to be able to RFF representation, namely the spectral density of the S-fBM covariance kernel, the sampling algorithm of the Random Features and the associated convergence guarantees. Before that, we chose to dedicate the following section for fixing the notations for the sake of clarity.

6 Spectral analysis of the S-fBM kernel

This section is devoted to a spectral analysis of the S-fBM kernel, which plays a central role both in characterizing its admissibility as a covariance function and in tailoring the Euler scheme with RFF representation. Since the kernel is radial, compactly supported and shift invariant, its spectral density is obtained as the Fourier transform of the covariance function in \mathbb{R}^d and admits explicit representations in terms of special

functions. In order to derive these representations and establish quantitative approximation results, we first introduce the necessary notations. We recall the Fourier transform convention adopted throughout the paper, together with the analytical tools required to handle radial Fourier transforms, including Bessel functions of the first kind and generalized hypergeometric functions. We also introduce suitable truncations of these series expansions, which will be instrumental in the construction of computable approximations of the spectral density and in the derivation of explicit error bounds. Working in arbitrary dimension $d \geq 1$ and focusing on the rough regime $H \in]0, \frac{1}{2}[$ relevant for applications, we express the S-fBM kernel in a normalized form that highlights its scaling properties and facilitates its spectral decomposition. The section then proceeds by establishing explicit spectral density formulas in both Bessel-series and hypergeometric forms, together with sharp uniform and \mathcal{L}^1 tail error estimates for their truncated counterparts, thereby quantifying the trade-off between dimensionality, truncation order and approximation accuracy. These results reveal a pronounced curse of dimensionality in the spectral domain, which is nevertheless mitigated by the exponential rate of convergence of the proposed truncation, a feature that is particularly relevant in high-dimensional and large-correlation-length regimes encountered in practice.

For any function $f \in \mathcal{L}^1(\mathbb{R}^d)$, we define its Fourier transform \hat{f} as:

$$\forall \boldsymbol{\omega} \in \mathbb{R}^d, \quad \hat{f}(\boldsymbol{\omega}) := \frac{1}{(2\pi)^d} \int_{\mathbb{R}^d} f(\mathbf{x}) e^{-i\boldsymbol{\omega}^T \mathbf{x}} d\mathbf{x}. \quad (44)$$

The Fourier transform \hat{f} is continuous and bounded. If \hat{f} also belongs to $\mathcal{L}^1(\mathbb{R}^d)$, then its inverse Fourier transform is given by

$$\forall \mathbf{x} \in \mathbb{R}^d, \quad f(\mathbf{x}) := \int_{\mathbb{R}^d} \hat{f}(\boldsymbol{\omega}) e^{i\boldsymbol{\omega}^T \mathbf{x}} d\boldsymbol{\omega} \quad (45)$$

Let J_ν denote the Bessel function of the first kind of order $\nu > 0$ (DLMF, 2025, 10.2.2):

$$J_\nu(z) = \sum_{n=0}^{\infty} \frac{(-1)^n (z/2)^{\nu+2n}}{n! \Gamma(n + \nu + 1)} \quad (46)$$

where $\Gamma(\cdot)$ is the Gamma function (DLMF, 2025, 5.2) defined for $\Re(z) > 0$ by

$$\Gamma(z) = \int_0^{\infty} t^{z-1} e^{-t} dt, \quad z \in \mathbb{C}$$

For any $(p, q) \in \mathbb{N}^2$, $(a_1, \dots, a_p), (b_1, \dots, b_q) \in \mathbb{R}^p \times \mathbb{R}^q$, we introduce the generalized hypergeometric function ${}_pF_q$ (DLMF, 2025, 16.2), defined by:

$${}_pF_q(a_1, \dots, a_p; b_1, \dots, b_q; z) = \sum_{n=0}^{\infty} \frac{(a_1)_n (a_2)_n \cdots (a_p)_n z^n}{(b_1)_n (b_2)_n \cdots (b_q)_n n!}, \quad (47)$$

where $(a)_n$ is the Pochhammer symbol (a.k.a. rising factorial):

$$(a)_n = a(a+1) \cdots (a+n-1) = \frac{\Gamma(a+n)}{\Gamma(a)}.$$

For any sequence $(a_n)_{n \in \mathbb{N}} \in \mathbb{R}^{\mathbb{N}}$ such that the following series h is absolutely convergent on $D \subset \mathbb{R}$,

$$\forall x \in D, \quad h(x) := \sum_{n=0}^{+\infty} a_n x^n, \quad (48)$$

we define its truncated version \hat{h}^N as:

$$\forall x \in D, \quad \hat{h}^N(x) := \sum_{n=0}^N a_n x^n. \quad (49)$$

Similarly, the truncated version of the Bessel function J_α and the generalized hypergeometric function are respectively:

$$\forall N \in \mathbb{N}, \quad \begin{cases} \widehat{J}_\alpha^N(x) := \sum_{m=0}^N \frac{(-1)^m}{m! \Gamma(m+\alpha+1)} \left(\frac{x}{2}\right)^{2m+\alpha} \\ \widehat{F}_q^N(a_1, \dots, a_p; b_1, \dots, b_q; z) := \sum_{k=0}^N \frac{(a_1)_k (a_2)_k \cdots (a_p)_k}{(b_1)_k (b_2)_k \cdots (b_q)_k} \frac{z^k}{k!}, \end{cases} \quad (50)$$

For the sake of generality, we choose to consider the S-fBM kernel defined in \mathbb{R}^d , $d \geq 1$ as follows:

$$C_\omega(\mathbf{x}) := \frac{\nu^2}{2} \left(1 - \left(\frac{\|\mathbf{x}\|}{T} \right)^{2H} \right) \mathbb{1}_{\{\|\mathbf{x}\| \leq T\}}, \quad \mathbf{x} \in \mathbb{R}^d \quad (51)$$

For any continuous functional $f : \mathbb{R}^d \rightarrow \mathbb{R}$ and any compact $\mathcal{K} \subset \mathbb{R}^d$, we denote:

$$\|f\|_\infty^{\mathcal{K}} := \sup_{x \in \mathcal{K}} |f(x)| \quad (52)$$

Similarly, we denote the truncated \mathcal{L}^1 norm for any arbitrary function $f \in \mathcal{L}^\infty(\mathbb{R}^d, \mathbb{R})$ and $r > 0$:

$$\|f\|_1^{\geq r} := \int_{\mathbb{R}^d \setminus B(0,r)} |f(\mathbf{x})| d\mathbf{x}. \quad (53)$$

where $B(r) := \{\mathbf{x} \in \mathbb{R}^d, \|\mathbf{x}\| \leq r\}$ is the centred ball of radius r . In the sequel, we consider $H \in]0, \frac{1}{2}[$ and $T > 0$.

6.1 Fourier transform of the S-fBM kernel

In this section, we explicitly derive the Fourier transform of the S-fBM kernel. When the parameters of the kernel are such that it is positive definite (see Subsection 6.2), then this Fourier transform is a probability density function, namely the spectral density of the S-fBM kernel. The first straightforward attempt is the following result, proved in Appendix A.2.

Proposition 2. *If $d \in 2\mathbb{N}^* \setminus \{1\}$, the following claims hold:*

1. *The spectral density of the S-fBM kernel admits the following representation:*

$$\forall \mathbf{c} \in \mathbb{R}^d, \quad g_\omega(\mathbf{x}) = \frac{\lambda^2 T^d}{H(1-2H)} \left[\frac{J_{\frac{d}{2}}(T\|\mathbf{x}\|)}{(T\|\mathbf{x}\|)^{\frac{d}{2}}} - T^{1-\frac{d}{2}} \sum_{m=0}^{\infty} \frac{(-1)^m}{m! \Gamma(m + \frac{d}{2})} \frac{(T\|\mathbf{x}\|/2)^{2m}}{2H + d + 2m} \right] \quad (54)$$

2. *For any $N \in \mathbb{N}$ and any compact $\mathcal{K} \subset \mathbb{R}^d$, there exist a positive constant C such that:*

$$\|\hat{g}_\omega^N - g_\omega\|_\infty^{\mathcal{K}} \leq \frac{(TC/2)^{2N}}{N! \Gamma(N + \frac{d}{2}) (N + \frac{d}{2})} \left(\left(\frac{TC}{2} \right)^{\frac{d}{2}} + 1 \right) \quad (55)$$

where:

$$\forall \mathbf{x} \in \mathbb{R}^d, \quad \hat{g}_\omega^N(\mathbf{x}) = \frac{\lambda^2 T^d}{H(1-2H)} \left[\frac{\widehat{J}_{\frac{d}{2}}^N(T\|\mathbf{x}\|)}{(T\|\mathbf{x}\|)^{\frac{d}{2}}} - T^{1-\frac{d}{2}} \sum_{m=0}^N \frac{(-1)^m}{m! \Gamma(m + \frac{d}{2})} \frac{(T\|\mathbf{x}\|/2)^{2m}}{2H + d + 2m} \right] \quad (56)$$

where the truncated version of the Bessel function $\widehat{J}_{\frac{d}{2}}^N$ is defined as in Eq. (50).

A particular derivation of Eq. (54) where $d = 1$ is developed in Appendix A.1.

Besides, the spectral density admits a representation denoted f_ω using the Hypergeometric function, more suitable for simulation purposes, which is the object of the following theorem proved in Appendix A.3.

Theorem 3. *The spectral density f_ω satisfied the following:*

1.

$$f_\omega(\mathbf{x}) = \frac{\nu^2 T^d / 2}{2^d \pi^{\frac{d}{2}} \left(\frac{d}{2H} + 1\right) \Gamma\left(\frac{d}{2} + 1\right)} {}_1F_2\left(\frac{d}{2} + H; \frac{d}{2} + H + 1, \frac{d}{2} + 1; -\frac{\|\mathbf{x}\|^2 T^2}{4}\right), \quad \mathbf{x} \in \mathbb{R}^d, \quad (57)$$

2. *For any compact $\mathcal{K} \subset \mathbb{R}^d$, the error bound holds:*

$$\forall N \in \mathbb{N}^*, \quad \left\| \hat{f}_\omega^N - f_\omega \right\|_\infty^{\mathcal{K}} \leq \frac{\nu^2 T^d / 2}{2^d \pi^{\frac{d}{2}} \left(\frac{d}{\alpha} + 1\right) \Gamma\left(\frac{d}{2} + 1\right)} \frac{C}{e(2Cr(\mathcal{K})e(N-1) - 1)(N-1)^{2Cr(\mathcal{K})e(N-1) - 1}} \quad (58)$$

where C is a positive constant and $r(\mathcal{K}) = \sup_{\mathbf{x} \in \mathcal{K}} \|\mathbf{x}\|$ the radius of \mathcal{K} .

These results reveal a curse of dimensionality. A fortiori when T is significant which is the case in financial applications see for instance the experiments reported in [Muzy et al. \(2013\)](#), Figures 8 and 9 in the context of MRW model. However, the exponential speed of convergence compensate this effect.

The exponential speed is also retrieved in the error related to the truncated norm as showcased in the following result.

Proposition 3. *The following claim holds:*

$$\forall r > 0, \quad \left\| \hat{f}_\omega^N - f_\omega \right\|_1^{>r} \leq \frac{\Omega_d C(T, d, \nu, H)}{T^d} \frac{(Tr + \kappa(d))^d - Tr^d}{d\kappa(d)} e^{-Tr} \quad (59)$$

where:

- $\Omega_d = \frac{2\pi^{\frac{d}{2}}}{\Gamma\left(\frac{d}{2}\right)}$
- $\kappa(d) = \begin{cases} \gamma(d+1)^{\frac{1}{d-1}}, & \text{if } d > 1, \\ e^{1-\gamma}, & \text{if } d = 1 \end{cases}$
- $\gamma \approx 0.577$ is the Euler constant
- $C(T, d, \nu, H) = A \left(\frac{T^2}{2}\right)^{\frac{d}{2}} \frac{\nu^2}{\Gamma\left(\frac{d}{2}\right)} \frac{d+H}{d(d+H)}$, A is a positive constant.

The proof is in Appendix A.4.

This means that the truncated L^1 norm of the truncation error decays exponentially in r , with an algebraic prefactor.

6.2 Positive definiteness of the S-fBM kernel

Here, we investigate the positive definiteness of the kernel underlying the S-fBM construction, a property that is essential for its interpretation as a valid covariance function in Euclidean space. Since positive definiteness is tightly linked to the non-negativity of the associated spectral density, our analysis relies on Fourier-analytic arguments and classical results on radial kernels. We provide a complete characterization of the admissible values of the smoothness parameter as a function of the ambient dimension d , thereby identifying the precise regimes in which the S-fBM kernel is well-posed.

Theorem 4. *The isotropic S-fBM kernel $K(\|\mathbf{u}\|) = \frac{\nu^2}{2} \left(1 - \left(\frac{\|\mathbf{u}\|}{T}\right)^{2H}\right) \mathbb{1}_{\{\|\mathbf{u}\| \leq T\}}$, $\mathbf{u} \in \mathbb{R}^d$, $\nu > 0$, $T > 0$, $H > 0$, is positive definite in \mathbb{R}^d if and only if $0 < H \leq \frac{3-d}{4}$.*

Proof. Since a linear rescaling does not affect positive definiteness, it is sufficient to prove that the standardized kernel $K_\alpha(\|\mathbf{u}\|) := (1 - \|\mathbf{u}\|^\alpha) \mathbb{1}_{\{\|\mathbf{u}\| \leq 1\}}$ is positive definite if and only if $0 < \alpha \leq \frac{3-d}{2}$. The Fourier transform \hat{K}_α of K_α is given by equation (57) with $\alpha = 2H$ and $T = 1$. According to Bochner's theorem, K_α is positive definite in \mathbb{R}^d if and only if $\hat{K}_\alpha(\mathbf{x}) \geq 0$ for all $\mathbf{x} \in \mathbb{R}^d$. Remark that K_α coincides with the function $I_{\delta, \mu, \nu, \alpha}(t)$ in Zastavnyi (2006, equation (9) page 1187) with the change of notation $(\delta, \mu, \nu, \alpha, t) = (\alpha, 2, \frac{d-1}{2}, d-1, \|\mathbf{x}\|)$. Now, Zastavnyi (2006, Theorem 5) gives conditions under which \hat{K}_α takes negative values. In our situation, Zastavnyi (2006, Theorem 5.3(i)) applies and yields the fact that K_α is not positive definite in \mathbb{R}^d if $\alpha > (3-d)/2$. Since $\alpha > 0$, this means that the S-fBM kernel can only be positive definite in the cases $d = 1$ or $d = 2$. When $d = 1$, K_α is positive definite if and only if $\alpha \in (0, 1]$ (Wu et al., 2022). When $d = 2$ and $\alpha = 1/2$, \hat{K}_α is given by $\frac{1}{20\pi} {}_1F_2\left(\frac{5}{4}; \frac{9}{4}, 2; -\frac{\|\mathbf{x}\|^2}{4}\right)$, which is non-negative according to Cho and Yun (2018, Theorem 5.1), see also the diagram Cho and Yun (2018, Figure 2). From Bochner's theorem, this shows that $K_{1/2}$ is positive definite in \mathbb{R}^2 . Since Zastavnyi (2006, Theorem 5.3(i)) shows that K_α is not positive definite in \mathbb{R}^2 when $\alpha > 1/2$, we can use the characterization of the parameter space in Golubov (1981) to conclude that K_α is positive definite in \mathbb{R}^2 for every $\alpha \in (0, 1/2]$. This concludes the proof. \square

Theorem 4 shows that the isotropic S-fBM kernel can only be positive definite when $d = 1$ or $d = 2$. For $d = 1$, the positive definiteness condition is $0 < H \leq \frac{1}{2}$, corresponding to the rough volatility regime already well documented in the literature (Gatheral et al., 2018; Bayer et al., 2016; Wu et al., 2022). For non explosiveness consideration of the S-fBM variance (see Eq. (40) and Eq. (39)) the admissible range of positive definiteness becomes $0 < H < \frac{1}{2}$.

6.3 Error bounds of the RFF scheme from Algorithm 3

6.3.1 Monte Carlo convergence rate

The Markovian structure of the HMC described in Section 3.2.1 is useful to derive a convergence bound of the RFF representation toward its true value. In the following result, we consider the problem of estimating the empirical kernel representation of Eq. (14).

We denote here \hat{X} the Hamiltonian Markov process whose ergodic distribution is $\hat{\pi}$ defined up to a multiplicative constant times \hat{f}_ω^N the spectral density, for an arbitrary truncation order $N > 0$, obtained via hypergeometric function's truncation (see Section 6.1).

Without loss of generality, we introduce for any function $h : \mathcal{X} \rightarrow [a, b]$ where $\mathcal{X} \subset \mathbb{R}^d$ and reals $a \leq b$ the empirical and theoretical means:

$$\begin{cases} \hat{\mu}_M = \frac{1}{M} \sum_{i=1}^M h(\hat{X}_i) \\ \mu_M = \frac{1}{M} \sum_{i=1}^M h(Y_i) \\ \mu = \mathbb{E}(h(\eta)) \end{cases} \quad (60)$$

where \hat{X} and Y are the Markov processes with ergodic distribution, defined up to a multiplicative constant, of \hat{f}_ω^N and f_ω respectively.

We present the following convergence guarantees demonstrated in Appendix D.1 with explicit bound.

Theorem 5. *There exist positive constants C and C_Ψ such that for any arbitrary positive real number R the following guarantee holds:*

$$\mathbb{P}(|\hat{\mu}_M - \mu| \geq t) \leq \exp\left(-\frac{Mt^2}{8Cv} + C\Psi_N(T, \nu, d, H, C_\Psi)\right), \quad (61)$$

where:

$$\Psi_N(T, \nu, d, H, C_\Psi) := \left[\left(\frac{T^2}{2} \right)^{\frac{d}{2}} \frac{\nu^2}{\Gamma(\frac{d}{2})} \left(\frac{1}{d} \left(\frac{eT^2}{4} \right)^N \frac{1}{e^{\frac{d}{2} + 1}_N} \right. \right. \\ \left. \left. + \frac{1}{d + 2H} \frac{C_\Psi}{e^{(2C_\Psi\sqrt{N}e(N-1) - 1)(N-1)2C_\Psi\sqrt{N}e(N-1) - 1}} \right) \right. \\ \left. + \frac{\Omega_d C_\omega}{T^d} \frac{(T\sqrt{N} + \kappa(d))^d - TN^{\frac{d}{2}}}{d\kappa(d)} e^{-T\sqrt{N}} \right].$$

$$v := \frac{(b-a)^2}{4} \left(1 + \frac{8\rho}{1-\rho} \right),$$

- $\rho \in [0, 1]$ is the ergodicity parameter of the underlying Markov process introduced in Lemma 2.

This theorem provides a non-asymptotic concentration bound for the Monte Carlo estimator $\hat{\mu}_M$ obtained from the HMC sampler in the case of the S-fBM kernel. It states that the probability that the estimator converges in probability to the true quantity μ exponentially fast with the number of samples M . The leading term in the exponent is of Gaussian type and reflects the effective variance of the estimator, which depends on the range of the test function and on the geometric ergodicity of the underlying Markov chain through the parameter ρ . The additional correction term $\Psi_N(T, \nu, d, H, C_\Psi)$ captures finite-dimensional and approximation effects arising from truncation, discretization and spectral properties of the underlying S-fBM kernel; importantly, this term does not depend on M but on N the order of truncation of the S-fBM spectral density.

Overall, the result shows that HMC achieves reliable statistical accuracy at an exponential rate in the sample size, with explicit constants that quantify both the mixing properties of the chain and the complexity of the target model.

Similarly, one can derive a \mathcal{L}^p error bound which proof is in Appendix D.2.

Corollary 1. *The p^{th} order moment of the discrepancy error satisfies:*

$$\|\hat{\mu}_M - \mu\|_{\mathcal{L}^p} \leq e^{C \frac{\Psi_N(T, \nu, d, H, C_\Psi)}{p}} \left(\Gamma\left(1 + \frac{p}{2}\right) \right)^{\frac{1}{p}} \left(\frac{1}{8Cv} M \right)^{-\frac{1}{2}}, \quad p > 0 \quad (62)$$

where C is a positive constant.

This inequality shows that the p^{th} moment of the estimation error decays at the standard Monte Carlo rate $M^{-\frac{1}{2}}$ as the number of samples M increases. Importantly, this correction grows at most exponentially with $1/p$ and does not affect the asymptotic rate in M . Overall, the bound confirms that HMC achieves the optimal root- M convergence rate in \mathcal{L}^p , with explicit constants that quantify the influence of the chain's dependence structure.

In the upcoming section, we tackle the accelerated numerical simulation scheme of Volterra processes with RFF. First, we go through the main accelerated simulation method focusing on its advantages. Then, we derive quantitative estimates of the developed numerical scheme with explicit bounds for an arbitrary kernel.

6.3.2 Error bounds

The following results quantify the propagation of errors using the scheme of Eq. (26) in the particular case of the S-fBM kernel leveraging the previous theoretical guarantees. As already mentioned, Theorem 2 and Proposition 1 proved in Appendix C.3, provides a \mathcal{L}^p bound on the discrepancy between respectively the Euler scheme X_N , its random feature approximation X_N^M and the true solution X . Now we conduct a similar analysis to derive the corresponding bounds in the case of the S-fBM kernel.

Theorem 6. *If σ satisfies \mathcal{H}_1 , \mathcal{H}_2 and \mathcal{H}_3 , then for any arbitrary compact $\mathcal{K} \subset \mathbb{R}_+$, $p > 0$ and $\varepsilon \in \left] \frac{1}{p}, \alpha \wedge 1 \right[$ there exists a positive constant $C_{\mathcal{K}}^p > 0$ such that for any $M \in \mathbb{N}$ and $t \in \mathcal{K}$:*

$$\sup_{s \in [0, t]} \mathbb{E}[|X_s - X_N^M(s)|^p] \leq K_p^1 \left(\left(1 + \mathbb{E}[|X_0|^p]\right) \delta_N^{p(\alpha \wedge 1) - \varepsilon} + e^{C_p^1(\Psi_N(T, \nu, d, H, C_\Psi) + t)} \Gamma\left(1 + \frac{p}{2}\right) \left(\frac{1}{8C_2 v} M\right)^{-p/2} \right) \quad (63)$$

The proof is in Appendix D.3.

In the same line as Proposition 1, Theorem 6 establishes a strong \mathcal{L}^p -error estimate for the approximation X_N^M of the process X . Again, the error naturally decomposes into two contributions: the first term, of order $\delta_N^{p(\alpha \wedge 1) - \varepsilon}$, corresponds to the time discretization approximation, while the second term reflects the leapfrog iteration approximation of the HMC sampling via the exponential factor involving $\Psi_N(T, \nu, d, H, C_\Psi)$ and t as well as the characteristic rate $M^{-p/2}$ of Euler-type schemes driven by Gaussian increments. Overall, the theorem provides explicit convergence rates in both approximation parameters and quantifies the interplay between time discretization, the leapfrog iteration and the proper HMC sampling.

7 Numerical experiments

7.1 RFF approximation of the S-fBM kernel

7.1.1 Goodness of fit

The first numerical step consists in validating the accuracy of the spectral density representation given in Eq. (57). In Figure 8 of Appendix E.1, we benchmark the one dimensional case ($d = 1$) by comparing the analytical formula in Eq. (57) with a reference obtained through numerical Fourier integration using the Simpson integration scheme. The results exhibit an excellent agreement between the two approaches, with discrepancies remaining at the level of machine precision. This demonstrates that the observed error is not induced by the modelling assumptions or the numerical integration procedure, but is instead attributable to the intrinsic limitations of floating point arithmetic.

We further extend this validation to the two-dimensional setting by examining the accuracy of the corresponding spectral density representation against numerical Fourier integration. The surface plot displays the pointwise difference over the frequency domain, offering a global view of the approximation error, while the associated color map representations emphasize its spatial structure and magnitude. In all cases, the discrepancies are again confined to machine precision, confirming that the proposed representation accurately reproduces the spectral density in both one and two dimensions. Consequently, the representation can be regarded as numerically exact for practical purposes, with residual errors entirely dominated by floating point rounding effects.

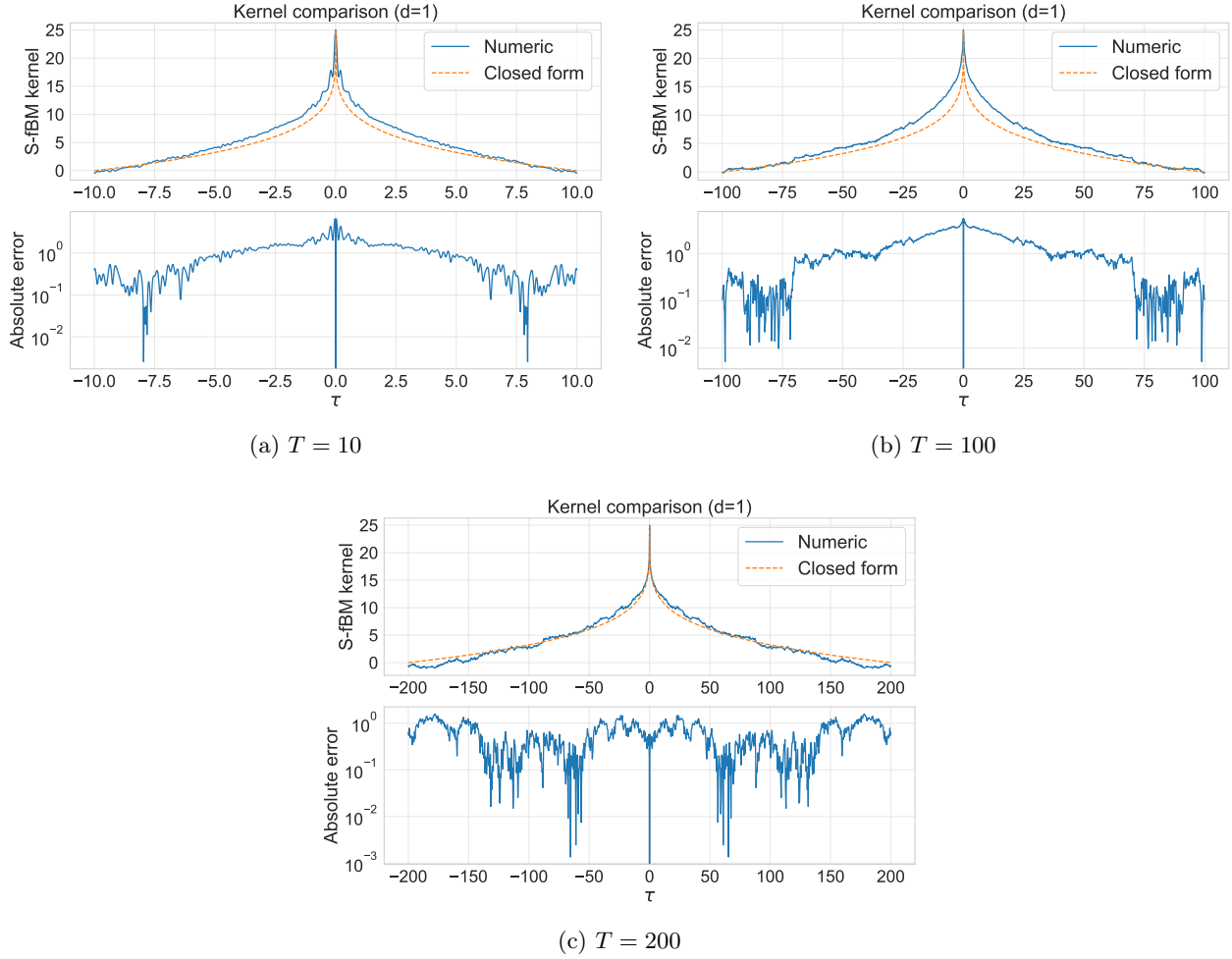
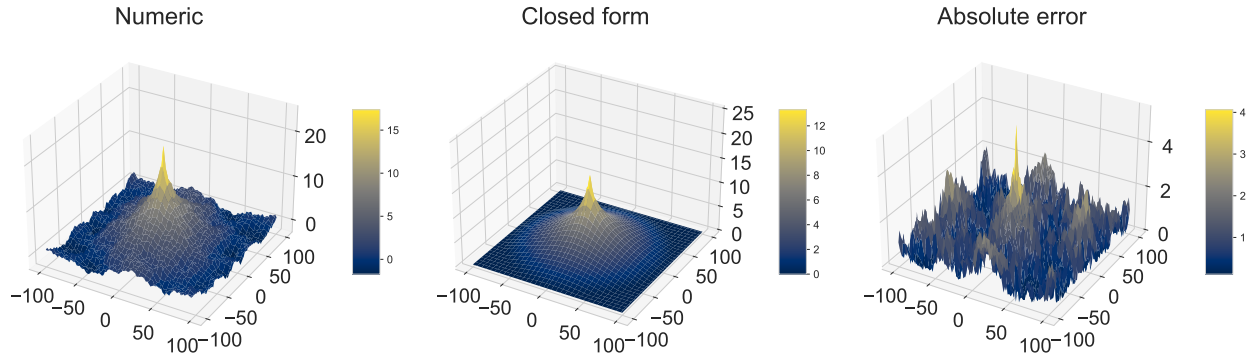
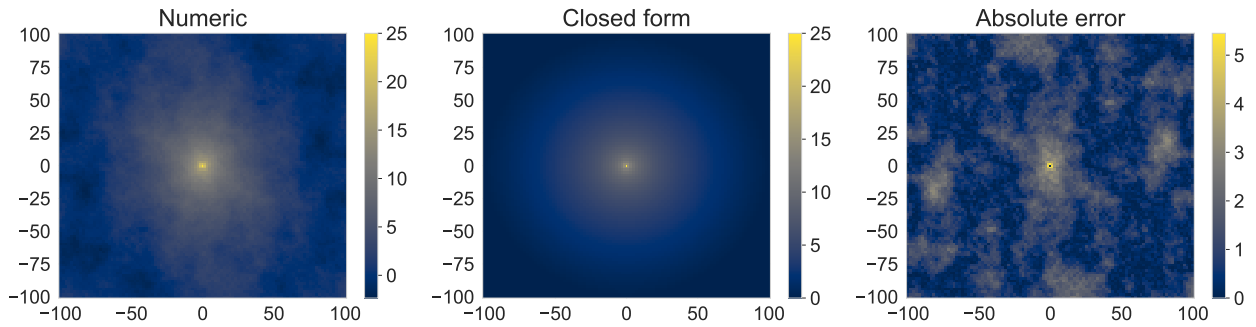


Figure 1: S-fBM kernel approximation using the RFF representation for different correlation limits T together with the absolute error between the approximated and theoretical kernel. The number of spectral Monte Carlo simulations is $M = 8000$, with $\nu^2 = 50$ and $H = 0.1$. The top panels correspond to $T = 10$ and $T = 100$, while the bottom panel corresponds to $T = 200$.

Figure 1 illustrates the accuracy of the kernel approximation obtained via the Random Fourier Features (RFF) representation for different correlation limits T . The results are based on Monte Carlo experiments in which the underlying latent variables were sampled using the HMC procedure described in the Section 3.2. The figure compares the behavior of the kernel error across increasing values of T , highlighting the impact of the sample size on the quality of the RFF-based approximation.



(a) Kernel approximation error surface



(b) Corresponding colormap representation

Figure 2: Two dimensional visualization of the S-fBM kernel approximation error obtained using the RFF representation. Results are based on $M = 8000$ Monte Carlo simulations with parameters $\nu^2 = 50$ and $H = 0.1$. The top panel shows the error surface, while the bottom panel displays the corresponding colormap both for $T = 100$.

In Figure 2 presents a two dimensional visualization of the kernel approximation error obtained using again the RFF representation. The results are computed from $M = 8000$ spectral Monte Carlo simulations with parameters $\nu^2 = 50$ and $H = 0.1$, where the latent variables are sampled using the Hamiltonian Monte Carlo (HMC) scheme introduced in the previous section. The top panel displays the error surface as a function of the time lags, providing a global view of the approximation accuracy, while the bottom panel shows the corresponding colormap representation, which emphasizes the spatial variability and magnitude of the error. Together, these visualizations offer complementary insights into the structure and intensity of the approximation error for a fixed sample size $T = 100$.

7.1.2 Parameters retrieval

The aim of this section is to verify the good retrieval of the S-fBM parameters from the RFF representation of its kernel. We recall the so-called Generalized Method of Moments (GMM) framework for the estimation of the parameters of the S-fBM model based on autocovariance information evaluated at a finite collection of time lags. For a fixed integer $Q \in \mathbb{N}$, we consider a prescribed sequence of lags $\mathcal{T}_Q = (\tau_l)_{l \in [1, Q]}$ and formulate the GMM estimator as the minimizer of a quadratic discrepancy between empirical and theoretical moment conditions. The latter are defined through the autocovariance function associated with RFF representation of the S-fBM model, leading to a tractable contrast function on the feasible parameter domain Ξ . This yields an approximated GMM estimator $\hat{\theta}_M$ constructed from M independent samples of the random features. We finally state a non-asymptotic error bound for this estimator, which quantifies the impact of the random feature approximation.

In this subsection we focus on the case $d = 1$. We denote, for a fixed $Q \in \mathbb{N}$, $\mathcal{T}_Q := (\tau_l)_{l \in [1, Q]}$ a sequence of time lags. The Generalized Method of Moments can be formulated as follows:

$$\theta = \arg \min_{\mathbf{x} \in \Xi} \mathbf{h}(\mathbf{x})^T W \mathbf{h}(\mathbf{x}) \quad (64)$$

where $\Xi = [0, 1] \times]0, \frac{1}{2}[\times \mathbb{R}_+$ stands for the feasible domain of the vector of true S-fBM parameters $\theta^* := (\lambda^2, H, T)$, the map $\mathbf{h} : \Xi \mapsto \mathbb{R}^Q$ represents the discrepancy between the empirical and theoretical kernel and $W \in \mathbb{R}^{Q \times Q}$ is a symmetric positive definite matrix.

Herein, we consider the discrepancy function being parameterised by the spectral density representation considered:

$$\mathbf{h}(\mathbf{x}) = \mathbf{C} - \mathbf{C}(\mathbf{x}) \quad (65)$$

where :

- $\mathbf{C} = (C_\omega(\tau), \tau \in \mathcal{T}_Q)$ is the observed autocovariance function across the time lags.
- $\mathbf{C}(\mathbf{x}) = (C_\omega(\tau)(\mathbf{x}), \tau \in \mathcal{T}_Q)$ is the theoretical autocovariance function across the same time lags.

We introduce the approximated version of the GMM solution:

$$\hat{\theta}_M = \arg \min_{\mathbf{x} \in \Xi} \hat{\mathbf{h}}_M(\mathbf{x})^T W \hat{\mathbf{h}}_M(\mathbf{x}) \quad (66)$$

where:

$$\begin{cases} \hat{\mathbf{h}}_M(\mathbf{x}) = \hat{\mathbf{C}}_M - \mathbf{C}(\mathbf{x}) \\ \hat{\mathbf{C}}_M = (\hat{C}_\omega^M(\tau), \tau \in \mathcal{T}_Q) \\ \hat{C}_\omega^M(\tau) = \frac{K(0)}{M} \sum_{m=1}^M \cos(\eta_m \tau) \end{cases} \quad (67)$$

\hat{C}_ω^M represents the empirical counterpart of $K(0)\mathbb{E}[\cos(\eta\tau)]$ with $\eta_1, \eta_2, \dots, \eta_M$ being M independent and identically distributed copies of η drawn from the spectral density of the autocovariance function \mathbf{C} .

For any matrix $M \in \mathbb{R}^{Q \times Q}$, we consider the matrix norm:

$$\|M\| := \sup_{x \in \mathbb{R}^Q} \frac{\|Mx\|_2}{\|x\|_2}$$

where for any $x \in \mathbb{R}^Q$, $\|x\|_2 = \sqrt{\sum_{i=1}^Q x_i^2}$ is the Euclidean norm of x . We also introduce the l^∞ matrix norm for any $M \in \mathbb{R}^{Q \times Q}$:

$$\|M\|_\infty := \sup_{1 \leq i, j \leq Q} |M_{i,j}|$$

Theorem 7. *There exists a positive constant K_W such that:*

$$\left\| \hat{\theta}_M - \theta^* \right\|_{\mathcal{L}^2} \leq K_W \|W\| \sqrt{\frac{Q}{M}} \quad (68)$$

The proof is in Appendix E.2.

Theorem 7 shows that the estimation error decays at rate $M^{-1/2}$, up to explicit constants depending on the weighting matrix and the number of moments. This corresponds to the speed of convergence of the central limit theorem coming from the Monte Carlo RFF approximation.

Now, we leverage the GMM method to re-estimate the S-fBM parameter taking as observed data the RFF representation of the kernel obtained via the sampling procedure described in Section 3.1. For each fixed parameters H, λ^2, T , we construct of sample of 50 estimates of respectively the Hurst exponent and intermittency parameter denoted \hat{H} and $\hat{\lambda}^2$. We do not focus on estimating the correlation limit T as it is intractable in practice as illustrated in the numerical experiments of [Muzy et al. \(2013\)](#). In the Table 1, we report the mean value and the standard deviation of each estimate with respect to each configuration of chosen parameters.

$\lambda^2 = 0.02$	$H = 0.04$	$H = 0.1$	$H = 0.3$
$T = 100$			
\hat{H}	0.0488(0.0583)	0.0962(0.0256)	0.2982(0.0320)
$\hat{\lambda}^2$	0.0350(0.0097)	0.0229(0.0027)	0.0199(0.0013)
$\lambda^2 = 0.04$			
$T = 200$			
\hat{H}	0.0417(0.0186)	0.1028(0.0180)	0.3033(0.0523)
$\hat{\lambda}^2$	0.0686(0.0146)	0.0458(0.0038)	0.0383(0.0051)
$\lambda^2 = 0.06$			
$T = 400$			
\hat{H}	0.0417(0.0232)	0.1020(0.0245)	0.3530(0.1095)
$\hat{\lambda}^2$	0.0999(0.0145)	0.0676(0.0077)	0.0406(0.0239)
$\lambda^2 = 0.08$			
$T = 600$			
\hat{H}	0.0409(0.0195)	0.1030(0.0379)	0.4210(0.2206)
$\hat{\lambda}^2$	0.1317(0.0245)	0.0893(0.0120)	0.1085(0.2312)

Table 1: Estimated mean and standard deviation obtained from 50 independent samples of estimated Hurst and intermittency parameters where $M = 50000$ using the time lag sequence $\{\tau_k = \lfloor 2^{\frac{k}{2}} \rfloor, k = 0, \dots, Q\}$ and $Q = 19$

We observe that the retrieval of the true parameters works well in most situations. For small H values, a small bias in $\hat{\lambda}^2$ is noticed particularly when T is large as it introduces long range dependence, making the kernel highly sensitive to low frequency behaviour and boundary effects. Second, cosine components are inherently oscillatory which can lead to strong multicollinearity among parameters particularly when H and λ^2 are of the same order of magnitude as they are both involved in the variance formula of the S-fBM process. Apart this configuration, the retrieval is done well with a decent accuracy.

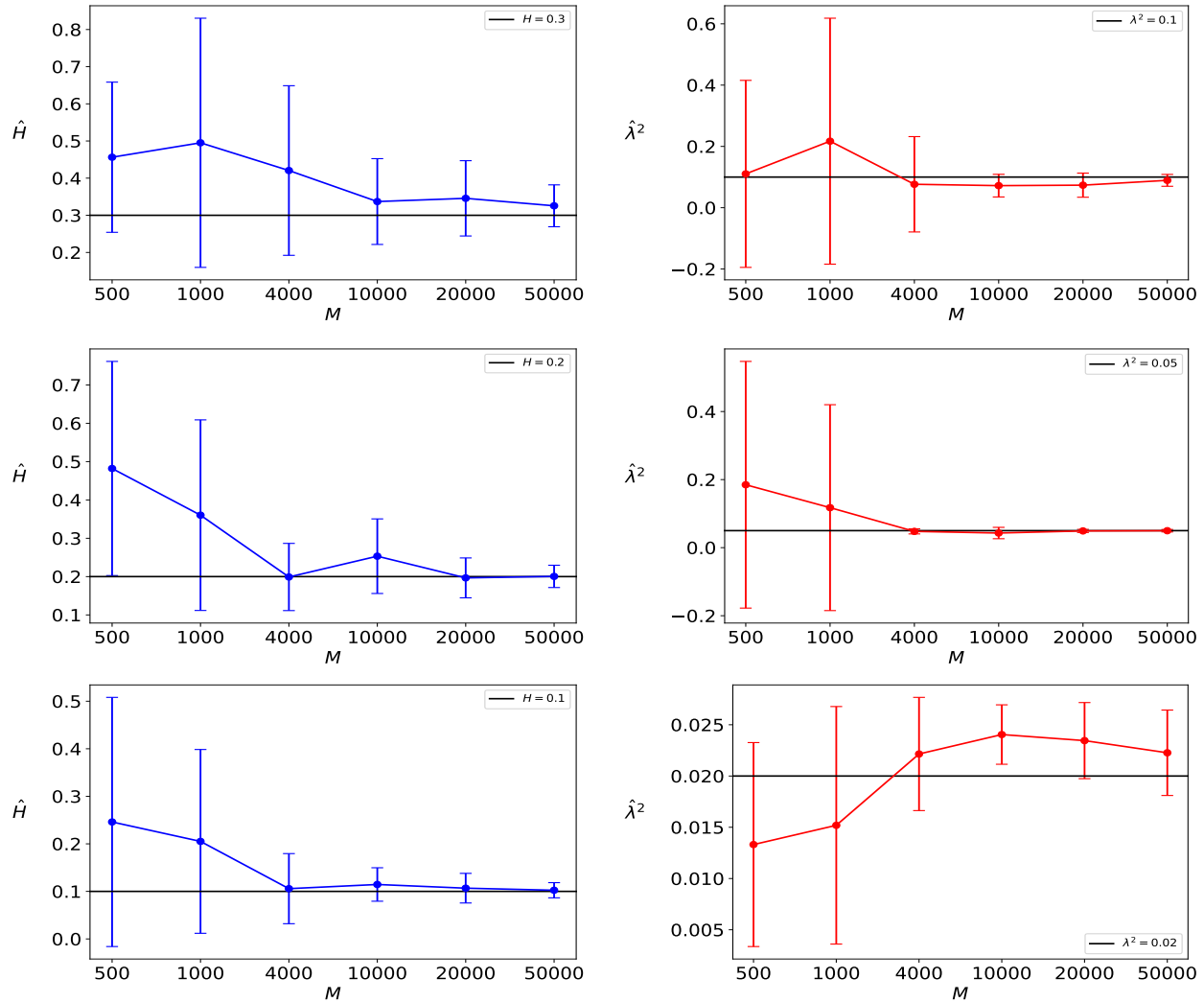


Figure 3: Using the RFF representation of the S-fBM kernel for different sampling realizations M , we plot the mean value and the associated 95% confidence interval from a sample of 20 copies of the Hurst exponent (**blue**) and the estimated intermittency parameter (**red**) together with error bars compared with the respective theoretical values: $H = 0.1, \lambda^2 = 0.02$ (**bottom**) $H = 0.2, \lambda^2 = 0.05$ (**middle**) and $H = 0.3, \lambda^2 = 0.1$ (**top**). Here $T = 200$ and the time lag sequence used is $\{\tau_k = \lfloor 2^{\frac{k}{2}} \rfloor, k = 0, \dots, Q\}$ where $Q = 19$.

Figure 3 illustrates the estimation of the Hurst exponent H and the intermittency parameter λ^2 from the RFF representation of the S-fBM kernel for different spectral sampling sizes M . For each value of M , the mean estimates and the associated 95% confidence intervals are computed from a sample of 20 independent copies and compared with the corresponding theoretical values. The three panels correspond to increasing levels of regularity and intermittency. As M increases, both estimators converge toward their theoretical values and the confidence intervals shrink, indicating that the estimation procedure becomes increasingly unbiased and more precise.

7.2 RFF acceleration of SVE simulation

This section is devoted to the numerical investigation of RFF techniques as a means of accelerating the simulation of SVEs. We begin by examining the qualitative impact of the RFF kernel approximation on the simulated trajectories by comparing sample paths generated via an Euler discretization with and without

RFF. We then turn to a quantitative assessment of computational efficiency, where average execution times are reported as a function of the number of time steps, allowing for a direct comparison between the classical Euler scheme and its RFF-based counterpart, both with and without internal feature sampling. Finally, we investigate the accuracy of the proposed method through a weak and strong error analysis. Weak errors are evaluated for smooth test functions under different coupling scenarios of the driving Brownian motions, while strong errors are analyzed in \mathcal{L}^p norms for several values of p , with particular attention paid to disentangling the contribution of the RFF approximation from that of stochastic regularization. Together, these experiments provide a comprehensive assessment of the trade-off between computational speed-up and numerical accuracy induced by the RFF approximation.

Figure 4 compares examples of sample paths simulated by the Euler discretization scheme (Algorithm 1) with the paths simulated by the RFF-Euler scheme (Algorithm 3). To isolate the effect of the kernel approximation, both trajectories are generated using the same underlying Brownian path and identical numerical parameters, with only the value of H varying between the two panels. This controlled setting allows for a direct comparison of the resulting paths and highlights the influence the RFF approximation.

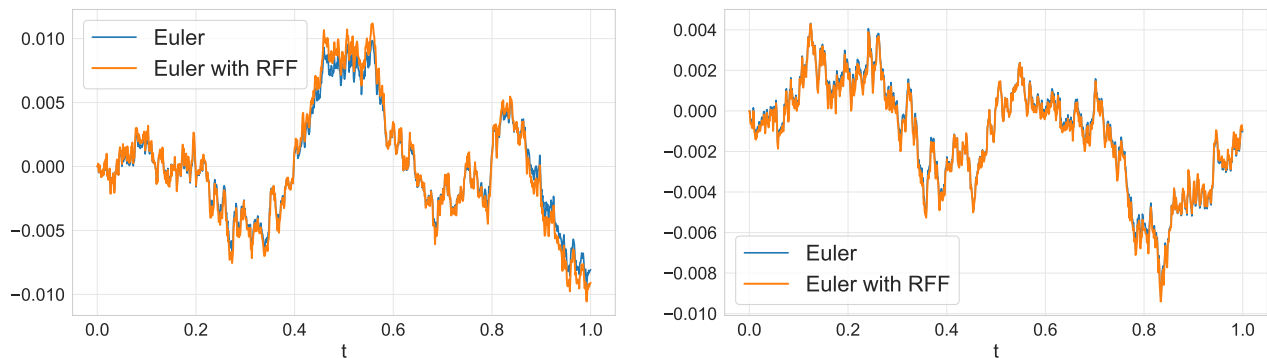


Figure 4: Sample paths generated using the Euler scheme with VS without the RFF approximation, driven by the same underlying Brownian path to facilitate comparison, with $H = 0.1$ (left) and $H = 0.2$ (right). The parameters considered are $\lambda^2 = 0.01$, $T = 100$ and $M = 10,000$. The volatility function is given by $\sigma(t, x) = 0.3(1 + 0.1x)$. The simulation uses 1000 time steps over the interval $[0, 1]$.

One can observe that the Euler and RFF-Euler are very close to each other everywhere, and that the error between the two is lower for $H = 0.2$ compared to $H = 0.1$. The fact that the error increases when H decreases is what is expected theoretically, since in the upper bound of Eq. (62), the function Ψ_N increases as H decreases. Intuitively, the fact that the \mathcal{L}^p error between the S-fBM kernel and its RFF approximation increases when H decreases is tied to the difficulty to approximate the kernel near zero for small H , which affects the decay of the spectral density.

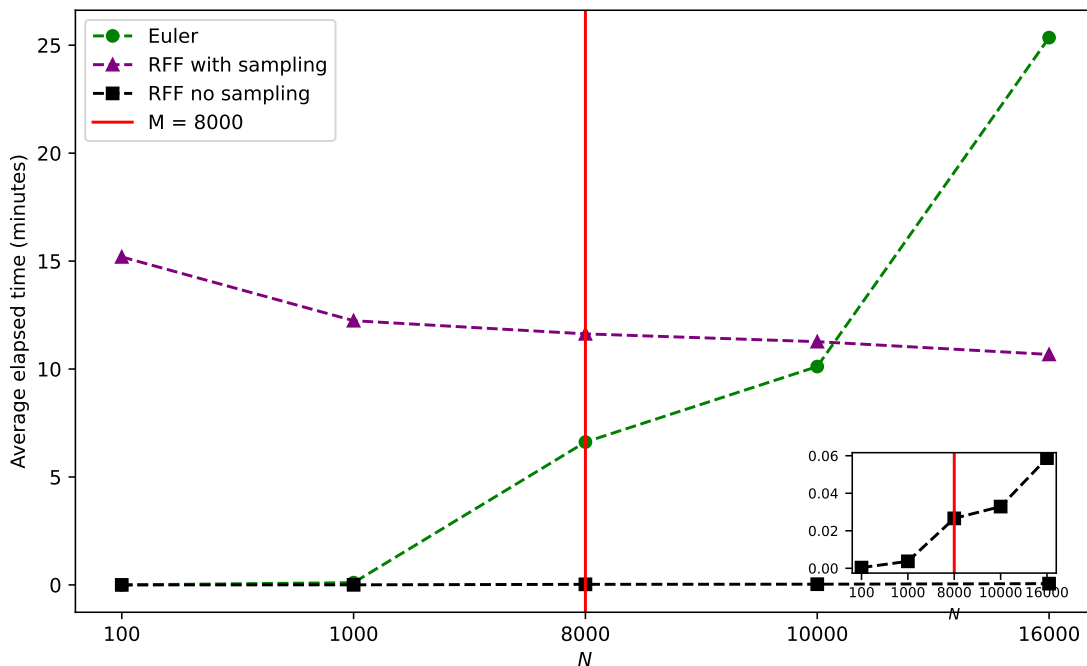


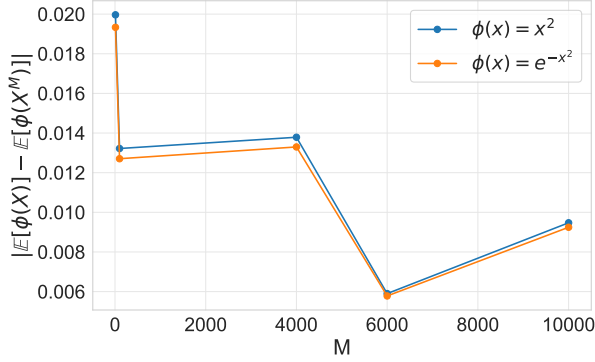
Figure 5: Average elapsed time over 20 runs as a function of the number of time steps N for the classical Euler scheme (**green**) and the RFF-Euler scheme, respectively, both including (**purple**) and excluding (**black**) the random features sampling. The parameters considered are $H = 0.1$, $\lambda^2 = 0.01$, $T = 100$ and $M = 8000$. The volatility function is given by $\sigma(t, x) = 0.3(1 + 0.1x)$. This is performed within a CPU-only job on a single node with 10 cores.

Figure 5 compares the computational cost of the Euler simulation scheme implemented with and without RFF sampling performed inside the algorithm. Both implementations are evaluated under identical numerical conditions, using the same underlying Brownian path. The experiment is designed to assess the impact of internal RFF sampling on the overall execution time and to quantify the computational complexity of the scheme described in Algorithm 3. The figure shows a significant advantage of incorporating the RFF with respect to the pure Euler scheme of Algorithm 1 a fortiori without incorporating the random feature sampling step in the elapsed execution time. One can see that external feature sampling has a clear advantage over the classical Euler scheme (it is about 200 times faster). Even internal feature sampling is competitive when simulating relatively long paths of the underlying Volterra process, being 2.5 times faster. It is important to mention that in practice the feature sampling is done once and can be stored and reused for multiple tasks.

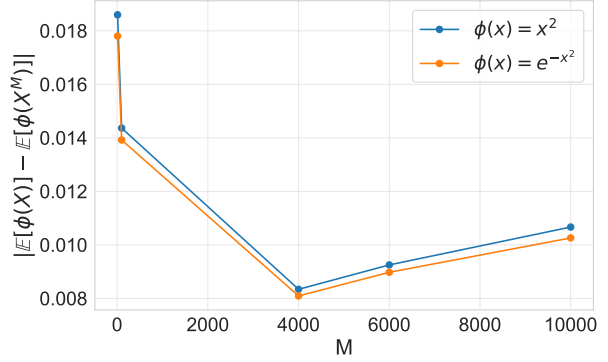
Now, we are interested in the weak error of the RFF-Euler scheme with respect to the classical Euler scheme. In Figure 6, we illustrate a weak error analysis of the proposed simulation scheme by evaluating the convergence of expectations of smooth test functions. More precisely, for a given test function ϕ , we consider the weak error defined by:

$$\mathcal{E}_\phi(M, T_f) = |\mathbb{E}[\phi(X_n^M(T_f))] - \mathbb{E}[\phi(X_n(T_f))]|,$$

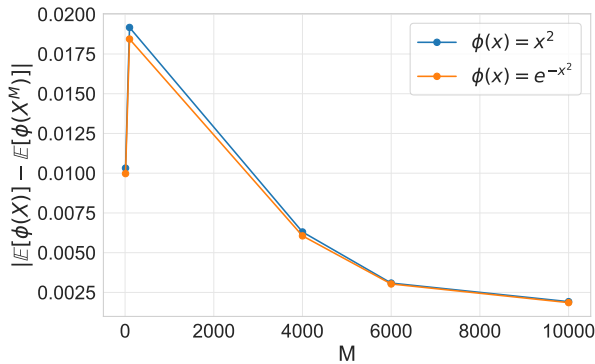
where $X_n^M(T_f)$ denotes the numerical approximation of the process at time T_f using the RFF-Euler scheme and $X_n(T_f)$ is its classical Euler counterpart. The expectations are estimated using Monte Carlo simulations and the weak errors are reported for two representative test functions, $\phi(x) = x^2$ and $\phi(x) = \exp(-x^2)$. The figure compares scenarios in which the numerical and reference solutions are driven either by distinct Brownian paths or by the same Brownian path, for two values of the Hurst exponent H . This setup allows us to assess the sole impact of the RFF kernel approximation on the one hand, and both the impact of Brownian regularization and the RFF approximation on the other hand on the accuracy of weak approximations.



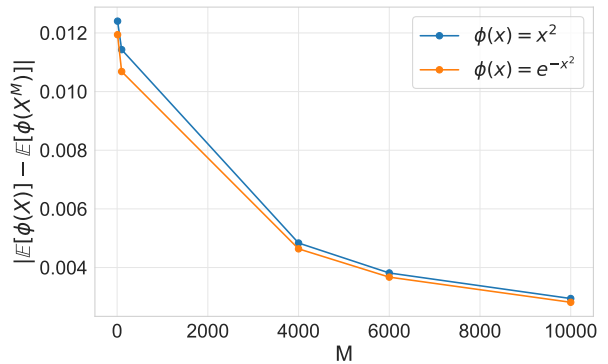
(a) Different Brownian path, $H = 0.05$



(b) Same Brownian path, $H = 0.05$



(c) Different Brownian path, $H = 0.1$



(d) Same Brownian path, $H = 0.1$

Figure 6: Weak error analysis for two test functions $\phi(x) = x^2$ (blue) and $\phi(x) = \exp(-x^2)$ (orange). Results are obtained with $T_f = 1$, $T = 200$, $\nu = 1$ and 100 Brownian simulations. The left column corresponds to simulations driven by independent Brownian motions, while the right column uses a common Brownian path. The top row shows the case $H = 0.05$ and the bottom row corresponds to $H = 0.1$.

The results displayed in Figure 6 indicate a clear and consistent decay of the weak error as the RFF approximation is refined, for both test functions under consideration. Using a common Brownian path systematically reduces the weak error by a factor of about 10. Moreover, the qualitative behaviour of the weak error remains similar as a function of M for both $\phi(x) = x^2$ and $\phi(x) = \exp(-x^2)$, suggesting that the numerical scheme exhibits robust weak convergence.

We now investigate the strong approximation error induced by the use of a finite number M of simulated features in the construction of the numerical scheme. For any fixed final time horizon $T_f > 0$ and any $p \geq 1$, we define the strong error at time T_f as

$$\mathcal{E}_{\text{strong}}^p(M, T_f) := \|X_n^M(T_f) - X_n(T_f)\|_{\mathcal{L}^p}^p, \quad (69)$$

The dependence of the strong error on the number of features is then characterized by the mapping

$$M \mapsto \mathcal{E}_{\text{strong}}^p(M, T_f),$$

which we analyze for arbitrary but fixed time horizon T_f . In order to disentangle the different sources of approximation error, we consider two distinct coupling scenarios. In the first scenario, both processes X_n and X_n^M are driven by the same underlying Brownian path. This synchronous coupling isolates the contribution of the random Fourier features approximation of the S-fBM kernel and allows us to assess its sole impact on the strong error. In the second scenario, the two processes are driven by independent Brownian motions. This

setting captures not only the error induced by the random feature approximation, but also the additional discrepancy arising from the stochastic regularization introduced by the Brownian perturbations themselves. Together, these two regimes provide a comprehensive characterization of the strong convergence behavior of the scheme as a function of M .

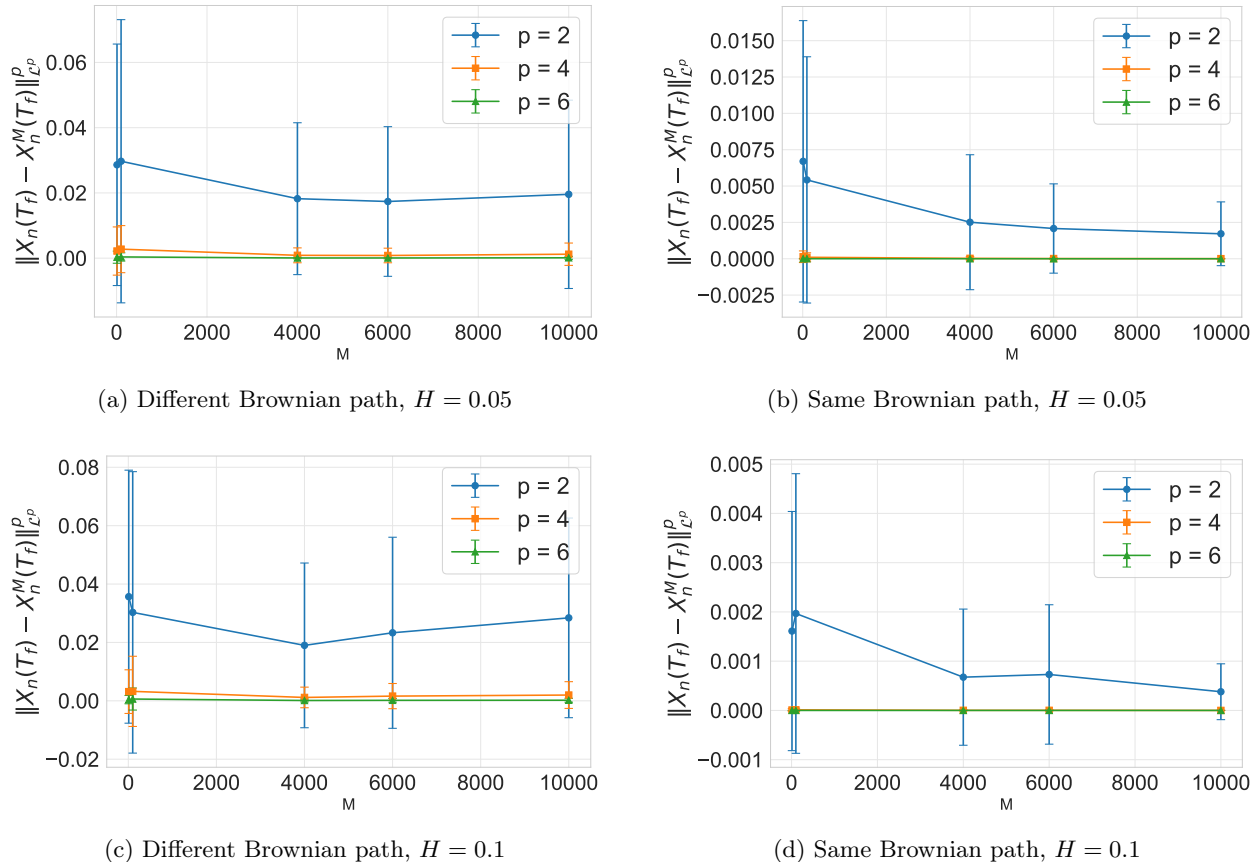


Figure 7: Strong error analysis with the corresponding 95% confidence interval considering $p = 2$, $p = 4$ and $p = 6$. Results are obtained with $T_f = 1$, $T = 200$, $\nu = 1$ and 100 Brownian simulations. The left column corresponds to simulations driven by independent Brownian motions, while the right column uses a common Brownian path. The top row shows the case $H = 0.05$ and the bottom row corresponds to $H = 0.1$.

In Figure 7, the numerical results indicate an improvement in approximation accuracy as the number of simulated features M increases. In particular, the strong approximation error is observed to decay monotonically with respect to M , reflecting the enhanced fidelity of the random feature representation of the underlying kernel. This decay is consistent with the expected averaging effects induced by Monte Carlo-type approximations. In parallel, the associated confidence intervals around the empirical error estimates become narrower as M grows, indicating a reduction in the variance of the error. Together, these effects demonstrate that increasing the number of features improves the average accuracy of the scheme.

8 Conclusion and prospects

In this work, we have developed a comprehensive theoretical and numerical framework of an accelerated numerical scheme for stochastic Volterra processes based on the random Fourier Features approximation, with a particular focus on stochastic Volterra equations involving the stationary fractional Brownian motion (s-fBM) covariance kernel.

Using the theoretical connection between the complete monotonicity and positive definiteness properties, we proved that the proposed RFF approximation is applicable to a larger class of kernels than the classical multifactor approximation by a sum of exponential terms, including kernels with compact support such as the s-fBM kernel.

The RFF-based spectral Monte Carlo technique, implemented using Hamiltonian Monte Carlo (HMC) sampling, substantially speeds up the simulation of stochastic Volterra equations, with controlled accuracy. Rigorous quantitative results, including strong \mathcal{L}^p error bounds (Theorems 1 and 2), establish uniform-in-time control of the schemes and explicit convergence rates in terms of the time discretization truncation parameter N and the number of random features M .

Focusing on the S-fBM kernel, for which we determined explicitly its spectral density and parameter condition for positive definiteness, our numerical experiments confirm that the proposed method reproduces the kernel and its statistical properties with high fidelity. Non-asymptotic error bounds decompose the overall approximation error into contributions from time discretization, spectral truncation, and stochastic sampling, with each component explicitly controlled.

To sum up, the proposed RFF-Euler scheme for Volterra equations allows for efficient approximation of a broad class of memory-driven kernels, while maintaining strong guarantees on accuracy, convergence, and computational tractability. Future work could include practical applications of the scheme for quantitative finance problems, such as option pricing under rough volatility dynamics and stochastic control problems.

Acknowledgements

Othmane Zarhali acknowledges the support from the French government, managed by the National Research Agency (ANR), under the “France 2030” program with reference “ANR-23-IACL-0008”. Nicolas Langrené acknowledges the support of the Guangdong Provincial/Zhuhai Key Laboratory of IRADS (2022B1212010006).

References

- Abi Jaber, E., Bayer, C., and Breneis, S. (2024). State spaces of multifactor approximations of nonnegative Volterra processes. Finance and Stochastics, 28:1–52.
- Abi Jaber, E., Cuchiero, C., Larsson, M., and Pulido, S. (2021). A weak solution theory for stochastic Volterra equations of convolution type. Annals of Applied Probability, 31(6):2924–2962.
- Abi Jaber, E. and El Euch, O. (2019). Multifactor approximation of rough volatility models. SIAM Journal on Financial Mathematics, 10(2):309–349.
- Abi Jaber, E., Larsson, M., and Pulido, S. (2019). Affine Volterra processes. Annals of Applied Probability, 29(5):3155–3200.
- Alfonsi, A. and Kebaier, A. (2024). Approximation of stochastic Volterra equations with kernels of completely monotone type. Stochastic Processes and their Applications, 168:104–139.
- Bacry, E., Delour, J., and Muzy, J.-F. (2001a). Modelling financial time series using multifractal random walks. Physica A: Statistical Mechanics and its Applications, 299(1-2):84–92.
- Bacry, E., Delour, J., and Muzy, J.-F. (2001b). Multifractal random walk. Physical Review E, 64(2):026103.
- Bacry, E. and Muzy, J. F. (2003). Log-infinitely divisible multifractal processes. Communications in Mathematical Physics, 236:449–475.
- Bayer, C. and Breneis, S. (2023). Markovian approximations of stochastic Volterra equations with the fractional kernel. Quantitative Finance, 23(1):53–70.
- Bayer, C., Friz, P., and Gatheral, J. (2016). Pricing under rough volatility. Quantitative Finance, 16(6):887–904.
- Bennedsen, M., Lunde, A., and Pakkanen, M. S. (2017). Hybrid scheme for Brownian semistationary processes. Finance and Stochastics, 21:931–965.
- Biagini, F., Hu, Y., Øksendal, B., and Zhang, T. (2008). Stochastic Calculus for Fractional Brownian Motion and Applications. Springer.
- Cho, Y.-K. and Yun, H. (2018). Newton diagram of positivity for ${}_1F_2$ generalized hypergeometric functions. Integral Transforms and Special Functions, 29(7):527–542.
- Cont, R. (2001). Empirical properties of asset returns: stylized facts and statistical issues. Quantitative Finance, 1(2):223–236.
- Coutin, L. and Qian, Z. (2007). Rough paths and fractional Brownian motion. Probability Surveys, 4:1–41.
- Decreusefond, L. (2002). Regularity properties of some stochastic volterra integrals with singular kernels. Potential Analysis, 16(2):139–149.
- Decreusefond, L. and Üstünel, A. S. (1998). Fractional Brownian motion: theory and applications. ESAIM: Proceedings, 5:75–86.
- Delbridge, I., Bindel, D., and Wilson, A. G. (2020). Randomly projected additive Gaussian processes for regression. In International Conference on Machine Learning, pages 2453–2463.
- Di Nunno, G., Mishura, Y., and Ralchenko, K. (2022). Stochastic differential equations driven by additive Volterra–Lévy and Volterra–Gaussian noises. Stochastic Processes, Statistical Methods, and Engineering Mathematics, 408:247–268.
- DLMF (2025). NIST Digital Library of Mathematical Functions. F. W. J. Olver, A. B. Olde Daalhuis, D. W. Lozier, B. I. Schneider, R. F. Boisvert, C. W. Clark, B. R. Miller, B. V. Saunders, H. S. Cohl, and M. A. McClain, eds.

- Duane, S., Kennedy, A. D., Pendleton, B. J., and Roweth, D. (1987). Hybrid Monte Carlo. Physics Letters B, 195(2):216–222.
- El Euch, O. and Rosenbaum, M. (2019). The characteristic function of rough Heston models. Mathematical Finance, 29(1):3–38.
- Emery, X. and Lantuéjoul, C. (2006). TBSIM: a computer program for conditional simulation of three-dimensional gaussian random fields via the turning bands method. Computers and Geosciences, 32(10):1615–1628.
- Fasshauer, G. (2007). Meshfree Approximation Methods with Matlab, volume 6 of Interdisciplinary Mathematical Sciences. World Scientific Publishing.
- Gatheral, J., Jaisson, T., and Rosenbaum, M. (2018). Volatility is rough. Quantitative Finance, 18(6):933–949.
- Golubov, B. I. (1981). On Abel-Poisson type and Riesz means. Analysis Mathematica, 7(3):161–184.
- Harms, P. and Stefanovits, B. (2019). Strong convergence rates for Volterra processes via Fourier methods. Stochastic Processes and their Applications, 129:4826–4863.
- Langrené, N., Warin, X., and Gruet, P. (2025). A spectral mixture representation of isotropic kernels with application to random Fourier features. arXiv:2411.02770.
- Lázaro-Gredilla, M., Quiñonero-Candela, J., Rasmussen, C. E., and Figueiras-Vidal, A. R. (2010). Sparse spectrum Gaussian process regression. Journal of Machine Learning Research, 11:1865–1881.
- Le, Q., Sarlós, T., and Smola, A. (2013). Fastfood-approximating kernel expansions in loglinear time. In Proceedings of the International Conference on Machine Learning, volume 85.
- Liu, Y., Li, J., Sun, S., and Yu, B. (2019). Advances in Gaussian random field generation: a review. Computational Geosciences, 23(5):1011–1047.
- Mandelbrot, B. B. and Van Ness, J. W. (1968). Fractional Brownian motions, fractional noises and applications. SIAM Review, 10(4):422–437.
- Mishura, Y., Shevchenko, G., and Shklyar, S. (2020). Gaussian processes with Volterra kernels. Modern Stochastics: Theory and Applications, 7(3):219–247.
- Muzy, J.-F. and Bacry, E. (2002). Multifractal stationary random measures and multifractal random walks with log infinitely divisible scaling laws. Physical review E, 66(5):056121.
- Muzy, J.-F., Baïle, R., and Bacry, E. (2013). Random cascade model in the limit of infinite integral scale as the exponential of a nonstationary $1/f$ noise. Application to volatility fluctuations in stock markets. Physical Review E, 87(4):042813.
- Muzy, J.-F., Delour, J., and Bacry, E. (2000). Modelling fluctuations of financial time series: from cascade process to stochastic volatility model. The European Physical Journal B-Condensed Matter and Complex Systems, 17:537–548.
- Pannier, A. and Jacquier, A. (2019). On the uniqueness of solutions of stochastic Volterra equations. arXiv:1912.05917.
- Pinelis, I. (2020). Exact lower and upper bounds on the incomplete gamma function. Mathematical Inequalities and Applications, 23(4):1261–1278.
- Prömel, D. J. et al. (2025). Pathwise uniqueness for singular stochastic Volterra equations. Probability Theory and Related Fields.

- Rahimi, A. and Recht, B. (2007). Random features for large-scale kernel machines. In Advances in Neural Information Processing Systems.
- Richard, A., Tan, X., and Yang, F. (2021). Discrete-time simulation of stochastic Volterra equations. Stochastic Processes and their Applications, 141:109–138.
- Rosenthal, H. P. (1970). On the subspaces of L^p ($p > 2$) spanned by sequences of independent random variables. Israel Journal of Mathematics, 8:273–303.
- Rudi, A. and Rosasco, L. (2017). Generalization properties of learning with random features. In Advances in Neural Information Processing Systems, volume 30, pages 3215–3225.
- Sasvári, Z. (2013). Multivariate Characteristic and Correlation Functions, volume 50 of De Gruyter Studies in Mathematics. De Gruyter.
- Sutherland, D. J. and Schneider, J. (2015). On the error of random Fourier features. In Proceedings of the 32nd International Conference on Machine Learning (ICML), pages 1225–1234. JMLR.org.
- Vedaldi, A. and Zisserman, A. (2012). Efficient additive kernels via explicit feature maps. In IEEE Transactions on Pattern Analysis and Machine Intelligence.
- von Bahr, B. and Esseen, C.-G. (1965). Inequalities for the r -th absolute moment of a sum of random variables, $1 \leq r \leq 2$. Annals of Mathematical Statistics, 36(1):299–303.
- Wu, P., Muzy, J.-F., and Bacry, E. (2022). From rough to multifractal volatility: The log S-fBm model. Physica A: Statistical Mechanics and its Applications, 604:127919.
- Yaglom, A. M. (1987a). Correlation Theory of Stationary and Related Random Functions Volume I: Basic Results. Springer Series in Statistics. Springer.
- Yaglom, A. M. (1987b). Correlation Theory of Stationary and Related Random Functions Volume II: Supplementary Notes and References. Springer Series in Statistics. Springer.
- Zarhali, O., Aubrun, C., Bacry, E., Bouchaud, J.-P., and Muzy, J.-F. (2025). Why is the volatility of single stocks so much rougher than that of the S&P500? arXiv:2505.02678.
- Zarhali, O., Bacry, E., and Muzy, J.-F. (2026). From rough to multifractal multidimensional volatility: A multidimensional Log S-fBM model. arXiv:2601.10517.
- Zastavnyi, V. (2006). On some properties of Buhmann functions. Ukrainian Mathematical Journal, 58(8).
- Zhu, Q., Loeper, G., Chen, W., and Langrené, N. (2021). Markovian approximation of the rough Bergomi model for Monte Carlo option pricing. Mathematics, 9(5):528.

A S-fBM spectral density

A.1 Proof of Proposition 4

Proposition 4. *The Fourier transform of the S-fBM kernel for $d = 1$ can be expressed as follows:*

$$\forall u \in \mathbb{R}, \quad g_\omega(u) = \sqrt{\frac{2}{\pi}} \frac{\lambda^2}{H(1-2H)} \left(\frac{\sin(uT)}{u} - T \sum_{\substack{k \geq 0 \\ k \text{ even}}} \frac{(Tu)^k (-1)^{\lfloor k/2 \rfloor}}{(2H+k+1)k!} \right) \quad (70)$$

Proof. $\omega_{H,T}$ is stationary and its autocovariance function is in $\mathcal{L}^1([-T, T])$. Thus, it admits a spectral density denoted f_ω .

We have:

$$g_\omega(u) = \frac{1}{\sqrt{2\pi}} \int_{\mathbb{R}} C_{\omega_{H,T}}(h) e^{-ihu} dh$$

Using the expression of $C_{\omega_{H,T}}(\cdot)$, we end up with:

$$g_\omega(u) = \frac{\lambda^2}{\sqrt{2\pi}H(1-2H)} \left(2 \frac{\sin(uT)}{u} - \int_{-T}^T \left(\frac{|h|}{T} \right)^{2H} e^{-ihu} dh \right)$$

Furthermore, we have by straightforward computations:

$$\overline{\int_{-T}^T |h|^{2H} e^{-ihu} dh} = - \int_{-T}^T |h|^{2H} e^{-ihu} (-dh) = \int_{-T}^T |h|^{2H} e^{-ihu} dh,$$

which means that the previous function is real-valued. Besides,

$$\int_{-T}^T |h|^{2H} e^{-ihu} dh = 2 \int_0^T h^{2H} \cos(hu) dh = 2\mathcal{R} \left(\int_0^T h^{2H} e^{ihu} dh \right)$$

Using the series expansion, one has:

$$\int_0^T h^{2H} e^{ihu} dh = \sum_{k=0}^{\infty} \frac{(iu)^k}{k!} \int_0^T h^{2H+k} dh = T^{2H+1} \sum_{k=0}^{\infty} \frac{(iT)^k}{(2H+k+1)k!}$$

After some algebra, one has:

$$\int_{-T}^T |h|^{2H} e^{-ihu} dh = 2T^{2H+1} \sum_{k=0}^{\infty} \frac{(Tu)^k \cos\left(\frac{k\pi}{2}\right)}{(2H+k+1)k!}$$

Thus,

$$\int_{-T}^T |h|^{2H} e^{-ihu} dh = 2T^{2H+1} \sum_{\substack{k \geq 0 \\ k \text{ even}}} \frac{(Tu)^k (-1)^{\lfloor k/2 \rfloor}}{(2H+k+1)k!},$$

which gives the claimed result. □

A.2 Proof of Proposition 2

Proof. 1. Since $C_\omega \in L^1(\mathbb{R}^d)$, $\omega_{H,T}$ a Fourier transform

$$g_\omega(\mathbf{x}) = \frac{1}{(2\pi)^{\frac{d}{2}}} \int_{\mathbb{R}^d} C_\omega(\mathbf{h}) e^{-i\langle \mathbf{h}, \mathbf{x} \rangle} d\mathbf{h}, \quad \mathbf{x} \in \mathbb{R}^d.$$

Substituting C_ω yields

$$g_\omega(\mathbf{x}) = \frac{\lambda^2}{(2\pi)^{\frac{d}{2}} H(1-2H)} \left[\int_{\|\mathbf{h}\| \leq T} e^{-i\langle \mathbf{h}, \mathbf{x} \rangle} d\mathbf{h} - \frac{1}{T^{2H}} \int_{\|\mathbf{h}\| \leq T} \|\mathbf{h}\|^{2H} e^{-i\langle \mathbf{h}, \mathbf{x} \rangle} d\mathbf{h} \right].$$

Both integrals are radial. Using the Fourier–Bessel transform formula for radial functions in \mathbb{R}^d , we obtain

$$\begin{aligned} \int_{\|\mathbf{h}\| \leq T} e^{-i\langle \mathbf{h}, \mathbf{x} \rangle} d\mathbf{h} &= (2\pi)^{\frac{d}{2}} T^d \frac{J_{\frac{d}{2}}(T\|\mathbf{x}\|)}{(T\|\mathbf{x}\|)^{\frac{d}{2}}}, \\ \int_{\|\mathbf{h}\| \leq T} \|\mathbf{h}\|^{2H} e^{-i\langle \mathbf{h}, \mathbf{x} \rangle} d\mathbf{h} &= (2\pi)^{\frac{d}{2}} \|\mathbf{x}\|^{1-\frac{d}{2}} \int_0^T r^{2H+\frac{d}{2}} J_{\frac{d}{2}-1}(\|\mathbf{x}\|r) dr. \end{aligned}$$

Thus,

$$g_\omega(\mathbf{x}) = \frac{\lambda^2}{H(1-2H)} \left[T^d \frac{J_{\frac{d}{2}}(T\|\mathbf{x}\|)}{(T\|\mathbf{x}\|)^{\frac{d}{2}}} - \frac{1}{T^{2H}} \|\mathbf{x}\|^{1-\frac{d}{2}} \int_0^T r^{2H+\frac{d}{2}} J_{\frac{d}{2}-1}(\|\mathbf{x}\|r) dr \right].$$

This shows that f_ω is a real-valued, radial function of \mathbf{x} . Integrating term by term gives

$$\int_0^T r^{2H+\frac{d}{2}} J_{\frac{d}{2}-1}(\|\mathbf{x}\|r) dr = \sum_{m=0}^{\infty} \frac{(-1)^m}{m! \Gamma(m + \frac{d}{2})} \left(\frac{\|\mathbf{x}\|}{2} \right)^{2m+\frac{d}{2}-1} \frac{T^{2H+2m+\frac{d}{2}+1}}{2H+2m+\frac{d}{2}+1}.$$

Plugging this into the expression of $f_\omega(\mathbf{x})$ and simplifying yields

$$g_\omega(\mathbf{x}) = \frac{\lambda^2 T^d}{H(1-2H)} \left[\frac{J_{\frac{d}{2}}(T\|\mathbf{x}\|)}{(T\|\mathbf{x}\|)^{\frac{d}{2}}} - T^{1-\frac{d}{2}} \sum_{m=0}^{\infty} \frac{(-1)^m}{m! \Gamma(m + \frac{d}{2})} \frac{(T\|\mathbf{x}\|/2)^{2m}}{2H+d+2m} \right].$$

2. The Bessel function representation is an alternating series. For the sake of compactness, we consider for any given $x > 0$:

$$a_m(x) = \frac{(-1)^m}{m! \Gamma(m + \alpha + 1)} \left(\frac{x}{2} \right)^{2m+\alpha}, \quad m \in \mathbb{N}$$

For a integer order $\alpha > 0$, the Bessel function of the first kind is given by the series

$$J_\alpha(x) = \sum_{m=0}^{\infty} a_m(x).$$

The associated remainder denoted $R_N(x)$ is known as:

$$R_N(x) = \sum_{m=N}^{\infty} \frac{(-1)^m}{m! \Gamma(m + \alpha + 1)} \left(\frac{x}{2} \right)^{2m+\alpha}.$$

Let

$$b_m = |a_m| = \frac{1}{m! \Gamma(m + \alpha + 1)} \left(\frac{x}{2} \right)^{2m+\alpha}, \quad m \in \mathbb{N}$$

Using the identity:

$$\forall x \in \mathbb{R}_+^*, \quad \Gamma(x+1) = x\Gamma(x)$$

leads to claim that $(b_m)_{m \in \mathbb{N}}$ is monotonically decreasing (this means that the radius of convergence is $+\infty$, ensuring absolute convergence in \mathbb{R}_+^*). Thus, the alternating-series remainder satisfies

$$\forall x > 0, \quad |R_N(x)| \leq b_N = \frac{1}{N! \Gamma(N + \alpha + 1)} \left(\frac{x}{2}\right)^{2N + \alpha}. \quad (71)$$

$$\left| J_{\frac{d}{2}}(T\|\mathbf{x}\|) - \widehat{J}_{\frac{d}{2}}^N(T\|\mathbf{x}\|) \right| \leq \frac{1}{N! \Gamma(N + \frac{d}{2} + 1)} \left(\frac{T\|\mathbf{x}\|}{2}\right)^{2N + \frac{d}{2}} \quad (72)$$

Arguing the same way leads for any $\mathbf{x} \in \mathbb{R}^d$ to:

$$\left| \sum_{m=N}^{\infty} \frac{(-1)^m}{m! \Gamma(m + \frac{d}{2})} \frac{(T\|\mathbf{x}\|/2)^{2m}}{2H + d + 2m} \right| \leq \frac{(T\|\mathbf{x}\|/2)^{2N}}{N! \Gamma(N + \frac{d}{2}) (2H + d + 2N)} \quad (73)$$

As a result, for any $\mathbf{x} \in \mathbb{R}^d$:

$$|\hat{g}_\omega^N(\mathbf{x}) - g_\omega(\mathbf{x})| \leq \frac{1}{N! \Gamma(N + \frac{d}{2} + 1)} \left(\frac{T\|\mathbf{x}\|}{2}\right)^{2N + \frac{d}{2}} + \frac{(T\|\mathbf{x}\|/2)^{2N}}{N! \Gamma(N + \frac{d}{2}) (2H + d + 2N)} \quad (74)$$

This means that for any compact $K \subset \mathbb{R}^d$, there exists a positive constant C such that:

$$\|\hat{g}_\omega^N - g_\omega\|_\infty^K \leq \frac{(TC/2)^{2N}}{N! \Gamma(N + \frac{d}{2}) (N + \frac{d}{2})} \left(\left(\frac{TC}{2}\right)^{\frac{d}{2}} + 1 \right) \quad (75)$$

where $C := \sup_{x \in K} \|x\|$.

□

A.3 Proof of Theorem 3

Before demonstrating the error bound, we need this technical lemma:

Lemma 1. For any $n \in \mathbb{N}$,

$$\left(\frac{n}{e}\right)^n e \leq n! \leq \frac{e^2}{4} \left(\frac{n+1}{e}\right)^{n+1}. \quad (76)$$

Proof. We start from the basic inequality

$$\forall x \in \mathbb{R}, \quad x - 1 < [x] \leq x,$$

which immediately implies, for $x > 1$,

$$\log(x-1) \leq \log([x]) \leq \log(x).$$

Integrating over the interval $[2, n+1]$, we obtain

$$\int_2^{n+1} \log(x-1) dx \leq \int_2^{n+1} \log([x]) dx = \sum_{k=2}^n \log k \leq \int_2^{n+1} \log x dx.$$

Evaluating the integrals gives

$$(n-1)\log n - (n-2) \leq \log(n!) \leq n\log(n+1) - (n-1) - (2\log 2 - 2),$$

which can be simplified to

$$n(\log n - 1) + 1 \leq \log(n!) \leq (n+1)(\log(n+1) - 1) - (2\log 2 - 2).$$

Exponentiating both sides yields the bounds

$$e^{n(\log n - 1) + 1} \leq n! \leq e^{(n+1)(\log(n+1) - 1) - (2\log 2 - 2)},$$

or equivalently,

$$\left(\frac{n}{e}\right)^n e \leq n! \leq \frac{e^2}{4} \left(\frac{n+1}{e}\right)^{n+1}.$$

□

We can now proceed with the proof of Theorem 3.

Proof. 1. We reason on the kernel $K_\alpha(\mathbf{u}) = (1 - \|\mathbf{u}\|^\alpha) \mathbb{1}_{\{\|\mathbf{u}\| \leq 1\}}$ as the S-fBM kernel is simply a rescaling of it.

Since the kernel (51) is continuous and absolutely integrable, its Fourier transform is given by (Fasshauer, 2007, Theorem B.1)

$$\mathcal{F}_\alpha(\mathbf{x}) = \frac{1}{(2\pi)^{\frac{d}{2}} \|\mathbf{x}\|^{\frac{d}{2}-1}} \int_0^1 t^{\frac{d}{2}} (1-t^\alpha) J_{\frac{d}{2}-1}(\|\mathbf{x}\| t) dt.$$

Then, use equation (46) to obtain

$$\begin{aligned} \mathcal{F}_\alpha(\mathbf{x}) &= \frac{1}{(2\pi)^{\frac{d}{2}} \|\mathbf{x}\|^{\frac{d}{2}-1}} \int_0^1 t^{\frac{d}{2}} (1-t^\alpha) \sum_{n=0}^{\infty} \frac{(-1)^n (\|\mathbf{x}\| t/2)^{\frac{d}{2}-1+2n}}{n! \Gamma(n + \frac{d}{2})} dt \\ &= \frac{1}{2^{\frac{d}{2}-1} (2\pi)^{\frac{d}{2}}} \sum_{n=0}^{\infty} \frac{(-\|\mathbf{x}\|^2/4)^n}{n! \Gamma(n + \frac{d}{2})} \int_0^1 t^{2n+d-1} (1-t^\alpha) dt. \end{aligned}$$

Then, using a change of variable and the definition of the beta function $B(a, b) = \frac{\Gamma(a)\Gamma(b)}{\Gamma(a+b)} = \int_0^1 t^{a-1} (1-t)^{b-1} du$ with $a = (2n+d)/\alpha$ and $b = 2$,

$$\begin{aligned} \int_0^1 t^{2n+d-1} (1-t^\alpha) dt &= \frac{1}{\alpha} \int_0^1 t^{\frac{2n+d}{\alpha}-1} (1-t) dt = \frac{1}{\alpha} \frac{\Gamma(\frac{2n+d}{\alpha})}{\Gamma(\frac{2n+d}{\alpha} + 2)} \\ &= \frac{1}{\alpha} \frac{1}{(\frac{2n+d}{\alpha} + 1) (\frac{2n+d}{\alpha})} = \frac{\alpha}{4} \frac{1}{(\frac{d+\alpha}{2} + n) (\frac{d}{2} + n)} = \frac{\alpha}{4} \frac{\Gamma(\frac{d+\alpha}{2} + n)}{(\frac{d}{2} + n) \Gamma(\frac{d+\alpha}{2} + 1 + n)}, \end{aligned}$$

which gives

$$\begin{aligned} \mathcal{F}_\alpha(\mathbf{x}) &= \frac{\alpha}{2^{\frac{d}{2}+1} (2\pi)^{\frac{d}{2}}} \sum_{n=0}^{\infty} \frac{(-\|\mathbf{x}\|^2/4)^n}{n! \Gamma(\frac{d}{2} + n)} \frac{\Gamma(\frac{d+\alpha}{2} + n)}{(\frac{d}{2} + n) \Gamma(\frac{d+\alpha}{2} + 1 + n)} \\ &= \frac{\alpha}{2^{\frac{d}{2}+1} (2\pi)^{\frac{d}{2}}} \sum_{n=0}^{\infty} \frac{\Gamma(\frac{d+\alpha}{2} + n)}{\Gamma(\frac{d+\alpha}{2} + 1 + n) \Gamma(\frac{d}{2} + 1 + n)} \frac{(-\|\mathbf{x}\|^2/4)^n}{n!} \\ &= \frac{\alpha}{2^{\frac{d}{2}+1} (2\pi)^{\frac{d}{2}}} \frac{\Gamma(\frac{d+\alpha}{2})}{\Gamma(\frac{d+\alpha}{2} + 1) \Gamma(\frac{d}{2} + 1)} \sum_{n=0}^{\infty} \frac{(\frac{d+\alpha}{2})_n}{(\frac{d+\alpha}{2} + 1)_n (\frac{d}{2} + 1)_n} \frac{(-\|\mathbf{x}\|^2/4)^n}{n!} \\ &= \frac{1}{2^{\frac{d}{2}} (2\pi)^{\frac{d}{2}} (\frac{d}{\alpha} + 1) \Gamma(\frac{d}{2} + 1)} {}_1F_2 \left(\frac{d+\alpha}{2}; \frac{d+\alpha}{2} + 1, \frac{d}{2} + 1; -\frac{\|\mathbf{x}\|^2}{4} \right). \end{aligned}$$

Using a change of variable, we conclude the claimed formula.

2. We recall:

$$f_\omega(\mathbf{x}) = \frac{\nu^2 T^d / 2}{2^d \pi^{\frac{d}{2}} \left(\frac{d}{\alpha} + 1\right) \Gamma\left(\frac{d}{2} + 1\right)} {}_1F_2\left(\frac{d}{2} + H; \frac{d}{2} + H + 1, \frac{d}{2} + 1; -\frac{\|\mathbf{x}\|^2 T^2}{4}\right), \quad \mathbf{x} \in \mathbb{R}^d \quad (77)$$

We fix an arbitrary compact $\mathcal{K} \subset \mathbb{R}^d$.

By definition,

$${}_1F_2\left(\frac{d}{2} + H; \frac{d}{2} + H + 1, \frac{d}{2} + 1; -\frac{\|\mathbf{x}\|^2 T^2}{4}\right) = \sum_{n=0}^{\infty} \frac{\left(\frac{d}{2} + H\right)_n}{\left(\frac{d}{2} + 1\right)_n \left(\frac{d}{2} + H + 1\right)_n} \frac{\left(-\frac{T^2 \|\mathbf{x}\|^2}{4}\right)^n}{n!},$$

We denote for simplicity:

$$t_n(\mathbf{x}) := \frac{\left(\frac{d}{2} + H\right)_n}{\left(\frac{d}{2} + 1\right)_n \left(\frac{d}{2} + H + 1\right)_n} \frac{\left(-\frac{T^2 \|\mathbf{x}\|^2}{4}\right)^n}{n!} \quad (78)$$

After some algebra, the ratio is equal to:

$$\left| \frac{t_{n+1}(\mathbf{x})}{t_n(\mathbf{x})} \right| = \frac{\frac{d}{2} + H + n}{n + 1} \cdot \frac{\frac{T^2 \|\mathbf{x}\|^2}{4}}{\left(\frac{d}{2} + 1 + n\right) \left(\frac{d}{2} + H + 1 + n\right)}. \quad (79)$$

It can be seen that since $\mathbf{x} \in \mathcal{K}$:

$$\forall \mathbf{x} \in \mathcal{K}, \quad \left| \frac{t_{n+1}(\mathbf{x})}{t_n(\mathbf{x})} \right| \leq \frac{Br(\mathcal{K})^2}{n^2} \quad (80)$$

where $r(\mathcal{K}) = \sup_{\mathbf{x} \in \mathcal{K}} \|\mathbf{x}\|$. This means that:

$$\forall \mathbf{x} \in \mathcal{K}, \exists C > 0, \forall n \in \mathbb{N}, \quad t_n(\mathbf{x}) \leq \frac{(Cr(\mathcal{K})^2)^n}{(n!)^2} \quad (81)$$

Using Lemma 1, there exists a positive constant $C > 0$ (depends only on d and H) such that for any $N \in \mathbb{N}$:

$$\forall x \in \mathbb{R}^d, \quad t_n(\mathbf{x}) \leq \frac{1}{e^2} \left(\frac{Cr(\mathcal{K})e}{n} \right)^{2n} \quad (82)$$

the function $t \rightarrow \left(\frac{e}{t}\right)^{2t}$ in $[1, +\infty[$ is decreasing which means (thanks to the Integral Test) that:

$$\begin{aligned} \forall N \in \mathbb{N}^*, \quad \left| \widehat{{}_1F_2}^N\left(\frac{d}{2} + H; \frac{d}{2} + H + 1, \frac{d}{2} + 1; -\frac{\|\mathbf{x}\|^2 T^2}{4}\right) - {}_1F_2\left(\frac{d}{2} + H; \frac{d}{2} + H + 1, \frac{d}{2} + 1; -\frac{\|\mathbf{x}\|^2 T^2}{4}\right) \right| \\ \leq \frac{1}{e^2} \int_{N-1}^{+\infty} \left(\frac{Cr(\mathcal{K})e}{t} \right)^{2t} dt \end{aligned}$$

After some algebra, one has:

$$\begin{aligned} \forall N \in \mathbb{N}^*, \quad \left| \widehat{{}_1F_2}^N\left(\frac{d}{2} + H; \frac{d}{2} + H + 1, \frac{d}{2} + 1; -\frac{\|\mathbf{x}\|^2 T^2}{4}\right) - {}_1F_2\left(\frac{d}{2} + H; \frac{d}{2} + H + 1, \frac{d}{2} + 1; -\frac{\|\mathbf{x}\|^2 T^2}{4}\right) \right| \\ \leq \frac{C}{e(2Cr(\mathcal{K})e(N-1)-1)(N-1)^{2Cr(\mathcal{K})e(N-1)-1}} \end{aligned}$$

Putting all the pieces together leads to:

$$\forall N \in \mathbb{N}^*, \left| \hat{f}_\omega^N(\mathbf{x}) - f_\omega(\mathbf{x}) \right| \leq \frac{\nu^2 T^d / 2}{2^d \pi^{\frac{d}{2}} \left(\frac{d}{\alpha} + 1 \right) \Gamma\left(\frac{d}{2} + 1\right)} \frac{C}{e(2Cr(\mathcal{K})e(N-1)-1)(N-1)^{2Cr(\mathcal{K})e(N-1)-1}}, \quad (83)$$

which yields the claimed result. \square

A.4 Proof of Proposition 3

Proof. We recall:

$$f_\omega(\mathbf{x}) = \frac{\nu^2 T^d / 2}{2^d \pi^{\frac{d}{2}} \left(\frac{d}{\alpha} + 1 \right) \Gamma\left(\frac{d}{2} + 1\right)} {}_1F_2 \left(\frac{d}{2} + H; \frac{d}{2} + H + 1, \frac{d}{2} + 1; -\frac{\|\mathbf{x}\|^2 T^2}{4} \right), \quad \mathbf{x} \in \mathbb{R}^d$$

Let $\hat{f}_\omega^N(\mathbf{x})$ denote the truncated series up to $N - 1$ terms and define the remainder

$$R_N(\mathbf{x}) := f_\omega(\mathbf{x}) - \hat{f}_\omega^N(\mathbf{x}).$$

The remainder $R_{1,N}$ of the hypergeometric series can be expressed as

$${}_1F_2(a; b, c; -z) = \sum_{n=0}^{\infty} \frac{(a)_n}{(b)_n (c)_n} \frac{(-z)^n}{n!} \implies R_{1,N}(z) = \sum_{n=N}^{\infty} \frac{(a)_n}{(b)_n (c)_n} \frac{(-z)^n}{n!}, \quad a = \frac{d}{2} + H, b = \frac{d}{2} + H + 1, c = \frac{d}{2} + 1.$$

Then the total remainder is

$$R_N(\mathbf{x}) = \frac{\nu^2 T^d / 2}{2^d \pi^{\frac{d}{2}} \left(\frac{d}{\alpha} + 1 \right) \Gamma\left(\frac{d}{2} + 1\right)} R_{1,N}(z).$$

For large n , the Pochhammer symbols satisfy

$$(c)_n = c(c+1) \cdots (c+n-1) \geq n! \quad \text{for } c > 0,$$

so that for $n \geq N$ and $z > 0$,

$$\frac{z^n}{(c)_n n!} \leq \frac{z^n}{n!}.$$

A similar argument is valid for ${}_1F_2$,

$$\frac{(a)_n}{(b)_n (c)_n n!} \leq \frac{(C_1)^n}{n!^2},$$

for some constant C_1 depending on a, b, c . Thus,

$$\sum_{n=N}^{\infty} \frac{z^n}{(n!)^2} \leq C_2 e^{C_1 z}, \quad z > r,$$

Let

$$C(T, d, \nu, H) = A \left(\frac{T^2}{2} \right)^{\frac{d}{2}} \frac{\nu^2}{\Gamma\left(\frac{d}{2}\right)} \frac{d+H}{d(d+H)},$$

where A is a positive constant depending on a, b, c . Consequently, for any $\mathbf{x} \in \mathbb{R}^d - B(0, r)$, there exists a positive constant C such that

$$|R_N(\mathbf{x})| \leq C(T, d, \nu, H) e^{-CT\|\mathbf{x}\|}$$

Given $r > 0$, the L^1 norm over $\|\mathbf{x}\| > r$ in d dimensions is

$$\|R_N\|_1^{>r} := \int_{\|\mathbf{x}\|>r} |R_N(\mathbf{x})| d\mathbf{x} = \Omega_d \int_r^\infty |R_N(y)| y^{d-1} dy,$$

with $\Omega_d = \frac{2\pi^{\frac{d}{2}}}{\Gamma(\frac{d}{2})}$. Plugging in the pointwise bound,

$$\|R_N\|_1^{>r} \leq \Omega_d C(T, d, \nu, H) \int_r^\infty y^{d-1} e^{-Ty} dy$$

After some algebra, one gets:

$$\int_r^\infty y^{d-1+2\beta} e^{-Ty} dy = \frac{1}{T^d} \int_{Tr}^\infty u^{d-1} e^{-u} du.$$

Then the integral is the upper incomplete gamma function:

$$\int_r^\infty y^{d-1} e^{-Ty} dy = \frac{1}{T^d} \Gamma(d, Tr).$$

given by:

$$\Gamma(s, x) = \int_x^\infty t^{s-1} e^{-t} dt, \quad s > 0 \quad (84)$$

Thus we obtain the explicit L^1 bound:

$$\|f_\omega - \hat{f}_\omega^N\|_1^{>r} \leq \frac{\Omega_d C(T, d, \nu, H)}{T^d} \Gamma(d, Tr)$$

Thanks to the upper bound of Eq. (1.5) in [Pinelis \(2020\)](#), one has:

$$\|f_\omega - \hat{f}_\omega^N\|_1^{>r} \leq \frac{\Omega_d C(T, d, \nu, H)}{T^d} \frac{(Tr + \kappa(d))^d - Tr^d}{d\kappa(d)} e^{-Tr}$$

which ends the proof. \square

B HMC sampling: theoretical background and proofs

This section is devoted to some ergodicity results of the HMC algorithm. Let the state of the HMC chain be denoted by $(y, p) \in \mathbb{R}^d \times \mathbb{R}^d$, where y represents the position and p the momentum. The Hamiltonian is defined as

$$H(y, p) = U(y) + K(p), \quad U(y) = -\log \pi(y), \quad K(p) = \frac{1}{2} p^\top M^{-1} p.$$

Denote by $\Phi_\epsilon^{\text{LF}}(y, p)$ the discrete Hamiltonian flow obtained after L leapfrog steps of size ϵ :

$$(y', p') = \Phi_\epsilon^{\text{LF}}(y, p).$$

This flow can be decomposed as:

$$\Phi_\epsilon^{\text{LF}} = \varphi_{\epsilon/2}^V \circ \varphi_\epsilon^T \circ \varphi_{\epsilon/2}^V,$$

where φ_s^T denotes the exact flow for the kinetic part (advance y by $sM^{-1}p$ holding p fixed) and φ_s^V denotes the exact flow for the potential part (advance p by $-s\nabla U(y)$ holding y fixed). The Metropolis-Hastings acceptance probability is

$$\alpha((y, p), (y', p')) = \min \left\{ 1, \exp(-H(y', p') + H(y, p)) \right\}.$$

The transition kernel $P((y, p), d(y', p'))$ of one HMC iteration is given by

$$P((y, p), d(y', p')) = \alpha((y, p), (y', p')) \delta_{\Phi_\epsilon^{\text{LF}}(y, p)}(d(y', p')) + (1 - \alpha((y, p), (y', p'))) \delta_{(y, -p)}(d(y', p')),$$

where δ_z denotes the Dirac measure at point z . This kernel describes the probability of moving from the current state (y, p) to a new state (y', p') : with probability $\alpha((y, p), (y', p'))$, the proposal $\Phi_\epsilon^{\text{LF}}(y, p)$ is accepted; and with probability $1 - \alpha((y, p), (y', p'))$, the proposal is rejected and the momentum is flipped for

reversibility. In the continuous-time limit (exact Hamiltonian flow denoted $\Phi^{\text{LF}}(\cdot, \cdot)$), the transition kernel is expressed as:

$$\mathbb{P}((y, p), A) = \mathbf{1}_A(\Phi^{\text{LF}}(y, p)),$$

The jump rate is given by:

$$Q((y, p), d(y', p')) = \alpha(y, p) \delta_{\Phi^{\text{LF}}(y, p)}(d(y', p')),$$

We denote:

$$r(y, p) = \int Q((y, p), d(y', p')) = \alpha(y, p),$$

with:

$$\alpha(y, p) = \min(1, \exp(-H(\Phi^{\text{LF}}(y, p)) + H(y, p))).$$

Proposition 5. *The infinitesimal generator reads:*

$$\mathcal{L}f(y, p) = \{f, H\} + \int_{\mathbb{R}^d} [f(y, p') - f(y, p)] Q((y, p), dp'),$$

where $\{f, H\} = \nabla_y f \cdot \nabla_p H - \nabla_p f \cdot \nabla_y H$ is the Poisson bracket and $Q((y, p), dp')$ describes the momentum refreshment kernel.

Proof. Let $f \in C^1(\mathbb{R}^{2d})$. Assume the Hamiltonian flow $(y, p) \mapsto \Phi^{\text{LF}}(y, p)$ is C^1 . Assume the jump kernel $Q((y, p), \cdot)$ has finite total rate

$$r(y, p) := \int_{\mathbb{R}^d} Q((y, p), dp') < \infty.$$

The semigroup is defined by

$$P_t f(y, p) := \mathbb{E}[f(Y_t, P_t) \mid (Y_0, P_0) = (y, p)].$$

Let N_t be the number of jumps in $[0, t]$. Then, one has by conditioning:

$$P_t f(y, p) = \mathbb{E}[f(Y_t, P_t) \mathbf{1}_{\{N_t=0\}}] + \mathbb{E}[f(Y_t, P_t) \mathbf{1}_{\{N_t=1\}}] + \mathbb{E}[f(Y_t, P_t) \mathbf{1}_{\{N_t \geq 2\}}].$$

As N is an inhomogeneous Poisson process with rate:

$$r_s := r(\phi_s(y, p)) = \int_{\mathbb{R}^d} Q(\phi_s(y, p), dp').$$

One has for small $t > 0$:

$$\begin{cases} \mathbb{P}(N_t = 0) &= 1 - r(y, p)t + o(t), \\ \mathbb{P}(N_t = 1) &= r(y, p)t + o(t), \\ \mathbb{P}(N_t \geq 2) &= o(t). \end{cases}$$

Thus:

- If $N_t = 0$, the process follows the Hamiltonian flow:

$$\mathbb{E}[f(Y_t, P_t) \mid N_t = 0] = f(\Phi^{\text{LF}}(y, p)).$$

- If $N_t = 1$, the momentum jumps once to p' distributed according to $Q((y, p), dp')/r(y, p)$ and the position y remains essentially unchanged:

$$\mathbb{E}[f(Y_t, P_t) \mid N_t = 1] = \int_{\mathbb{R}^d} f(y, p') \frac{Q((y, p), dp')}{r(y, p)}.$$

Consequently,

$$\begin{aligned} P_t f(y, p) &= \mathbb{P}(N_t = 0) f(\Phi^{\text{LF}}(y, p)) + \mathbb{P}(N_t = 1) \mathbb{E}[f(Y_t, P_t) \mid N_t = 1] + o(t) \\ &= (1 - r(y, p)t + o(t)) f(\Phi^{\text{LF}}(y, p)) + t \int_{\mathbb{R}^d} f(y, p') Q((y, p), dp') + o(t). \end{aligned}$$

A Taylor expansion along the Hamiltonian flow yields:

$$f(\Phi^{\text{LF}}(y, p)) = f(y, p) + t \left. \frac{d}{dt} f(\Phi^{\text{LF}}(y, p)) \right|_{t=0} + o(t) = f(y, p) + t\{f, H\}(y, p) + o(t),$$

where $\{f, H\} = \nabla_y f \cdot \nabla_p H - \nabla_p f \cdot \nabla_y H$ is the Poisson bracket. As a result,

$$\begin{aligned} P_t f(y, p) - f(y, p) &= t\{f, H\}(y, p) - tr(y, p)f(y, p) + t \int_{\mathbb{R}^d} f(y, p') Q((y, p), dp') + o(t) \\ &= t\{f, H\}(y, p) + t \int_{\mathbb{R}^d} [f(y, p') - f(y, p)] Q((y, p), dp') + o(t). \end{aligned}$$

This leads to:

$$\mathcal{L}f(y, p) = \{f, H\}(y, p) + \int_{\mathbb{R}^d} [f(y, p') - f(y, p)] Q((y, p), dp').$$

□

Proposition 6. *There exists a Lyapunov function for \mathcal{L} , i.e.:*

$$\exists(\alpha, \beta) \in [0, 1] \times \mathbb{R}, \quad \mathcal{L}V(y, p) \leq -\alpha V(y, p) + \beta \quad (85)$$

Proof. Consider the Markov process with generator

$$\mathcal{L}f(y, p) = \{f, H\}(y, p) + \int_{\mathbb{R}^d} [f(y', p') - f(y, p)] Q((y, p), d(y', p')),$$

where

$$Q((y, p), d(y', p')) = \alpha(y, p) \delta_{\Phi^{\text{LF}}(y, p)}(d(y', p')), \quad \alpha(y, p) = \min(1, \exp(-H(\Phi^{\text{LF}}(y, p)) + H(y, p))).$$

Let the Lyapunov function be

$$V(y, p) = 1 + H(y, p).$$

Since V depends only on H , the Poisson bracket term vanishes:

$$\{V, H\} = 0.$$

Thus, the generator applied to V reduces to

$$\begin{aligned} \mathcal{L}V(y, p) &= \int_{\mathbb{R}^d} [V(y', p') - V(y, p)] Q((y, p), d(y', p')) \\ &= \alpha(y, p) [V(\Phi^{\text{LF}}(y, p)) - V(y, p)] \\ &= \alpha(y, p) [H(\Phi^{\text{LF}}(y, p)) - H(y, p)]. \end{aligned}$$

Define the energy difference

$$\Delta H(y, p) = H(\Phi^{\text{LF}}(y, p)) - H(y, p).$$

Then

$$\mathcal{L}V(y, p) = \alpha(y, p) \Delta H(y, p), \quad \alpha(y, p) = \min(1, e^{-\Delta H(y, p)}).$$

Then

$$\mathcal{L}V(y, p) = \alpha(y, p) [(\Delta H(y, p))_+ - (\Delta H(y, p))_-] = \alpha(y, p) \Delta H(y, p)$$

Observing that $-(\Delta H)_- \leq 0$ and $\alpha(y, p)(\Delta H)_+ \leq \sup \alpha(y, p)(\Delta H)_+ =: \beta$, we obtain the drift inequality

$$\mathcal{L}V(y, p) \leq -\alpha V(y, p) + \beta,$$

with

$$\begin{aligned} \alpha &= \inf_{(y, p)} \frac{(\Delta H)_-}{V(y, p)} = \inf_{(y, p)} \frac{\max(0, H(y, p) - H(\Phi^{\text{LF}}(y, p)))}{1 + H(y, p)}, \\ \beta &= \sup_{(y, p)} \alpha(y, p)(\Delta H)_+ = \sup_{(y, p)} \alpha(y, p) \max(0, H(\Phi^{\text{LF}}(y, p)) - H(y, p)). \end{aligned}$$

One can easily notice that $\alpha \in [0, 1]$.

Hence, $V(y, p) = 1 + H(y, p)$ is a Lyapunov function for the generator \mathcal{L} , with drift constants α and β as above. \square

Lemma 2. *For any function $h : \mathcal{X} \rightarrow [a, b]$ where $\mathcal{X} \subset \mathbb{R}^d$ and reals $a \leq b$, there exist a positive constant $C > 0$ and $\rho \in [0, 1]$ such that:*

$$\forall k \geq 0, \quad |\text{Cov}(h(Y_0), h(Y_k))| \leq (b - a)^2 C \rho^k \quad (86)$$

Proof. According to the previous results, Y is geometrically ergodic. The Meyn–Tweedie inequality leads to the existence for any $y \in \mathbb{R}^n$ of $R(y) < \infty$ and $\rho \in [0, 1]$ such that

$$\forall t \geq 0, \quad \|P_t(y, \cdot) - \pi\|_{TV} \leq R(y) \rho^t.$$

Besides, as $(Y_t)_{t \geq 0}$ is a stationary Markov process and homogeneous with transition kernel P and invariant distribution π .

Fix $k \geq 0$. By stationarity

$$\mathbb{E}[h(Y_k)] = \mathbb{E}[h(Y_0)] = \pi(h) := \int_{\mathbb{R}^d} h(y) \pi(dy)$$

so

$$\text{Cov}(h(Y_0), h(Y_k)) = \mathbb{E}[h(Y_0)h(Y_k)] - \pi(h)^2 = \mathbb{E}[h(Y_0) P^k h(Y_0)] - \pi(h)^2,$$

where $P^k h(y) = \int h(y') P^k(y, dy') = \mathbb{E}[h(Y_k) | Y_0 = y]$. Introduce $\pi(h)$ inside the expectation to obtain

$$\text{Cov}(h(Y_0), h(Y_k)) = \mathbb{E}[h(Y_0) (P^k h(Y_0) - \pi(h))].$$

Taking absolute values and using $|h| \leq b - a$ (after centering if desired) gives

$$|\text{Cov}(h(Y_0), h(Y_k))| \leq (b - a) \mathbb{E}[|P^k h(Y_0) - \pi(h)|].$$

For any $y \in \mathcal{X}$,

$$|P^k h(y) - \pi(h)| = \left| \int h(y') (P^k(y, dy') - \pi(dy')) \right| \leq (b - a) \|P^k(y, \cdot) - \pi\|_{TV}.$$

Taking expectation over Y_0 and the supremum over y yields

$$\mathbb{E}[|P^k h(Y_0) - \pi(h)|] \leq (b - a) \sup_y \|P^k(y, \cdot) - \pi\|_{TV}.$$

Combining the last two displays we obtain the first bound

$$|\text{Cov}(h(Y_0), h(Y_k))| \leq (b - a)^2 \sup_y \|P^k(y, \cdot) - \pi\|_{TV}.$$

If, in addition, the chain is geometrically ergodic in total variation, then the previous inequality implies

$$|\text{Cov}(h(Y_0), h(Y_k))| \leq (b - a)^2 C \rho^k,$$

as claimed. \square

C Error of the RFF scheme

C.1 Supporting results

Lemma 3 (BDG-type inequality, [Pannier and Jacquier 2019](#)). *Let $p > 2$ and $\mathbb{T} \subset \mathbb{R}_+$. Let $K : \mathbb{T}^2 \rightarrow \mathbb{R}$ be a kernel and let u be progressively measurable such that the process $M^K(u)$ defined as:*

$$M_t^K(u) := \int_0^t K(t, s)u(s) dW_s.$$

is in L^1 . Then,

$$\mathbb{E} \left[\sup_{t \in \mathbb{T}} |M_t^K(u)|^p \right] \lesssim_p \mathbb{E} \left[\left(\int_0^t |K(t, s)u(s)|^2 ds \right)^{p/2} \right], \quad (87)$$

If moreover $K(t, \cdot) \in L^{p-2}([0, t])$ for all $t \in \mathbb{T}$, then

$$\mathbb{E} \left[\left(\int_0^t |K(t, s)u(s)|^2 ds \right)^{p/2} \right] \leq C_{T,p} \mathbb{E} \left[\int_0^t |u(s)|^p ds \right], \quad (88)$$

where

$$C_{T,p} := \sup_{t \in \mathbb{T}} \|K(t, \cdot)\|_{L^{p-2}([0,t])}^{p/2} < \infty.$$

Proposition 7 ([von Bahr and Esseen \(1965\)](#) inequality). *Let $1 \leq r \leq 2$ and let $(X_i)_{i \geq 1}$ be independent random variables with $\mathbb{E}[X_i] = 0$ and $\mathbb{E}|X_i|^r < \infty$. Then*

$$\mathbb{E} \left| \sum_{i=1}^n X_i \right|^r \leq C_r \sum_{i=1}^n \mathbb{E}|X_i|^r, \quad (89)$$

where the constant $C_r > 0$ depends only on r .

Proposition 8 ([Rosenthal \(1970\)](#) inequality). *Let $p \geq 2$ and let $(X_i)_{i=1}^n$ be independent, mean-zero random variables with $\mathbb{E}|X_i|^p < \infty$. Then there exists a constant $C_p > 0$, depending only on p , such that*

$$\mathbb{E} \left| \sum_{i=1}^n X_i \right|^p \leq C_p \left(\sum_{i=1}^n \mathbb{E}|X_i|^p + \left(\sum_{i=1}^n \mathbb{E}|X_i|^2 \right)^{p/2} \right). \quad (90)$$

C.2 Proof of Theorem 1

1. Let us reason on X_n as the proof is similar. It follows from Hölder's inequality that for any $t \in \mathcal{K}$:

$$\mathbb{E}[|X_n(t)|^p] \leq \mathbb{E}[|X_0|^p] + \mathbb{E} \left[\left| \int_0^t K(t - \zeta_n(s)) \sigma(\zeta_n(s), X_n(\zeta_n(s))) dW_s \right|^p \right].$$

The Burkholder–Davis–Gundy inequality (Lemma 3) together with Theorem 2.3 in [Pannier and Jacquier \(2019\)](#) yield that there exists a positive constant $C > 0$ such that

$$\mathbb{E}[|X_n(t)|^p] \leq C \mathbb{E}[|X_0|^p] + C \mathbb{E} \left[\left(\int_0^t |K(t - \zeta_n(s)) \sigma(\zeta_n(s), X_n(\zeta_n(s)))|^2 ds \right)^{\frac{p}{2}} \right].$$

Applying Hölder's inequality for any $\beta > 0$,

$$\begin{aligned} & \left(\int_0^t |K(t - \zeta_n(s)) \sigma(\zeta_n(s), X_n(\zeta_n(s)))|^2 ds \right)^{\frac{p}{2}} \\ & \leq \left(\int_0^t |K(t - \zeta_n(s))|^{2\beta} ds \right)^{\frac{p}{2\beta}} \left(\int_0^t |\sigma(\zeta_n(s), X_n(\zeta_n(s)))|^{\frac{2\beta}{\beta-1}} ds \right)^{\frac{p(\beta-1)}{2\beta}}. \end{aligned}$$

By the linear growth condition on σ , there exists an arbitrary constant $C > 0$ such that:

$$\begin{aligned} & \left(\int_0^t |K(t - \zeta_n(s)) \sigma(\zeta_n(s), X_n(\zeta_n(s)))|^2 ds \right)^{\frac{p}{2}} \\ & \leq C \left(\int_0^t |K(t - \zeta_n(s))|^{2\beta} ds \right)^{\frac{p}{2\beta}} \left(\int_0^t (1 + |X_n(\zeta_n(s))|^{\frac{2\beta}{\beta-1}}) ds \right)^{\frac{p(\beta-1)}{2\beta}}, \end{aligned}$$

In particular,

$$\begin{aligned} & \left(\int_0^t |K(t - \zeta_n(s)) \sigma(\zeta_n(s), X_n(\zeta_n(s)))|^2 ds \right)^{\frac{p}{2}} \\ & \leq C \left(\int_0^t |K(t - \zeta_n(s))|^{2\beta} ds \right)^{\frac{p}{2\beta}} \left(\int_0^t (1 + |X_n(\zeta_n(s))|^{\frac{2\beta}{\beta-1}}) ds \right)^{\frac{p(\beta-1)}{2\beta}}, \end{aligned}$$

Again, using Hölder's inequality,

$$\begin{cases} \left(\int_0^t (1 + |X_n(\zeta_n(s))|^{\frac{2\beta}{\beta-1}}) ds \right)^{\frac{p(\beta-1)}{2\beta}} \leq t^{\frac{p(\beta-1)}{2\beta}-1} \int_0^t (1 + |X_n(\zeta_n(s))|^p) ds. \\ \left(\int_0^t |K(t - \zeta_n(s))|^{2\beta} ds \right)^{\frac{p}{2\beta}} \leq t^{\frac{p}{2\beta}-1} \int_0^t |K(t - \zeta_n(s))|^p ds. \end{cases}$$

meaning that:

$$\mathbb{E} \left[\left(\int_0^t |K(t - \zeta_n(s)) \sigma(\zeta_n(s), X_n(\zeta_n(s)))|^2 ds \right)^{\frac{p}{2}} \right] \leq C t^{\frac{p}{2}-1} \mathbb{E} \left[\left(\int_0^t |K(t - \zeta_n(s))|^p ds \right) \int_0^t (1 + |X_n(\zeta_n(s))|^p) ds \right]$$

This leads to the existence of a positive constant $C > 0$ such that

$$\mathbb{E}[|X_n(t)|^p] \leq C \left(\mathbb{E}[|X_0|^p] + t^{\frac{p}{2}} K(0)^p \right) + \int_0^t \mathbb{E} \left[|X_n(\zeta_n(s))|^p \right] ds.$$

Applying Grönwall's lemma yields

$$\mathbb{E}[|X_n(t)|^p] \leq C \left(\mathbb{E}[|X_0|^p] + t^{\frac{p}{2}} K(0)^p \right) e^{Ct}.$$

which leads to the claimed result.

2. For any arbitrary $0 \leq s \leq t$, we write

$$\begin{aligned} X_n^M(t) - X_n^M(s) &= \int_s^t \hat{K}_M(t - \zeta_n(u)) \sigma(\zeta_n(u), X_n^M(\zeta_n(u))) dW_u \\ &\quad + \int_0^s \left[\hat{K}_M(t - \zeta_n(u)) - \hat{K}_M(s - \zeta_n(u)) \right] \sigma(\zeta_n(u), X_n^M(\zeta_n(u))) dW_u \\ &=: I_1 + I_2. \end{aligned}$$

For $p > 0$, according to the Burkholder–Davis–Gundy inequality (Lemma 3) together with Theorem 2.3 in [Pannier and Jacquier \(2019\)](#), there exists $C_p > 0$ such that

$$\begin{cases} \mathbb{E}[|I_1|^p] \leq C_p \mathbb{E} \left[\left(\int_s^t |\hat{K}_M(t - \zeta_n(u))|^2 |\sigma(\zeta_n(u), X_n^M(\zeta_n(u)))|^2 du \right)^{p/2} \right], \\ \mathbb{E}[|I_2|^p] \leq C_p \mathbb{E} \left[\left(\int_0^s |\hat{K}_M(t - \zeta_n(u)) - \hat{K}_M(s - \zeta_n(u))|^2 |\sigma(\zeta_n(u), X_n^M(\zeta_n(u)))|^2 du \right)^{p/2} \right]. \end{cases}$$

Thanks to the linear growth assumption, there exists, after some algebra, a positive constant $C_p^1 > 0$ such that:

$$\mathbb{E}[|I_1|^p] \leq C_p^1 |t - s|^{p/2}.$$

Besides, by direct computations, one has for any $s \leq t$:

$$\left| \hat{K}_M(t - \zeta_n(u)) - \hat{K}_M(s - \zeta_n(u)) \right| = 2\mathbb{E} \left[\left| \sin \left(\eta \left(\frac{t+s}{2} - \zeta_n(u) - s \right) \right) \sin \left(\eta \left(\frac{t-s}{2} \right) \right) \right| \right] \leq 2$$

and similarly using the linear growth assumption, there exists a positive constant $C_p^2 > 0$ such that:

$$\mathbb{E}[|I_2|^p] \leq C_p^2.$$

On the other hand, using Minkowski's inequality:

$$\mathbb{E}[|X_n^M(t) - X_n^M(s)|^p] \leq C_p (|t - s|^{p/2} + 1)$$

where $C_p = C_p^1 \vee C_p^2$.

which ends the proof. ■

C.3 Proof of Theorem 2

For simplicity assume $X_0^M = X_0$ (the deterministic initial difference is handled similarly).

By some algebra, the following decomposition holds:

$$\begin{aligned} X_N(t) - X_N^M(t) &= \int_0^t K(t - \zeta_N(s)) \left(\sigma(\zeta_N(s), X_N(\zeta_N(s))) - \sigma(\zeta_N(s), X_N^M(\zeta_N(s))) \right) dW_s \\ &\quad + \int_0^t (K(t - \zeta_N(s)) - \hat{K}_M(t - \zeta_N(s))) \sigma(\zeta_N(s), X_N^M(\zeta_N(s))) dW_s \\ &=: I_t^{(1)} + I_t^{(2)}. \end{aligned}$$

Let $p \geq 2$. By the Burkholder–Davis–Gundy inequality (Lemma 3) together with Theorem 2.3 in [Pannier and Jacquier \(2019\)](#), there exists $C > 0$ such that

$$\mathbb{E}[|X_N(t) - X_N^M(t)|^p] \leq C \mathbb{E}[\langle I^{(1)} \rangle_t^{p/2}] + C \mathbb{E}[\langle I^{(2)} \rangle_t^{p/2}].$$

Using the Lipschitz property of σ in space, we have:

$$\mathbb{E}[\langle I^{(1)} \rangle_t^{p/2}] \leq L \mathbb{E} \left[\left(\int_0^t |K(t - \zeta_N(s))|^2 |X_N(\zeta_N(s)) - X_N^M(\zeta_N(s))|^2 ds \right)^{\frac{p}{2}} \right].$$

Apply Hölder's inequality in time for any exponent arbitrary $\beta > 1$ gives:

$$\begin{aligned} \mathbb{E} \left[\left(\int_0^t |K(t - \zeta_N(s))|^2 |X_N(\zeta_N(s)) - X_N^M(\zeta_N(s))|^2 ds \right)^{\frac{p}{2}} \right] &\leq \left(\int_0^t |K(t - \zeta_N(s))|^{2\beta} ds \right)^{\frac{p}{2\beta}} \\ &\quad \mathbb{E} \left[\left(\int_0^t |X_N(\zeta_N(s)) - X_N^M(\zeta_N(s))|^{\frac{2\beta}{\beta-1}} ds \right)^{\frac{p(\beta-1)}{2\beta}} \right]. \end{aligned}$$

As the random Fourier features representation of K is bounded:

$$\mathbb{E}[\langle I^{(1)} \rangle_t^{p/2}] \leq \int_0^t \mathbb{E}[|X_N(\zeta_N(s)) - X_N^M(\zeta_N(s))|^p] ds,$$

hence

$$\mathbb{E}[|I_t^{(1)}|^p] \leq C \int_0^t \mathbb{E}[|X_N(\zeta_N(s)) - X_N^M(\zeta_N(s))|^p] ds.$$

in particular:

$$\mathbb{E}[|I_t^{(1)}|^p] \leq C \int_0^t \sup_{0 \leq u \leq s} \mathbb{E}[|X_N(u) - X_N^M(u)|^p] ds.$$

On the other hand, we estimate the quadratic variation:

$$\mathbb{E}[\langle I^{(2)} \rangle_t^{p/2}] = \mathbb{E} \left[\left(\int_0^t |K(t - \zeta_N(s)) - \widehat{K}_M(t - \zeta_N(s))|^2 |\sigma(\zeta_N(s), X_N^M(\zeta_N(s)))|^2 ds \right)^{\frac{p}{2}} \right].$$

Applying Hölder's inequality with exponent $\beta > 1$ gives:

$$\mathbb{E}[\langle I^{(2)} \rangle_t^{p/2}] \leq \mathbb{E} \left[\left(\int_0^t |K - \widehat{K}_M|^{2\beta} (t - \zeta_N(s)) ds \right)^{\frac{p}{2\beta}} \left(\int_0^t |\sigma(\zeta_N(s), X_N^M(\zeta_N(s)))|^{\frac{2\beta}{\beta-1}} ds \right)^{\frac{p(\beta-1)}{2\beta}} \right].$$

Using the linear growth property together with the time-averaging inequality (i.e., for any continuous function a and $t \geq 0$, $(\int_0^t a(x) dx)^r \leq t^{r-1} \int_0^t a(x)^r dx$ with $r = \frac{p(\beta-1)}{2\beta} \geq 1$ there exists a positive constant $C_t > 0$ so that:

$$\left(\int_0^t |\sigma(\zeta_N(s), X_N^M(\zeta_N(s)))|^{\frac{2\beta}{\beta-1}} ds \right)^{\frac{p(\beta-1)}{2\beta}} \leq C_t \int_0^t (1 + |X_N^M(\zeta_N(s))|^p) ds.$$

Thus as the random features are independent from the driving Brownian motion W , one has:

$$\mathbb{E}[\langle I^{(2)} \rangle_t^{p/2}] \leq C_t \mathbb{E} \left[\left(\int_0^t |K - \widehat{K}_M|^{2\beta} (t - \zeta_N(s)) ds \right)^{\frac{p}{2\beta}} \right] \int_0^t \mathbb{E}[1 + |X_N^M(\zeta_N(s))|^p] ds.$$

Again apply the time-averaging trick to the first factor to get the convenient bound:

$$\left(\int_0^t |K - \widehat{K}_M|^{2\beta} (t - \zeta_N(s)) ds \right)^{\frac{p}{2\beta}} \leq C_t \int_0^t |K(t - \zeta_N(s)) - \widehat{K}_M(t - \zeta_N(s))|^p ds.$$

Consequently

$$\mathbb{E}[|I_t^{(2)}|^p] \leq C_t \mathbb{E} \left(\int_0^t |K(t - \zeta_N(s)) - \widehat{K}_M(t - \zeta_N(s))|^p ds \right) \left(1 + \sup_{u \in [0, t]} \mathbb{E}[|X_N^M(u)|^p] \right).$$

Using the moment estimate, there exists a positive constant $C(\mathcal{K}) > 0$ for any arbitrary compact $\mathcal{K} \subset \mathbb{R}_+$ such that:

$$\mathbb{E}[|I_t^{(2)}|^p] \leq C(\mathcal{K}) \left(\mathbb{E}[|X_0^M|^p] + |K(0)|^p \right) \mathbb{E} \left(\int_0^t |K(t - \zeta_N(s)) - \widehat{K}_M(t - \zeta_N(s))|^p ds \right).$$

Using Fubini's theorem,

$$\mathbb{E}[|I_t^{(2)}|^p] \leq C(\mathcal{K}) \left(\mathbb{E}[|X_0^M|^p] + |K(0)|^p \right) \int_0^t \mathbb{E} \left(|K(t - \zeta_N(s)) - \widehat{K}_M(t - \zeta_N(s))|^p \right) ds.$$

► For $1 \leq p < 2$, the *Von Bahr-Essen inequality* (Proposition 7) gives for any $0 \leq s \leq t$, after some algebra:

$$\mathbb{E} \left(|K(t - \zeta_N(s)) - \widehat{K}_M(t - \zeta_N(s))|^p \right) \leq C_p M^{-(p-1)}.$$

where C_p is a positive constant. Consequently:

$$\sup_{s \in [0, t]} \mathbb{E}[|X_N(s) - X_N^M(s)|^p] \leq C_{\mathcal{K}}^p \left(\int_0^t \sup_{0 \leq u \leq s} \mathbb{E}[|X_N(u) - X_N^M(u)|^p] ds + \frac{1}{M^{p-1}} \right).$$

where $C_{\mathcal{K}}^p = 4C_p C(\mathcal{K}) \left(\mathbb{E}[|X_0^M|^p] + |K(0)|^p \right) \vee C_t$. Hence, we obtain thanks to Grönwall's lemma:

$$\sup_{s \in [0, t]} \mathbb{E}[|X_N(s) - X_N^M(s)|^p] \leq \frac{C_{\mathcal{K}}^p}{M^{p-1}} e^{C_{\mathcal{K}}^p t}.$$

- For $p \geq 2$, *Rosenthal's inequality* (Proposition 8) states that there exists a constant C_p such that for any $0 \leq s \leq t$:

$$\mathbb{E} \left(\left| \sum_{m=1}^M K(t - \zeta_N(s)) - \cos(\eta_m(t - \zeta_N(s))) \right|^p \right) \leq C_p K(0) \left(\sum_{m=1}^M \mathbb{E}[|K(t - \zeta_N(s)) - \cos(\eta_m(t - \zeta_N(s)))|^p] + \left(\sum_{m=1}^M \mathbb{E}[|K(t - \zeta_N(s)) - \cos(\eta_m(t - \zeta_N(s)))|^2] \right)^{p/2} \right).$$

thanks to the random Fourier features representation, one can have the upper bound after some algebra:

$$\mathbb{E} \left(\left| \sum_{m=1}^M K(t - \zeta_N(s)) - \cos(\eta_m(t - \zeta_N(s))) \right|^p \right) \leq C_p \left(2M + (4M)^{p/2} \right).$$

Consequently,

$$\mathbb{E} \left(|K(t - \zeta_N(s)) - \widehat{K}_M(t - \zeta_N(s))|^p \right) \leq C_p \left(\frac{2}{M^{p-1}} + \left(\frac{4^p}{M} \right)^{\frac{1}{2}} \right).$$

This leads to:

$$\sup_{s \in [0, t]} \mathbb{E}[|X_N(s) - X_N^M(s)|^p] \leq C_{\mathcal{K}}^p \left(\int_0^t \sup_{0 \leq u \leq s} \mathbb{E}[|X_N(u) - X_N^M(u)|^p] ds + \left(\frac{2}{M^{p-1}} + \left(\frac{4^p}{M} \right)^{\frac{1}{2}} \right) \right).$$

where $C_{\mathcal{K}}^p = C(\mathcal{K}) \left(\mathbb{E}[|X_0^M|^p] + |K(0)|^p \right) \vee C_p$.

Applying Grönwall's lemma yields:

$$\sup_{s \in [0, t]} \mathbb{E}[|X_N(s) - X_N^M(s)|^p] \leq C_{\mathcal{K}}^p \left(\frac{2}{M^{p-1}} + \left(\frac{4^p}{M} \right)^{1/2} \right) e^{C_{\mathcal{K}}^p t}.$$

which ends the proof. ■

C.4 Proof of Proposition 1

Applying Minkowski's inequality:

$$\left(\sup_{s \in [0, t]} \mathbb{E}|X_s - X_N^M(s)|^p \right)^{1/p} \leq \left(\sup_{s \in [0, t]} \mathbb{E}|X_s - X_N(s)|^p \right)^{1/p} + \left(\sup_{s \in [0, t]} \mathbb{E}|X_N(s) - X_N^M(s)|^p \right)^{1/p}.$$

Using Jensen's inequality,

$$\sup_{s \in [0, t]} \mathbb{E}|X_s - X_N^M(s)|^p \leq 2^{p-1} \left(\sup_{s \in [0, t]} \mathbb{E}|X_s - X_N(s)|^p + \sup_{s \in [0, t]} \mathbb{E}|X_N(s) - X_N^M(s)|^p \right).$$

The error bound of Theorem 2 as well as Theorem 2.2 (ii) in [Richard et al. \(2021\)](#) claim the existence of positive constants K_p^1 and K_p^2 such that

$$\sup_{s \in [0, t]} \mathbb{E} |X_s - X_N^M(s)|^p \leq \begin{cases} K_p^1 \left((1 + \mathbb{E}[|X_0|^p]) \delta_N^{p(\alpha \wedge 1) - \varepsilon} + \frac{e^{C_K^p t}}{M^{p-1}} \right), & \text{if } 1 \leq p < 2, \\ K_p^2 \left((1 + \mathbb{E}[|X_0|^p]) \delta_N^{p(\alpha \wedge 1) - \varepsilon} + \left(\frac{2}{M^{p-1}} + \left(\frac{4^p}{M} \right)^{\frac{1}{2}} \right) e^{C_K^p t} \right), & \text{if } p \geq 2. \end{cases}$$

which ends the proof. ■

D Error of the RFF scheme: the S-fBM kernel

D.1 Proof of Theorem 5

By stationarity one has from Lemma 2 that:

$$\forall (i, j) \in \mathbb{N}, \quad |\text{Cov}(h(Y_i), h(Y_j))| \leq (b-a)^2 C \rho^{|i-j|}.$$

Let $Y_i = h(Y_i) - \mathbb{E}[h(Y_i)]$ so that $S_M = \sum_{i=1}^M Y_i$. Each Y_i satisfies $|Y_i| \leq b-a$ and by assumption

$$|\text{Cov}(h(Y_i), h(Y_j))| \leq (b-a)^2 C \rho^{|i-j|}, \quad 0 < \rho < 1.$$

We first bound the variance of S_M :

$$\text{Var}(S_M) = \sum_{i=1}^M \text{Var}(Y_i) + 2 \sum_{1 \leq i < j \leq M} \text{Cov}(Y_i, Y_j).$$

By the covariance bound,

$$\text{Var}(S_M) \leq M \sup_i \text{Var}(Y_i) + 2(b-a)^2 C \sum_{i=1}^M \sum_{k=1}^{M-i} \rho^k = M \sup_i \text{Var}(Y_i) + 2(b-a)^2 C \sum_{k=1}^{M-1} (M-k) \rho^k.$$

Since

$$\sum_{k=1}^{M-1} (M-k) \rho^k \leq M \sum_{k=1}^{\infty} \rho^k = M \frac{\rho}{1-\rho},$$

we obtain

$$\text{Var}(S_M) \leq M \left(\sup_{1 \leq i \leq M} \text{Var}(Y_i) + 2(b-a)^2 C \frac{\rho}{1-\rho} \right).$$

By Popoviciu's inequality on variances,

$$\text{Var}(S_M) \leq M \left(\frac{(b-a)^2}{4} + 2(b-a)^2 C \frac{\rho}{1-\rho} \right).$$

We define

$$v := \frac{(b-a)^2}{4} \left(1 + \frac{8\rho}{1-\rho} \right),$$

in order to introduce compactly the positive constant C such that $\text{Var}(S_M) \leq MCv$. Next, recall a standard Bernstein-type moment generating function inequality for S_M ; there exists a constant $C_1 > 0$ such that

$$\log \mathbb{E} e^{u S_M} \leq C_1 u^2 \text{Var}(S_M).$$

Thus, we obtain

$$\log \mathbb{E} e^{uS_M} \leq C_1 u^2 M v.$$

Consider now the normalized sum

$$T_M := \frac{1}{M} \sum_{i=1}^M (h(Y_i) - \mathbb{E}[h(Y_i)]) = \frac{S_M}{M}.$$

One straightforwardly has:

$$\text{Var}(T_M) = \frac{1}{M^2} \text{Var}(S_M) \leq \frac{v}{M}.$$

Applying the same Bernstein-type moment generating function inequality to T_M leads to:

$$\log \mathbb{E} e^{uT_M} \leq C_1 u^2 \text{Var}(T_M) \leq C_1 u^2 \frac{v}{M}.$$

Hence,

$$\log \left[\mathbb{E} \left(\exp \left(\frac{u}{M} \sum_{i=1}^M (h(Y_i) - \mathbb{E}[h(\eta)]) \right) \right) \right] \leq C_1 u^2 \frac{v}{M}.$$

Similarly, there exists a positive constant $C_2 > 0$ such that:

$$\log \left[\mathbb{E} \left(\exp \left(\frac{u}{M} \sum_{i=1}^M (h(\hat{X}_i) - \mathbb{E}[h(\hat{X}_0)]) \right) \right) \right] \leq C_2 u^2 \frac{v}{M}.$$

By the propagation of errors, one can write:

$$\log \left[\mathbb{E} \left(\exp \left(u \frac{1}{M} \sum_{i=1}^M (h(\hat{X}_i) - \mathbb{E}[h(\eta)]) \right) \right) \right] \leq C_1 u^2 \frac{v}{M} + C_2 u^2 \frac{v}{M} + \left| \mathbb{E}[h(\hat{X}_0)] - \mathbb{E}[h(\eta)] \right|.$$

As h is bounded, by fixing an arbitrary positive real R one can write using the triangle inequality:

$$\left| \mathbb{E}[h(\hat{X}_0)] - \mathbb{E}[h(\eta)] \right| \leq C \left(\int_{B(0,R)} |f_\omega(\mathbf{x}) - \hat{f}_\omega^N(\mathbf{x})| d\mathbf{x} + \|f_\omega - \hat{f}_\omega^N\|_1^r \right).$$

Thanks to Theorem 5 as well as Proposition 3, there exists a positive constant C_3 such that:

$$\left| \mathbb{E}[h(\hat{X}_0)] - \mathbb{E}[h(\eta)] \right| \leq C_3 \Psi_N^R(T, \nu, d, H, C_\Psi),$$

where

$$\begin{aligned} \Psi_N^R(T, \nu, d, H, C_\Psi) := & \left[\left(\frac{T^2}{2} \right)^{\frac{d}{2}} \frac{\nu^2}{\Gamma(\frac{d}{2})} \left(\frac{1}{d} \left(\frac{eT^2 R^2}{4N} \right)^N \frac{1}{e(\frac{d}{2} + 1)_N} \right. \right. \\ & \left. \left. + \frac{1}{d + 2H} \frac{C_\Psi}{e(2C_\Psi R e(N-1) - 1)(N-1)^{2C_\Psi R e(N-1) - 1}} \right) \right. \\ & \left. + \frac{\Omega_d C_\omega (TR + \kappa(d))^d - TR^d}{T^d d \kappa(d)} e^{-TR} \right]. \end{aligned}$$

This is true for any $R > 0$ in particular $R = \sqrt{N}$, which means that:

$$\left| \mathbb{E}[h(\hat{X}_0)] - \mathbb{E}[h(\eta)] \right| \leq C_3 \Psi_N(T, \nu, d, H, C_\Psi),$$

where $\Psi_N(T, \nu, d, H, C_\Psi) = \Psi_N^{\sqrt{N}}(T, \nu, d, H, C_\Psi)$. Putting the terms together, one has:

$$\log \left[\mathbb{E} \left(\exp \left(\frac{u}{M} \sum_{i=1}^M (h(\hat{X}_i) - \mathbb{E}[h(\eta)]) \right) \right) \right] \leq C \left(\frac{2vu^2}{M} + \Psi_N^R(T, \nu, d, H, C_\Psi) \right),$$

where $C = C_1 \vee C_2 \vee C_3 \vee C_4$. Using Markov's inequality, for any $t \geq 0$:

$$\mathbb{P}(|\hat{\mu}_M - \mu| \geq t) \leq \exp \left(-ut + C \left(\frac{vu^2}{M} + \Psi_N^R(T, \nu, d, H, C_\Psi) \right) \right),$$

Similarly to Hoeffding's inequality (by minimizing the exponent), this holds in particular for:

$$u^* = \frac{Mt}{4Cv}.$$

which leads to:

$$\mathbb{P}(|\hat{\mu}_M - \mu| \geq t) \leq \exp \left(-\frac{Mt^2}{8Cv} + C\Psi_N(T, \nu, d, H, C_\Psi) \right).$$

■

D.2 Proof of Corollary 1

For the sake of compactness, define:

$$\alpha := \frac{1}{8Cv}, \quad \beta := C\Psi_N(T, \nu, d, H, C_\Psi),$$

so that the tail bound is

$$\mathbb{P}(|\hat{\mu}_M - \mu| \geq t) \leq e^\beta e^{-\alpha Mt^2}, \quad t \geq 0.$$

For any real $p > 0$ we use the identity

$$\mathbb{E}[|\hat{\mu}_M - \mu|^p] = \int_0^\infty p t^{p-1} \mathbb{P}(|\hat{\mu}_M - \mu| \geq t) dt,$$

Hence

$$\begin{aligned} \mathbb{E}[|\hat{\mu}_M - \mu|^p] &= \int_0^\infty p t^{p-1} \mathbb{P}(|\hat{\mu}_M - \mu| \geq t) dt \\ &\leq e^\beta p \int_0^\infty t^{p-1} e^{-\alpha Mt^2} dt. \end{aligned}$$

The remaining integral is standard: for $b > 0$,

$$\int_0^\infty t^{p-1} e^{-bt^2} dt = \frac{1}{2} b^{-p/2} \Gamma\left(\frac{p}{2}\right).$$

We obtain

$$\mathbb{E}[|\hat{\mu}_M - \mu|^p] \leq e^\beta p \cdot \frac{1}{2} (\alpha M)^{-p/2} \Gamma\left(\frac{p}{2}\right).$$

Using the identity $\Gamma(1+s) = s\Gamma(s)$, this can be written compactly as

$$\mathbb{E}[|\hat{\mu}_M - \mu|^p] \leq e^\beta \Gamma\left(1 + \frac{p}{2}\right) (\alpha M)^{-p/2},$$

meaning that:

$$\mathbb{E}[|\hat{\mu}_M - \mu|^p] \leq e^{C\Psi_N(T, \nu, d, H, C_\Psi)} \Gamma\left(1 + \frac{p}{2}\right) \left(\frac{1}{8Cv} M\right)^{-p/2}.$$

which leads to the claimed result.

■

D.3 Proof of Theorem 6

We use the same notations as in the proof of Theorem 2 (Appendix C.3). We recall that:

$$X_N(t) - X_N^M(t) = I_t^{(1)} + I_t^{(2)}.$$

where:

$$\begin{cases} I_t^{(1)} = \int_0^t K(t - \zeta_N(s)) \left(\sigma(\zeta_N(s), X_N(\zeta_N(s))) - \sigma(\zeta_N(s), X_N^M(\zeta_N(s))) \right) dW_s \\ I_t^{(2)} = \int_0^t \left(K(t - \zeta_N(s)) - \widehat{K}_M(t - \zeta_N(s)) \right) \sigma(\zeta_N(s), X_N^M(\zeta_N(s))) dW_s \end{cases} \quad (91)$$

Following the same arguments as in Appendix C.3, one has the bound:

$$\begin{cases} \mathbb{E}[|I_t^{(1)}|^p] \leq C_t \int_0^t \sup_{0 \leq u \leq s} \mathbb{E}[|X_N(u) - X_N^M(u)|^p] ds \\ \mathbb{E}[|I_t^{(2)}|^p] \leq C(\mathcal{K}) \left(\mathbb{E}[|X_0^M|^p] + |K(0)|^p \right) \int_0^t \mathbb{E} \left(|K(t - \zeta_N(s)) - \widehat{K}_M(t - \zeta_N(s))|^p \right) ds \end{cases}$$

Using the result of Corollary 1, one has:

$$\mathbb{E} \left(|K(t - \zeta_N(s)) - \widehat{K}_M(t - \zeta_N(s))|^p \right) \leq e^{C_2 \Psi_N(T, \nu, d, H, C_\Psi)} \Gamma \left(1 + \frac{p}{2} \right) \left(\frac{1}{8C_2\nu} M \right)^{-p/2}.$$

As a result,

$$\sup_{s \in [0, t]} \mathbb{E}[|X_N(s) - X_N^M(s)|^p] \leq C_{\mathcal{K}}^p \left(\int_0^t \sup_{0 \leq u \leq s} \mathbb{E}[|X_N(u) - X_N^M(u)|^p] ds + e^{C_2 \Psi_N(T, \nu, d, H, C_\Psi)} \Gamma \left(1 + \frac{p}{2} \right) \left(\frac{1}{8C_2\nu} M \right)^{-p/2} \right).$$

where $C_{\mathcal{K}}^p = C(\mathcal{K}) \left(\mathbb{E}[|X_0^M|^p] + |K(0)|^p \right) \vee C_t$. Hence, we obtain thanks to Grönwall's lemma:

$$\sup_{s \in [0, t]} \mathbb{E}[|X_N(s) - X_N^M(s)|^p] \leq C_{\mathcal{K}}^p e^{C_2 \Psi_N(T, \nu, d, H, C_\Psi) + C_{\mathcal{K}}^p t} \Gamma \left(1 + \frac{p}{2} \right) \left(\frac{1}{8C_2\nu} M \right)^{-p/2}.$$

Applying Minkowski's inequality:

$$\left(\sup_{s \in [0, t]} \mathbb{E}[|X_s - X_N^M(s)|^p] \right)^{1/p} \leq \left(\sup_{s \in [0, t]} \mathbb{E}[|X_s - X_N(s)|^p] \right)^{1/p} + \left(\sup_{s \in [0, t]} \mathbb{E}[|X_N(s) - X_N^M(s)|^p] \right)^{1/p}.$$

Using Jensen's inequality,

$$\sup_{s \in [0, t]} \mathbb{E}[|X_s - X_N^M(s)|^p] \leq 2^{p-1} \left(\sup_{s \in [0, t]} \mathbb{E}[|X_s - X_N(s)|^p] + \sup_{s \in [0, t]} \mathbb{E}[|X_N(s) - X_N^M(s)|^p] \right).$$

Using the error bound of the classical Euler scheme of Theorem 2.2 (ii) in [Richard et al. \(2021\)](#), there exist positive constants K_p^1 and C_p^1 such that

$$\sup_{s \in [0, t]} \mathbb{E}[|X_s - X_N^M(s)|^p] \leq K_p^1 \left(\left(1 + \mathbb{E}[|X_0|^p] \right) \delta_N^{p(\alpha \wedge 1) - \varepsilon} + e^{C_p^1(\Psi_N(T, \nu, d, H, C_\Psi) + t)} \Gamma \left(1 + \frac{p}{2} \right) \left(\frac{1}{8C_2\nu} M \right)^{-p/2} \right)$$

without loss of generality, we denote C_p^1 as C_p which ends the proof. ■

E Numerical appendix

E.1 S-fBM spectral density representation

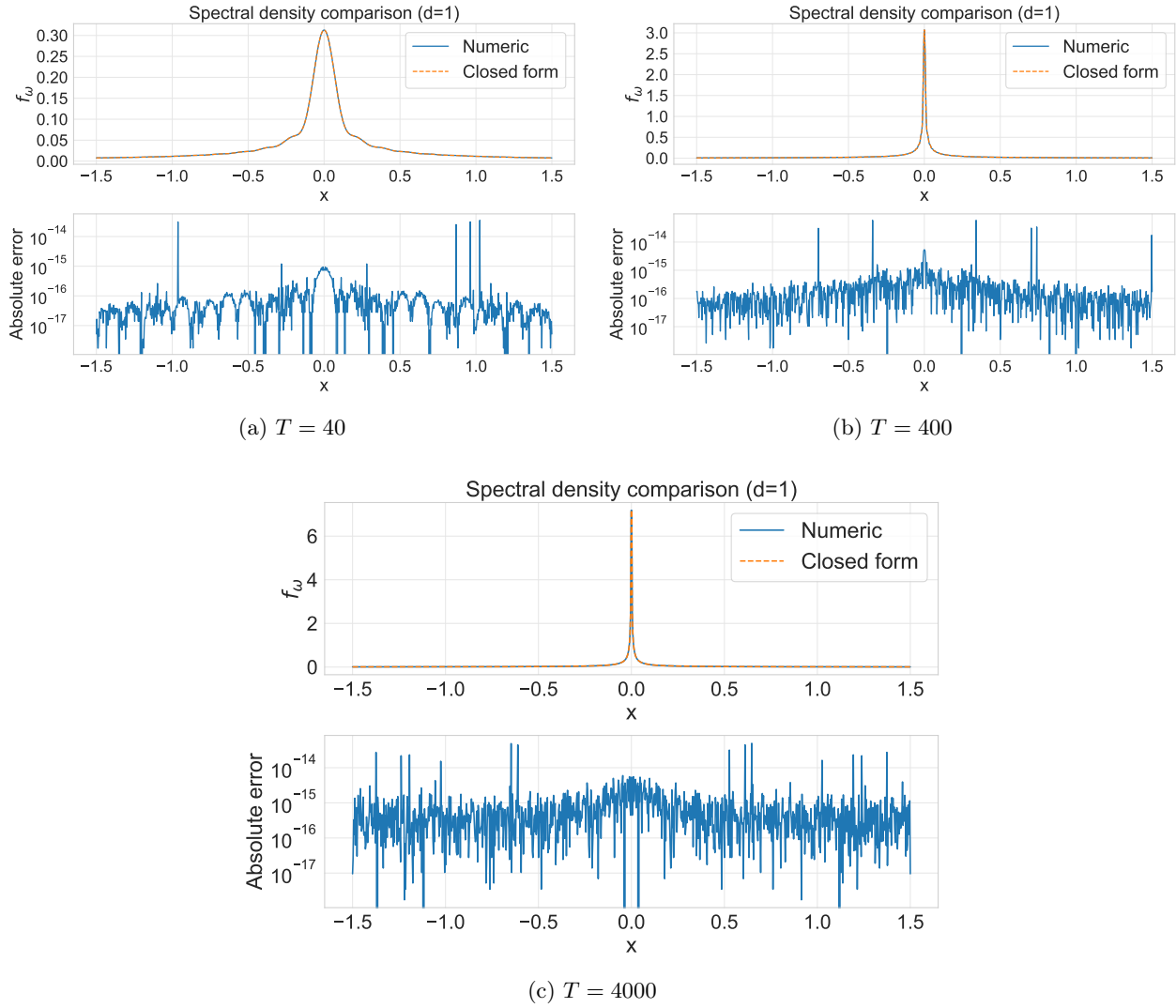
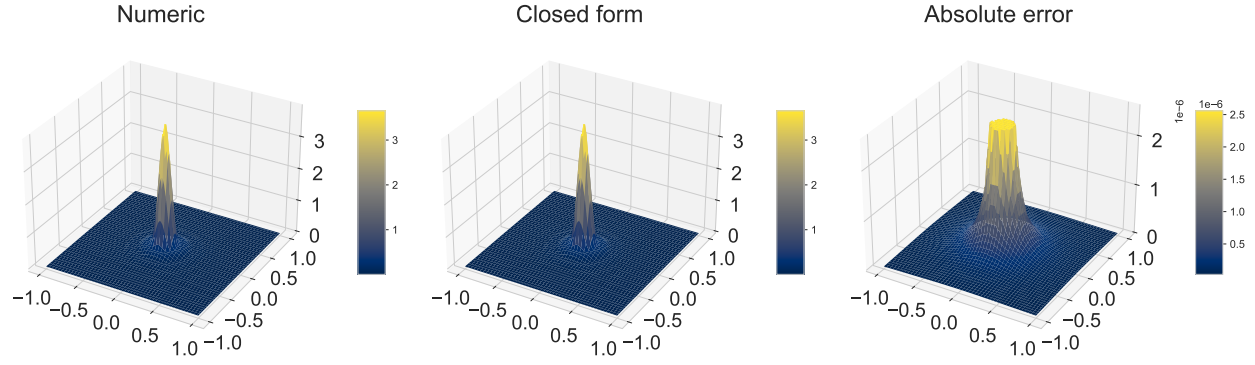
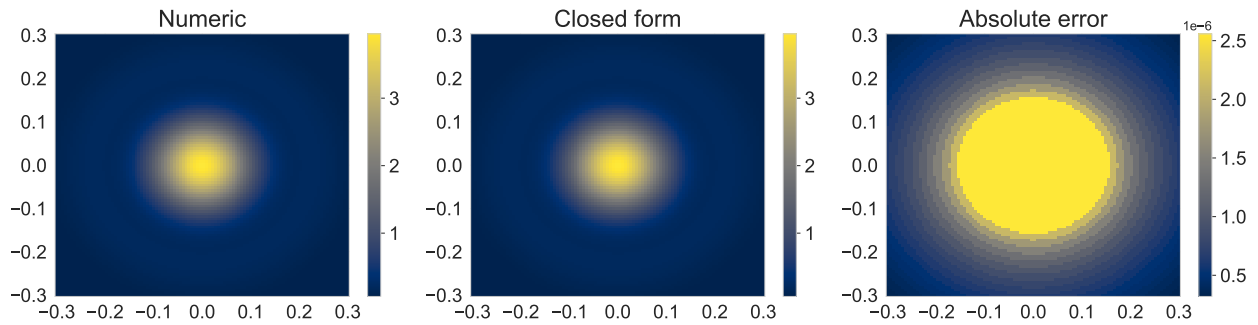


Figure 8: Illustration of the estimated quantities for increasing correlation limits T with fixed parameters $H = 0.01$ and $\nu^2 = 1$. The top panels correspond to $T = 40$ and $T = 400$, while the bottom panel shows the results for $T = 4000$.



(a) Pointwise error surface



(b) Colormap of the absolute error

Figure 9: Two dimensional validation of the spectral density representation for $H = 0.01$ and $\nu^2 = 2$. The top panel shows the surface of the pointwise difference between the analytical spectral density and its numerical Fourier integration reference for $T = 40$. The bottom panels display the corresponding colormap representations, highlighting that the approximation error remains at the level of machine precision across the frequency domain.

E.2 Proof of Theorem 7

Consider the GMM objective functions associated with the true and approximated discrepancies:

$$\forall x \in \Xi, \quad \begin{cases} \mathcal{T}(x) := \mathbf{h}(x)^T W \mathbf{h}(x), \\ \hat{\mathcal{T}}(x) := \hat{\mathbf{h}}(x)^T W \hat{\mathbf{h}}(x), \end{cases}$$

where ∇ and ∇^2 denote the gradient and Hessian operators, respectively. By definition of the GMM estimator, $\hat{\theta}_M$ satisfies the first-order condition:

$$\nabla \hat{\mathcal{T}}(\hat{\theta}_M) = 0.$$

Using a first-order Taylor expansion, there exists $\tilde{\theta} \in \Xi$ such that:

$$\nabla \hat{\mathcal{T}}(\hat{\theta}_M) = \nabla \hat{\mathcal{T}}(\theta^*) + \nabla^2 \hat{\mathcal{T}}(\tilde{\theta})(\hat{\theta}_M - \theta^*).$$

Hence,

$$\hat{\theta}_M - \theta^* = -\left(\nabla^2 \hat{\mathcal{T}}(\tilde{\theta})\right)^{-1} \nabla \hat{\mathcal{T}}(\theta^*).$$

Since $\hat{\mathcal{T}}(\cdot)$ is differentiable, we have for any $x \in \Xi$:

$$\begin{cases} \nabla \hat{\mathcal{T}}(\mathbf{x}) = 2\hat{J}(\mathbf{x})^\top W \hat{\mathbf{h}}(\mathbf{x}), \\ \nabla^2 \hat{\mathcal{T}}(\mathbf{x}) = 2\hat{J}(\mathbf{x})^\top W \hat{J}(\mathbf{x}) + 2 \left(\nabla^2 \hat{\mathbf{h}}(\mathbf{x}) \right) W \hat{\mathbf{h}}(\mathbf{x}), \end{cases}$$

where \hat{J} denotes the Jacobian of $\hat{\mathbf{h}}$ and the contraction $\left(\nabla^2 \hat{\mathbf{h}}(\mathbf{x}) \right) W \hat{\mathbf{h}}(\mathbf{x})$ is defined componentwise as:

$$\left(\nabla^2 \hat{\mathbf{h}}(\mathbf{x}) \right) W \hat{\mathbf{h}}(\mathbf{x}) = \sum_{k=1}^Q \left(W \hat{\mathbf{h}}(\mathbf{x}) \right)_k \nabla^2 \left(\hat{\mathbf{h}} \right)_k(\mathbf{x}),$$

where $\left(\hat{\mathbf{h}} \right)_k$ is the k^{th} component of $\hat{\mathbf{h}}$. One has straightforwardly that:

$$\left\| \hat{\theta}_M - \theta^* \right\|_2^2 \leq \frac{\left\| \nabla \hat{\mathcal{T}}(\theta^*) \right\|_2^2}{\left\| \nabla^2 \hat{\mathcal{T}}(\hat{\theta}) \right\|_2^2}.$$

Let us lower bound the denominator. Applying the inverse triangle inequality gives:

$$\left\| \nabla^2 \hat{\mathcal{T}}(\mathbf{x}) \right\| \geq 2 \left(\left\| \hat{J}(\mathbf{x})^\top W \hat{J}(\mathbf{x}) \right\| - \left\| \left(\nabla^2 \hat{\mathbf{h}}(\mathbf{x}) \right) W \hat{\mathbf{h}}(\mathbf{x}) \right\| \right).$$

As W is symmetric positive definite, one has:

$$\left\| \hat{J}(\mathbf{x})^\top W \hat{J}(\mathbf{x}) \right\| \geq \sigma_{\min}(\hat{J}(\mathbf{x})^\top W \hat{J}(\mathbf{x})) = \sigma_{\min}(W) \sigma_{\min}(\hat{J}(\mathbf{x}))^2.$$

On the other hand:

$$\left\| \left(\nabla^2 \hat{\mathbf{h}}(\mathbf{x}) \right) W \hat{\mathbf{h}}(\mathbf{x}) \right\| \leq \|W\|_\infty \left\| \hat{\mathbf{h}}(\mathbf{x}) \right\|_\infty \sum_{k=1}^Q \left\| \nabla^2 \left(\hat{\mathbf{h}} \right)_k(\mathbf{x}) \right\|.$$

This can be rewritten as:

$$\left\| \left(\nabla^2 \hat{\mathbf{h}}(\mathbf{x}) \right) W \hat{\mathbf{h}}(\mathbf{x}) \right\| \leq \|W\|_\infty \left\| \hat{\mathbf{h}}(\mathbf{x}) \right\|_\infty \hat{H}_Q(\mathbf{x}),$$

where $\hat{H}_Q(\mathbf{x}) = \sum_{k=1}^Q \left\| \nabla^2 \left(\hat{\mathbf{h}} \right)_k(\mathbf{x}) \right\|$. This leads to the following lower bound for any $\mathbf{x} \in \Xi$:

$$\left\| \nabla^2 \hat{\mathcal{T}}(\mathbf{x}) \right\| \geq 2 \left[\sigma_{\min}(W) \sigma_{\min}(\hat{J}(\mathbf{x}))^2 - \|W\|_\infty \left\| \hat{\mathbf{h}}(\mathbf{x}) \right\|_\infty \hat{H}_Q(\mathbf{x}) \right]_+.$$

where $\sigma_{\min}(\cdot)$ is the smallest singular value and $[\cdot]_+$ is the positive part.

On the other hand, after some algebra one has:

$$\left\| \nabla \hat{\mathcal{T}}(\mathbf{x}) \right\|_2 \leq 2 \left\| \hat{J}(\mathbf{x}) \right\| \left\| W \right\| \left\| \hat{\mathbf{h}}(\mathbf{x}) \right\|_2$$

This leads to:

$$\left\| \hat{\theta}_M - \theta^* \right\|_2 \leq \frac{\left\| \hat{J}(\theta^*) \right\| \left\| W \right\| \left\| \hat{\mathbf{h}}(\theta^*) \right\|_2}{\left[\sigma_{\min}(W) \sigma_{\min}(\hat{J}(\hat{\theta}))^2 - \|W\|_\infty \left\| \hat{\mathbf{h}}(\hat{\theta}) \right\|_\infty \hat{H}_Q(\hat{\theta}) \right]_+}.$$

By direct computations:

$$\mathbb{E} \left[\left\| \hat{\mathbf{h}}(\theta^*) \right\|_2^2 \right] = \frac{1}{M} \sum_{k=1}^Q \text{Var}(\cos(\eta\tau_k)) \leq \frac{Q}{M}.$$

As a result, there exists an explicit positive constant:

$$K_W := \frac{\|\hat{J}(\theta^*)\|}{\left[\sigma_{\min}(W) \sigma_{\min}(\hat{J}(\tilde{\theta}))^2 - \|W\|_{\infty} \|\hat{\mathbf{h}}(\tilde{\theta})\|_{\infty} \hat{H}_Q(\tilde{\theta}) \right]_+}$$

such that:

$$\|\hat{\theta}_M - \theta^*\|_{\mathcal{L}^2} \leq K_W \|W\| \sqrt{\frac{Q}{M}}.$$

■